# A deviational Monte Carlo formulation of ab initio phonon transport and its application to the study of kinetic effects in graphene ribbons



by

Colin D. Landon

B.S., Brigham Young University (2008)
S.M., Massachusetts Institute of Technology (2010)

Submitted to the Department of Mechanical Engineering
in partial fulfillment of the requirements for the degree of

Doctor of Philosophy in Mechanical Engineering

at the

MASSACHUSETTS INSTITUTE OF TECHNOLOGY

June 2014



Signature redacted

Author .....
Department of Mechanical Engineering
March 3, 2014

Signature redacted

Certified by .....
Nicolas G. Hadjiconstantinou
Professor of Mechanical Engineering
Thesis Supervisor

Signature redacted

Accepted by .....
David E. Hardt
Chairman, Department Committee on Graduate Theses

Signature redacted

Accepted by .....
Youssef Marzouk
Co-Director, Computational Science and Engineering

# A deviational Monte Carlo formulation of ab initio phonon transport and its application to the study of kinetic effects in graphene ribbons

by

Colin D. Landon

Submitted to the Department of Mechanical Engineering
on March 3, 2014, in partial fulfillment of the
requirements for the degree of
Doctor of Philosophy in Mechanical Engineering

## Abstract

We present a deviational Monte Carlo method for solving the Boltzmann equation for phonon transport subject to the linearized ab initio 3-phonon scattering operator. Phonon dispersion relations and transition rates are obtained from density functional theory calculations. The ab initio scattering operator replaces the commonly used relaxation-time approximation, which is known to neglect, among other things, coupling between out of equilibrium states. The latter is particularly important in two-dimensional materials such as graphene, which is the subject of this thesis.

One important ingredient of the method presented here is an energy-conserving, stochastic particle algorithm for simulating the linearized form of the ab initio scattering operator. This scheme is incorporated within the recently developed deviational, energy-based formulation of the Boltzmann equation, to obtain, for the first time, low-variance Monte Carlo solutions of this model for time- and spatially-dependent problems. The deviational formulation ensures that simulations are computationally feasible for arbitrarily small temperature differences, while the stochastic treatment of the scattering operator is both efficient—in the limit of large number of states, it outperforms the more traditional direct evaluation methods used in solutions of the homogeneous Boltzmann equation—and exhibits no timestep error.

We use the method to study heat transport in graphene ribbons, a geometry used to experimentally measure the thermal conductivity of graphene. Our results show that the effective thermal conductivity of ribbons decreases monotonically as either the length or the width of the ribbon decreases. We also show that at room temperature the error introduced by modeling the effect of transverse diffuse boundaries using a homogeneous scattering approximation is on the order of 10% and as high as 30%. A simple parametric model for the effective thermal conductivity depending only on the Knudsen number is presented that outperforms the homogenous scattering rate approximation in terms of accuracy. Spatially resolved temperature and heat flux profiles are also obtained and analyzed for the first time in graphene ribbons using

the linearized ab initio scattering term.

Thesis Supervisor: Nicolas G. Hadjiconstantinou
Title: Professor of Mechanical Engineering

# Acknowledgments

Looking back at the course that this research has taken, I am very grateful for the assistance that I have received and pleased with the final product. This thesis is not what I envisioned when I started three and a half years ago. For one thing, its scope is narrower, but the final treatment of phonon transport is significantly more valuable, largely due to the well timed emergence of ab initio thermal transport simulations in two dimensional materials. I was initially disappointed that the higher fidelity ab initio approach made my work using the relaxation time approximation obsolete, but the ensuing period of studying and research has made this thesis significantly better and in addition has shaped and solidified my career plans. In recently rereading a manuscript that we submitted in early 2012, I was thankful that it had been rejected. These last two years have made an enormous difference.

That time has been so valuable in large part due to my advisor. He has given me complete latitude to explore phonon transport as I desired. My quest for understanding and reproducing faithfully the relevant physics has led me outside what was his area of expertise, but he has learned the material along side me and probably more quickly than I did. I always look forward to our meetings, because he so frequently has laser sharp insights into problems inside and outside his areas of experience. He has also been a wonderful ballast, encouraging consistent work through the long periods of frustration, and restraint with regards to my hair-brained ideas that were very exciting, but more often then not amounted to nothing. He has also been more understanding of and accommodating for the needs of my family than I could possibly have expected. I consider it a true blessing that he has been my advisor during my time at MIT.

Thanks mainly to my wife, she and my three young children thrived in an apartment that was too small, and with father that was too often unavailable. In the afternoons, I often had little and quite persistent reminders that it was 5:00 knocking on my door. I will always be thankful to my wife and my children who worked with me to build our family while I worked on this research. Their energy, love, and

support have been a constant comfort and strength for me.

While the principal contribution of this work is the spatially and time dependent solution of the Boltzmann equation, this cannot occur without some material model. By providing a relevant model, Sangyeop Lee and Keivan Esfarjani made this project possible. Over the last two years Sangyeop has also been an on going source of insight into thermal transport in graphene and I am deeply grateful to him for his collaboration.

Jean-Phillipe Péraud is a brilliant student and very pleasant friend. He has been quietly and steadily improving the efficiency of stochastic particle methods for phonon transport and many of his contributions to the field are found in the particle method I present herein.

Finally, to the crew of the old room 3-355A—Husain, Gregg, and Ghassan—although renovations took away our place, the memories live on. No one could have asked for a better group to introduce me to MIT and efficient simulations of the Boltzmann equation. Beyond all that, thank you for your continuing friendship.

We also gratefully acknowledge funding for this project provided by the National Defense Science and Engineering Graduate fellowship, the National Science Foundation Graduate Research Fellowship Program, and the MIT-Singapore Alliance.

# Chapter 1

# Introduction

The large thermal conductivity of graphene [41, 10, 29, 69, 34] makes it an appealing material for thermal management applications, but begin a two-dimensional material, thermal transport can be strongly dependent upon boundaries and boundary conditions [98]. This sensitivity can be leveraged to good advantage (e.g. improving the thermo electric figure of merit [110], or creating thermal rectifiers [53, 117, 105]), but can also be detrimental to device performance (e.g. the dramatic reduction of thermal conductivity in supported vs. suspended graphene [109]). This work will focus on the reduction of thermal conductivity in suspended graphene due to small device length scales—the most important contribution being an efficient computational method for simulating thermal transport for arbitrary geometries including fundamental kinetic effects in small-scale graphene devices.

In non-metals like graphene, lattice vibrations are the primary carriers of thermal energy. Due to the theoretical and computational complexity associated with explicit modeling of atomic vibrations to describe thermal transport, atomistic methods tend to be limited in scope to investigations of physics (e.g. [81, 14, 13]), rather than modeling of devices—although some progress has been made in this direction [53, 54, 70]. An alternative to atomistic modeling is provided by the phonon Boltzmann transport equation (BTE) which models thermal transport as a balance between advection and

scattering acting upon the phonon distribution function $n(\boldsymbol{x}, \boldsymbol{q}, s, t)$ [89],

$$\frac{\partial n(\boldsymbol{x}, \boldsymbol{q}s, t)}{\partial t} + \boldsymbol{v}(\boldsymbol{q}s) \cdot \nabla_{\boldsymbol{x}} n(\boldsymbol{x}, \boldsymbol{q}s, t) = \left[\frac{\partial n(\boldsymbol{x}, \boldsymbol{q}s, t)}{\partial t}\right]_{\text{scatt}}, \tag{1.1}$$

where, in our notation, $\boldsymbol{x}$ is the spatial position vector, $\boldsymbol{q}$ the phonon wavevector, $s$ the polarization, and $t$ the time. The details of this equation and in particular the RHS scattering term will be described in Chapters 2 and 3. In the present context, we merely note that the phonon BTE leverages atomistic details (i.e. the dispersion relation and the scattering model) to describe thermal transport without explicit treatment of the atoms or their motion.

## 1.1 Approximations of the phonon BTE

Despite the significant simplification introduced by the phonon BTE compared to direct molecular simulation of the system of interest, the complexity of its scattering operator [124, 115], and the high dimensionality of the phase space $(\boldsymbol{x}, \boldsymbol{q}, s, t)$ has led to the prominent use of various approximations and additional simplifications.

### 1.1.1 Single mode relaxation time approximation

The three phonon scattering operator that will be detailed in Chapter 3 is not amenable to analytical solutions. A simple alternative scattering model is the single mode relaxation time (SMRT) approximation which, rather heuristically, models the scattering of phonons as a simple exponential decay towards a local equilibrium [22, 124]. Within the SMRT approximation and using simplified models for dispersions relations, the phonon BTE has been integrated deterministically both analytically and numerically (e.g. [56, 58, 50]), but these studies are limited to spatially homogeneous problems or very simple geometries [124, 27].

It was not until 1995 that a satisfactory solution method including explicit treatment of momentum and energy conservation for three phonon scattering was developed [87], which we will refer to as the linearized iterative method [77]. This ground

breaking development finally led to solutions of the BTE by employing three important simplifications: spatially homogenous, steady state, and small temperature gradient problems.

Nanoscale thermal transport has most commonly been treated using the SMRT model for the scattering operator (for example [22, 56, 124, 50, 57, 6, 19, 78]) and has been remarkably successful in predicting thermal conductivity in three dimensional semiconductors [6], given the crudeness of the approximation. However, in the context of thermal transport in two-dimensional materials, even before the first isolation of graphene in 2004 [86], it was recognized that the simplistic SMRT model predicted divergent thermal conductivity for materials like graphene [58]. This failure of the SMRT model was troubling, and led to the development of various approximate methods for predicting a finite thermal conductivity which arrived at reasonable values of thermal conductivity for graphene [84, 83, 85, 1, 9],

With the advent of the linearized iterative method, it became apparent that the divergent thermal conductivity was an artifact of the approximate treatment of momentum and energy conservation used in the SMRT [71, 109], that the agreement of the thermal conductivities predicted by the SMRT with experiments was a fortuitous cancelation of errors [112], and that the details of transport (specifically which phonon modes carry the thermal energy) were wrong under this model [71, 109, 113]. These issues highlight the need for the ab initio approaches for modeling phonon dynamics in graphene and justify the added complexity associated with such methods [77].

## 1.2 Numerical solution of the Boltzmann equation–Background

Spatial and time dependent solutions of the Boltzmann equation are essential to the field of nanoscale heat transfer. This is particularly true due to the complex interplay between ballistic effects and geometry (e.g. [98, 105]). We also note that recent experiments have included time-dependencies (e.g. [20, 18, 108, 107]). On the other

hand, closed form solutions of (1.1) are only available for the simplest of problems and following drastic simplifications–most notably the equilibrium solution, which is the Bose-Einstein distribution, and which is independent of the spatial and time variables,

$$n^{\text{eq}}(\omega(\boldsymbol{qs});T) = \frac{1}{\exp\left(\frac{\hbar\omega(\boldsymbol{qs})}{k_b T}\right) - 1}. \tag{1.2}$$

A few other simple geometries admit closed form solutions when the SMRT approximation is employed (See Section 6.7.2 and Ref. [27]). Under some conditions, spatial effects can be introduced approximately as will also be discussed and analyzed in Chapter 7.

Apart from these exceptions, integration of spatially and temporally dependent problems remains challenging due to the high dimensionality of (1.1) and the traveling discontinuities in the distribution function expected from the LHS of (1.1) [5]. Due to these factors, deterministic integration is computationally demanding both in terms of CPU time and memory storage and requires complex algorithms.

Alternatively, integration can be performed with stochastic particle or Monte Carlo (MC) methods, which ameliorate most of the limitations of the deterministic solvers. Specifically, particle methods can accurately and stably propagate the discontinuities in the distribution function [52], and, given a simple scattering model, MC methods do not even require discretization of the wavevector space. These advantages also come with an intuitive formulation and natural importance sampling which improves computational efficiency [51]. On the other hand, MC methods suffer from statistical noise which can be removed by sampling, but only at a rate of $M^{-1/2}$, where $M$ is the number of independent samples [45, 93]. The balance between stochastic noise and computational efficiency allows stochastic methods to be generally more efficient when an error of greater than 1% is acceptable, but below that level deterministic methods tend to have the advantage [93]. Notable among the stochastic methods are the low variance deviational simulation Monte Carlo (LVDSMC) methods, which dramatically reduce the stochastic noise by simulating only the deviation from equilibrium [7, 52, 103].

Monte Carlo simulation of phonon transport [60, 96, 93] has emerged rather recently compared to Monte Carlo simulation of rarefied gases known as Direct simulation Monte Carlo (DSMC) [11, 12]. Mainly for this reason, DSMC has been studied much more thoroughly in terms of the numerical aspects, including convergence [104, 120], discretization errors [3, 4, 43, 38, 101], and variance reducing formulations [7, 52, 103]. The DSMC simulations differ from phonon transport primarily in the form of the scattering model, but many of the important developments for DSMC are only recently being incorporated into phonon Monte Carlo simulations, or remain unaddressed [91, 92, 67, 93].

Phonon Monte Carlo simulations first appeared in 1988, albeit only for a ballistic problem [60]. The first phonon Monte Carlo to include a scattering term—the SMRT approximation—did not appear until 1994 [96]. Since that time a number of important advancements have been introduced including dispersion relation improvements [75, 82], frequency dependent relaxation times [75], scattering step energy conservation [65], strict momentum and energy conservation [30], and more efficient formulations [91, 67, 93]. All of these works were able to avoid discretization of the reciprocal space due to the use of the SMRT scattering model, but as described in Section 1.1.1, this convenient feature comes at the cost of misrepresenting important details of phonon transport in graphene.

### 1.2.1 Moving beyond the relaxation time approximation

While the advection algorithm for MC simulation of (1.1) is the same regardless of the scattering operator, developing an efficient particle based treatment of the scattering operator is challenging and varies greatly with the scattering model. Such a method for the hard sphere scattering operator for gases was at the heart of Bird's seminal DSMC paper [11].

In the context of more phonon-like scattering operators, Garcia and Wagner have developed an extension of DSMC for the Uehling-Uhlenbeck collision operator that obeys Bose-Einstein (as well as Fermi-Dirac) statistics [39]. Their algorithm obtains the scattering rate for a particle by reconstructing the distribution from its samples

and explicitly evaluating the scattering operator. Although this method should be generally applicable to any scattering operator, reconstruction is very inefficient–it requires discretization of reciprocal space and an adequate number of samples in all reciprocal space cells.

Matsumoto *et al.* developed a DSMC-like method for four phonon scattering that does not need discretization of reciprocal space [73, 74]. In their algorithm, pairs of phonons are selected for collision, but, without justification, they chose a constant scattering rate. It is not clear how an appropriate scattering rate would be calculated over the continuous wavevector space. Furthermore, the post collision wavevectors are randomly selected and the collision is discarded if energy conservation cannot be satisfied based on the dispersion relation. This scheme is expected to lead to an overwhelming number of rejected collisions and be problematically inefficient for any real dispersion relation—their work considers only a single branch.

Brown and Hensel proposed a mixed scheme which uses a deterministic finite-volume integrator for the LHS of the phonon BTE and a "statistical" model for the RHS [16, 17]. Although they appear to allow scattering events only between appropriate sets of three phonon states, the rate of distribution function change is chosen, arbitrarily, to be linearly proportional to the deviation from equilibrium. In this manner, their algorithm naturally has the correct equilibrium distribution, but it is not at clear that the dynamics of the scattering are correct in any other manner.

Finally, we mention Hamzeh and Aniel, who employ a linearized ab initio scheme similar to that of Ref. [88] to calculate the transition probability for each pathway and a generalized Ridley scheme to estimate the transition probability (in terms of the Grüneisen parameter). They then use a scheme similar to the approach of Garcia and Wagner wherein they discretize reciprocal space and reconstruct the distribution function to evaluate the scattering rates [48]. We cannot comment on their implementation of the scattering because their report lacks sufficient details, nor on their implementation of the advection because they only preform simulation of a spatially homogenous problem.

## 1.3 Thesis overview

Chapters 2 and 3 of this thesis present the necessary background for the state of the art iterative solutions of the linearized ab initio phonon Boltzmann equation. The iterative solution, numerical aspects associated with it, and results for graphene using dispersion relations from density functional theory (DFT) and scattering rates from density functional perturbation theory (DFPT) calculations are presented in Chapter 4.

Due to the significant computational advantages associated with deviational methods [7, 52, 8], the present thesis focuses on the development of an energy-based deviational Monte Carlo method for simulating phonon transport in graphene using the linearized ab initio three phonon scattering operator. This is made possible by reformulating the discrete version of the linearized collision operator as a linear system of ordinary differential equations (see Chapter 5). The other major ingredient of the proposed method is a stochastic particle scheme for integrating this system of ODEs. This scheme is numerically more efficient than matrix based deterministic methods because it requires roughly $\mathcal{O}(N_{\text{states}} \log(N_{\text{states}}))$ operations in contrast to $\mathcal{O}(N_{\text{states}}^2)$ required by the former, where $N_{\text{states}}$ is the number of states in the discretization of reciprocal space. Moreover, it is strictly energy conserving and introduces no timestep discretization error in the scattering model. It also is directly compatible with the intuitive particle treatment of the advection terms of the Boltzmann equation. The complete scheme, which we will refer to as linearized ab initio phonon low variance deviational simulation Monte Carlo (LAIP-LVDSMC) is described in Chapter 6. The proposed method is used to analyze finite length and finite width kinetic effects in micro and nanoscale graphene ribbons as well as "homogeneous" approximations of the effect of boundaries in graphene ribbons in Chapter 7.

# Chapter 2

# Background

In order to introduce the notation used throughout this work, define the parameters, and lay the theoretical foundations for the methods that follow, it will be convenient to present a brief derivation of lattice dynamics [115] and the linearized iterative solution method [87, 77]. This derivation differs from the standard [115] in its use of an analytical decomposition for the distribution function [7], which will lead naturally to the governing equations for the iterative solution as well as our new solution method.

## 2.1 Direct Lattice

A crystal is a combination of a lattice and a basis. Graphene has a hexagonal lattice and a two carbon atom basis in the honeycomb arrangement. The underlying properties that will be used throughout this work are a mass of $M_{\text{atom}} = 1.992646635752415 \times 10^{-26}$ kg for carbon, the lattice parameter $a_{\text{lat}} = 2.4328709987\mathring{A}$, the nominal thickness $\delta = 3.35\mathring{A}$, the real space lattice vectors

$$\begin{aligned} \boldsymbol{a}_1 &= \left(\frac{\sqrt{3}}{2}, \frac{1}{2}, 0\right) a_{\text{lat}} \\ \boldsymbol{a}_2 &= (0, 1, 0) a_{\text{lat}} \\ \boldsymbol{a}_3 &= (0, 0, 1) \end{aligned} \tag{2.1}$$

and the basis vectors

$$\begin{aligned} \boldsymbol{b}_1 &= (0.0, 0.0, 0.0) \\ \boldsymbol{b}_2 &= (0.7023093630, 1.2164354994, 0.0)\mathring{A} \end{aligned} \tag{2.2}$$

Because graphene is a two dimensional material, the third lattice vector is chosen of norm 1. The parameter values listed above, have been chosen to correspond to those used for the force constant calculations provide by Sangyeop Lee (with the exception of the $z$-direction lattice vector) and they are reasonable for graphene [81, 14].

This representation of the crystal as a lattice and a basis provides a description that naturally includes the symmetry of the lattice. For example, each atom can uniquely be identified by $\boldsymbol{l}$, a vector pointing to the center of the unit cell, and $\boldsymbol{b}$, the position of the $b$th atom in the basis relative to the center of the unit cell. In other words, the equilibrium position of the $b$th atom in the $l$th unit cell is given by

$$\boldsymbol{x}(\boldsymbol{lb}) = \boldsymbol{l} + \boldsymbol{b}. \tag{2.3}$$

A primitive translation vector is a linear combination of the lattice vectors that maps from one point on the lattice to another point which has identical surroundings

$$T = n_1\boldsymbol{a}_1 + n_2\boldsymbol{a}_2 + n_3\boldsymbol{a}_3 \tag{2.4}$$

where $n_1$, $n_2$, $n_3$ are integers. In the case of graphene, $n_3 = 0$. The Wigner-Seitz unit cell (which contains the complete basis, but no duplication) is shown in Figure 2-1. For graphene the unit cell has an area

$$A_{\text{uc}} = |\boldsymbol{a}_1 \cdot (\boldsymbol{a}_2 \times \boldsymbol{a}_3)| = \frac{\sqrt{3}a_{\text{lat}}^2}{2} \tag{2.5}$$

where $A_{\text{uc}}$ is the area of the unit cell in direct space. Calculations of spatially homogenous materials need be performed for only one such unit cell, which will be important in the derivations later in this chapter.

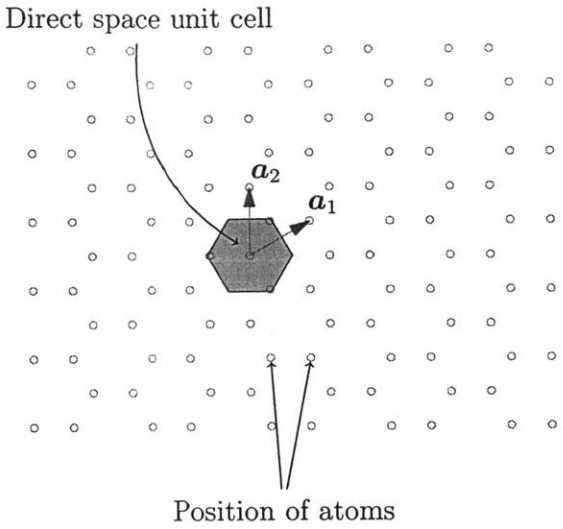


Figure 2-1: Direct space atomic positions (circles), unit cell, and lattice vectors.

## 2.2 Reciprocal Lattice

This work is focused on phonon transport. As phonons are related to the Fourier transform of lattice vibrations, it will also be necessary to describe the reciprocal space lattice. The basis vectors of the reciprocal lattice are [115]

$$\begin{aligned} \boldsymbol{b}_{\text{lat},1} &= \frac{2\pi}{\Omega}(\boldsymbol{a}_2 \times \boldsymbol{a}_3) \\ \boldsymbol{b}_{\text{lat},2} &= \frac{2\pi}{\Omega}(\boldsymbol{a}_3 \times \boldsymbol{a}_1) \\ \boldsymbol{b}_{\text{lat},3} &= \frac{2\pi}{\Omega}(\boldsymbol{a}_1 \times \boldsymbol{a}_2) \end{aligned} \tag{2.6}$$

and the area of the graphene reciprocal unit cell is $S_{\text{uc}} = \frac{a_{\text{lat}}}{2\pi}|\boldsymbol{a}_1 \cdot (\boldsymbol{a}_2 \times \boldsymbol{a}_3)|$ [115]—specifically,

$$S_{\text{uc}} = \frac{4\pi^2}{A_{\text{uc}}}. \tag{2.7}$$

A reciprocal lattice vector is defined by the integers $m_1$, $m_2$, $m_3$ in the relation

$$\boldsymbol{G} = m_1\boldsymbol{b}_{\text{lat},1} + m_2\boldsymbol{b}_{\text{lat},2} + m_3\boldsymbol{b}_{\text{lat},3} \tag{2.8}$$

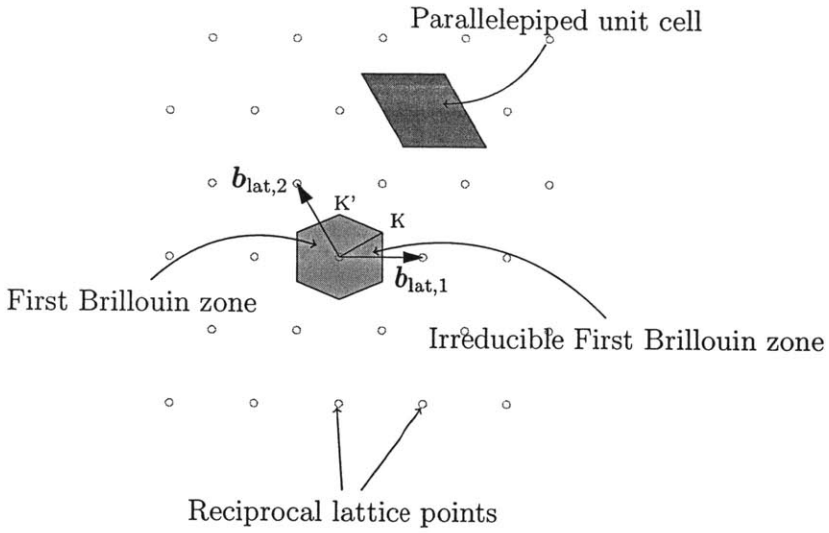


Figure 2-2: Reciprocal space lattice points and unit cells

Table 2.1: Special high symmetry points in the Brillouin zone. Wavevectors reported in units of $\frac{2\pi}{a_{lat}}$.

| Label | $q_x$ | $q_y$ |
|---|---|---|
| $\Gamma$ | 0 | 0 |
| M | $1/\sqrt{3}$ | 0 |
| K | $1/\sqrt{3}$ | 1/3 |
| K' | 0 | 2/3 |

which guarantees that the following relationship is satisfied

$$\exp(\mathrm{i}\boldsymbol{G}\cdot\boldsymbol{T}) = 1 \tag{2.9}$$

The first Brillouin zone, as shown in Figure 2-2, is the reciprocal space equivalent of the Wigner-Seitz cell. However, as a matter of computational convenience, this work will rely principally on the equivalent parallelepiped unit cell also shown in Figure 2-2.

Table 2.2: Symmetry operators in graphene from [62]

| Number | Symbol | Description |
|---|---|---|
| 1 | $E$ | Identity |
| 2 | $C_{6p}$ | 60 degree rotation about $\boldsymbol{a}_3$ |
| 3 | $C_{6m}$ | -60 degree rotation about$\boldsymbol{a}_3$ |
| 4 | $C_{3p}$ | 120 degree rotation about $\boldsymbol{a}_3$ |
| 5 | $C_{3m}$ | -120 degree rotation about$\boldsymbol{a}_3$ |
| 6 | $C_2$ | 180 degree rotation about$\boldsymbol{a}_3$ |
| 7 | $C_{p21}$ | 180 degree rotation about $\boldsymbol{a}_1 + 2\boldsymbol{a}_2$ |
| 8 | $C_{p22}$ | 180 degree rotation about $2\boldsymbol{a}_1 + \boldsymbol{a}_2$ |
| 9 | $C_{p23}$ | 180 degree rotation about $\boldsymbol{a}_1 + \boldsymbol{a}_2$ |
| 10 | $C_{pp21}$ | 180 degree rotation about $\boldsymbol{a}_1$ |
| 11 | $C_{pp22}$ | 180 degree rotation about $\boldsymbol{a}_2$ |
| 12 | $C_{pp23}$ | 180 degree rotation about $\boldsymbol{a}_1 + \boldsymbol{a}_2$ |

## 2.3 Symmetry operators

While the reciprocal space unit cell contains no duplication in terms of translational lattice vectors, it contains many points that are symmetrically equivalent. Each point can be mapped to a symmetrically equivalent point using a symmetry operator $\mathcal{S}$. Graphene has twelve symmetry operators listed in Table 2.2. Using these symmetry operators, the First Brillouin zone can be divided into twelve symmetrically equivalent irreducible Brillouin zones. One irreducible Brillouin zone is shown shaded in Figure 2-2.

### 2.3.1 A notational comment

In recognition that various notational conventions exist, we pause to explain the notation that we will use throughout this work. As already employed, vectors will be represented with a boldface symbol,

$$\boldsymbol{l} = (l_x, l_y, l_z) = l_x\hat{\boldsymbol{x}} + l_y\hat{\boldsymbol{y}} + l_z\hat{\boldsymbol{z}}, \tag{2.10}$$

where $\hat{\boldsymbol{x}}$, $\hat{\boldsymbol{y}}$, and $\hat{\boldsymbol{z}}$ are the unit vectors $(1,0,0)$, $(0,1,0)$, and $(0,0,1)$.

After quantization of the harmonic problem, we will need to refer discretely available phonon states identified by the wavevector $\boldsymbol{q}$ and the polarization $s$. Accordingly,

it will be appropriate and convenient to describe the properties of a state using a subscript notation $[\ldots]_\lambda = [\ldots]_{\boldsymbol{q}s} = [\ldots](\boldsymbol{q}s)$ (e.g. the frequency $\omega_\lambda = \omega_{\boldsymbol{q}s} = \omega(\boldsymbol{q}s)$).

When referring to an element of a vector state property (e.g. $\boldsymbol{v}_\lambda$), we will use the first subscript to represent cartesian direction and a comma to separate the second subscript for the state—for example,

$$\boldsymbol{v}_\lambda = v_{x,\lambda}\hat{\boldsymbol{x}} + v_{y,\lambda}\hat{\boldsymbol{y}} + v_{z,\lambda}\hat{\boldsymbol{z}}. \tag{2.11}$$

Later in this work, the wavevector space will be treated as continuous and summations will be converted to integrations, which for the two dimensional case is accomplished with the relation

$$\sum_{\boldsymbol{q}} \approx \frac{A_{\text{uc}}}{4\pi^2\delta} \int \mathrm{d}^2\boldsymbol{q}. \tag{2.12}$$

To numerically evaluate these integrals, we will discretize reciprocal space with a grid. We will refer to the $i$th grid point as a state having wavevector $\boldsymbol{q}_i$ and polarization $s_i$ (or in short $\lambda_i$). When referring to the discretization, we will use the subscript $i$ (or $j$ or $k$) in place of the quantum index $\lambda$—for example, $\boldsymbol{v}_i = v_{x,i}\hat{\boldsymbol{x}} + v_{y,i}\hat{\boldsymbol{y}} + v_{z,i}\hat{\boldsymbol{z}}$ is the velocity associated with the $i$th state of our discretization of reciprocal space, $\lambda_i$.

Finally, we will use particles to discretize the distribution function for integration of the Boltzmann equation. The $i$th particle will reside at one of the grid point states and will have the properties of that state (e.g. $\boldsymbol{q}_i$, $s_i$, and frequency $\omega_i = \omega(\boldsymbol{q}_i s_i)$) as well as a position $\boldsymbol{x}_i$. In this manner, whether performing a numerical integration using the grid or the particles, the notation will be the same—for example,

$$\sum_s \int \mathrm{d}^2\boldsymbol{q}\omega(\boldsymbol{q}s) \propto \sum_i \omega_i. \tag{2.13}$$

We will alway refer to phonon states and the discretizations using an index (e.g. $\omega_i$) and not a boldface vector notation (e.g. $\boldsymbol{\omega}$), with one exception that will be explained in the text. These matters will be reiterated when each is introduced in the course of this thesis.

## 2.4 Lattice dynamics

The following derivation of lattice dynamics is presented, which closely adheres to Srivastava's work [115]. Lattice vibrations, which are the principal carriers of thermal energy in graphene, can be described in terms of displacements of the atoms from their equilibrium positions. The component in the $\alpha$ direction of such a displacement for the $b$th basis atom in the $l$th unit cell will be denoted $u_\alpha(\boldsymbol{lb})$.

When atoms are displaced from their equilibrium location, the potential energy of the crystal rises and the Taylor series expansion of the potential energy is

$$\begin{aligned}\mathcal{V} &= \mathcal{V}_0 + \sum_{\boldsymbol{lb},\alpha} \left.\frac{\partial \mathcal{V}}{\partial u_\alpha(\boldsymbol{lb})}\right|_0 u_\alpha(\boldsymbol{lb}) + \frac{1}{2}\sum_{\boldsymbol{lb},\boldsymbol{l'b'},\alpha\beta} \left.\frac{\partial^2 \mathcal{V}}{\partial u_\alpha(\boldsymbol{lb})u_\beta(\boldsymbol{l'b'})}\right|_0 u_\alpha(\boldsymbol{lb})u_\beta(\boldsymbol{l'b'}) \\ &\quad + \frac{1}{3!}\sum_{\boldsymbol{lb},\boldsymbol{l'b'},\boldsymbol{l''b''},\alpha\beta\gamma} \left.\frac{\partial^3 \mathcal{V}}{\partial u_\alpha(\boldsymbol{lb})u_\beta(\boldsymbol{l'b'})u_\gamma(\boldsymbol{l''b''})}\right|_0 u_\alpha(\boldsymbol{lb})u_\beta(\boldsymbol{l'b'})u_\gamma(\boldsymbol{l''b''}) \\ &\quad + \ldots \qquad (2.14) \\ &= \mathcal{V}_0 + \mathcal{V}_1 + \mathcal{V}_2 + \mathcal{V}_3 + \ldots\end{aligned}$$

where $\alpha, \beta, \gamma$ are cartesian directions. Because at equilibrium the net force on each atom is zero, the first derivative is zero. The second and third derivatives represent the "force" constants of the system

$$\Phi_{\alpha\beta}(\boldsymbol{lb},\boldsymbol{l'b'}) = \left.\frac{\partial^2 \mathcal{V}}{\partial u_\alpha(\boldsymbol{lb})u_\beta(\boldsymbol{l'b'})}\right|_0 \qquad (2.15)$$

and

$$\Psi_{\alpha\beta\gamma}(\boldsymbol{lb},\boldsymbol{l'b'},\boldsymbol{l''b''}) = \left.\frac{\partial^3 \mathcal{V}}{\partial u_\alpha(\boldsymbol{lb})u_\beta(\boldsymbol{l'b'})u_\gamma(\boldsymbol{l''b''})}\right|_0 . \qquad (2.16)$$

### 2.4.1 Harmonic terms

The vibrational modes defined by their frequencies and polarization vectors arise from an analysis of the equation of motion of the lattice atoms, which for atom $\boldsymbol{lb}$ can be

written as

$$m_b \ddot{u}_\alpha(lb) = -\sum_{l'b'\beta} \Phi_{\alpha\beta}(lb, l'b') u_\beta(l'b'), \tag{2.17}$$

and this has a solution of the form

$$u(lb) = \frac{1}{\sqrt{m_b}} \sum_q U(qb) \exp(i(q \cdot l - \omega t)), \tag{2.18}$$

where $q$ is a wavevector. Due to boundary conditions, the allowable wavevectors are discrete, but it is computationally unfeasible to represent explicitly all allowable wavevectors. Consequently, the discrete wavevector space will later be converted to a continuous one and then discretized again for numerical integration. In (2.18) $q$ and $b$ are indices, but to avoid switching between subscript and parentheses notation, $(qb)$ will be allowed to represent an index as well as functional dependence for a continuous variable. By exploiting translational symmetry and defining a relative lattice position $h = l' - l$, Equation (2.17) can be rewritten as

$$\omega^2 U_\alpha(qb) = \sum_{hb'\beta} \frac{1}{\sqrt{m_b m_{b'}}} \Phi_{\alpha\beta}(0b, hb') U_\beta(qb') \exp(iq' \cdot h) \tag{2.19}$$

which leads to the characteristic equation

$$\left| D_{\alpha\beta}(qbb') - \omega^2 \delta_{\alpha\beta} \delta_{bb'} \right| = 0. \tag{2.20}$$

The dynamical matrix is given by

$$D_{\alpha\beta}(qbb') = \frac{1}{\sqrt{m_b m_{b'}}} \sum_h \Phi_{\alpha\beta}(0b, hb') \exp(ih \cdot q). \tag{2.21}$$

In this work, Equation (2.21) is evaluated directly from the second order force constants calculated from density functional theory (DFT) by Sangyeop Lee and the diagonalization is performed by the LAPACK library for Fortran, which results in phonon frequencies $\omega(qs)$ and eigenvectors $e(b|qs)$ for polarization $s$. The polarizations are labeled: out-of-plane acoustic (ZA), transverse acoustic (TA), longitudinal

acoustic (LA), out-of-plane optical (ZO), transverse optical (TO) and longitudinal optical (LO), referring to the motion of the atoms with respect to the wavevector near the zone center and with respect to the other atom in the unit cell.

Although the anharmonic terms can be expected to slightly modify this dispersion relation [72, 31, 33, 37], the effect of the anharmonic terms is relatively small [33], and beyond the scope of this analysis.

The eigenvalues and vectors returned by the diagonalization are unsorted, but in order to calculate the phonon group velocities,

$$\boldsymbol{v}(\boldsymbol{q}s) = \nabla_{\boldsymbol{q}}\omega(\boldsymbol{q}s), \tag{2.22}$$

from numerical differentiation, there must be a reliable and automated way to sort the dispersion relation by branch. This can be accomplished by comparing the eigenvectors at a point $\boldsymbol{q}$ with a known correct sorting to a point $\boldsymbol{q}'$ nearby that needs to be sorted. The sorting of the branches of $\boldsymbol{q}'$ is chosen in order to align the eigenvectors by maximizing

$$\left|\sum_{\alpha,b} e_\alpha(b|\boldsymbol{q}s)e^*_\alpha(b|\boldsymbol{q}'s)\right|.$$

This procedure works most reliably when the two points $\boldsymbol{q}$ and $\boldsymbol{q}'$ lie on a line that also crosses through the $\Gamma$ point ($\boldsymbol{q} = \boldsymbol{0}$), but may still fail to properly sort the LO and TO branches in the region where branch cross or nearly cross (points of inflection). This is easily remedied by sorting the LO and TO branches such that $\omega(\boldsymbol{q}\text{LO}) < \omega(\boldsymbol{q}\text{TO})$– Figure 2-4 shows a zoomed in view of the apparent branch crossing in Figure 2-3 to reveal that the LO and TO branches do *not* cross[1]. In order to provide reference points of known correct sorting, branches are sorted by the magnitude of $\omega$ near the $\Gamma$ point– specifically $||\boldsymbol{q}|| < \frac{2\pi}{3\sqrt{3}a_{\text{lat}}}$–without reference to any neighboring point. Eigenvalues and eigenvectors are stored for points along lines emanating outward from the $\Gamma$ point, which are then used as references for later calculation of eigenvalues and eigenvectors

[1]While this sorting of branches disagrees with [81] and [64] and the references therein, it is the only approach reconcilable with the data. Since the force constants are treated as inputs, the authors refrain from commenting on which sorting is physically correct.

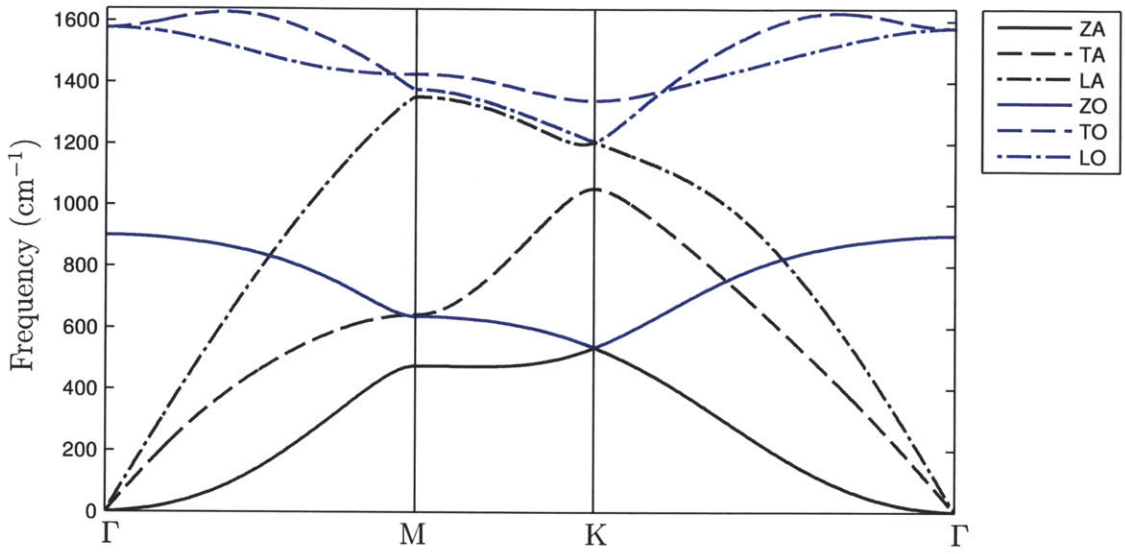


Figure 2-3: Phonon dispersion relation sorted by branch along high symmetry directions.

for arbitrary $\boldsymbol{q}$.

As can be seen from Figure 2-5, this procedure works consistently for the data set used in this study. The values of the dispersion relation at high symmetry points shown in Table 2.3 are in good agreement with theoretical and experimental investigations of the graphene dispersion relation [64, 81], which provides validation of the second order force constants used in this study. Group velocities are calculated using a centered finite difference method–the step size is chosen to be sufficiently small to eliminate artifacts in the velocity calculation.

### 2.4.2 Anharmonic terms

A partial validation of the third order force constant used in this work can be obtained through the Grüneisen parameter. The Grüneisen parameter is related to the derivative of the dispersion relation with respect to the volume. Although it was originally proposed for simpler models, it can be generalized to the anisotropic case as [115]

$$\gamma(\boldsymbol{q}s) = -\frac{V}{\omega(\boldsymbol{q}s)}\frac{\mathrm{d}\omega(\boldsymbol{q}s)}{\mathrm{d}V}. \tag{2.23}$$

Table 2.3: Dispersion relation at high symmetry points in units of $cm^{-1}$.

| Source | $a_{lat}$ | Exchange-correlation | Parameterization |
|---|---|---|---|
| This work | 2.4328709987Å | LDA | PZ [94] |
| Reference [81] | 2.46Å | GGA | PBE [95] |
| Reference [64] | 2.447 – 2.457Å | LDA & GGA | various |

| Point | ZA | TA | LA | ZO | TO | LO |
|---|---|---|---|---|---|---|
| This work: | | | | | | |
| Γ | 0 | 0 | 0 | 900.5 | 1577.4 | 1577.4 |
| M | 475.7 | 642.0 | 1352.9 | 636.7 | 1426.9 | 1377.1 |
| K=K' | 535.5 | 1053.7 | 1205.6 | 535.6 | 1340.9 | 1206.2 |
| Reference [81]: | | | | | | |
| Γ | 0 | 0 | 0 | 881 | 1554 | 1554 |
| M | 471 | 626 | 1328 | 635 | 1390 | 1340 |
| K=K' | 535 | 997 | 1213 | 535 | 1288 | 1213 |
| Reference [64]: | | | | | | |
| Γ | 0 | 0 | 0 | 825-896 | 1569-1597 | 1569-1597 |
| M | 472-476 | 626-634 | 1315-1347 | 636-640 | 1396-1442 | 1346-1380 |
| K=K' | 535-539 | 994-1004 | 1221-1246 | 535-539 | 1289-1371 | 1220-1246 |

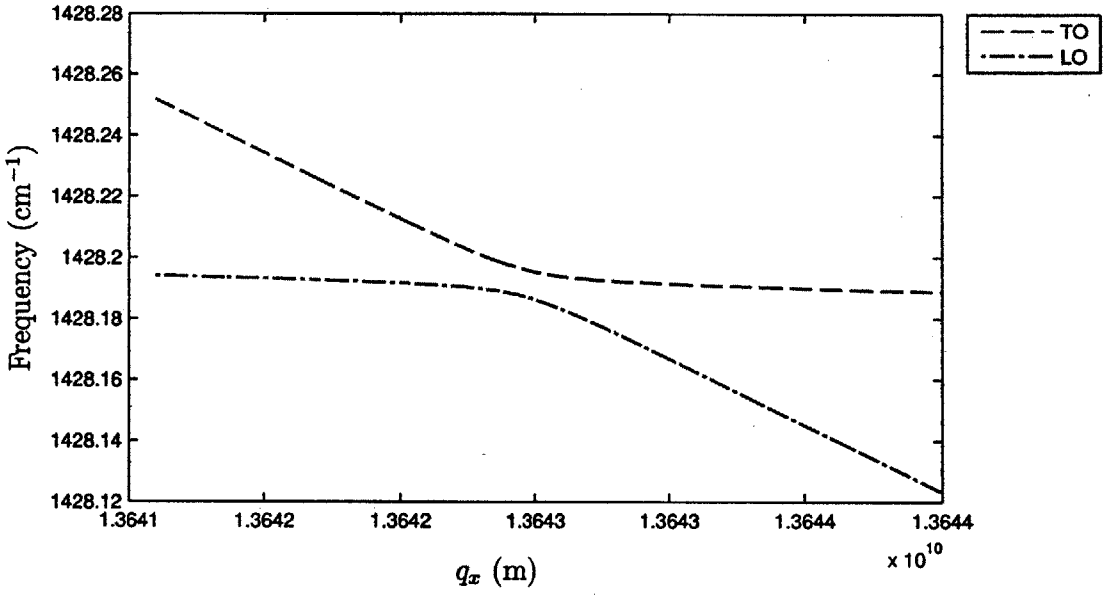


Figure 2-4: Detail of the LO TO sorting near the point of inflection along the line $\Gamma$ to M or $q_y = \epsilon$, where $\epsilon$ is an infinitesimal perturbation from 0 to show the gap opening.

The Grüneisen parameter can also be calculated from the force constants directly (see [124, 15, 33] and specifically for graphene [112])

$$\begin{aligned}\gamma(\boldsymbol{qs}) &= -\frac{1}{4(\omega(\boldsymbol{qs}))^2}\sum_{\alpha\beta\gamma}\sum_{\boldsymbol{bb'b''}}\sum_{\boldsymbol{h'h''}}(\Phi_{\alpha\beta\gamma}(\boldsymbol{0b},\boldsymbol{h'b'},\boldsymbol{h''b''})) \\ &\quad\times\frac{e^*_\alpha(\boldsymbol{b}|\boldsymbol{qs})e^*_\beta(\boldsymbol{b'}|\boldsymbol{qs})}{M_{\text{atom}}}\exp\left(i\boldsymbol{q}\cdot\boldsymbol{h'}\right)x_\gamma(\boldsymbol{h''b''}). \qquad (2.24)\end{aligned}$$

The Grüneisen parameter $\gamma(\boldsymbol{qs})$ should not be confused with the cartesian coordinate index, subscript $\gamma$. The Grüneisen parameter has previously been calculated from DFT [81] and the results of that calculation agree well with the current model (see Figure 2-8).

Although the Grüneisen parameter can be linked to the strength of three phonon scattering through various approximations [56, 57, 59, 48], the resulting model is unsatisfactory for thermal transport calculations in graphene [112]. Instead, the ab initio thermal transport procedure will be used to evaluate phonon scattering rates [87, 77]. The ab initio scattering operator is derived through various transformations of the

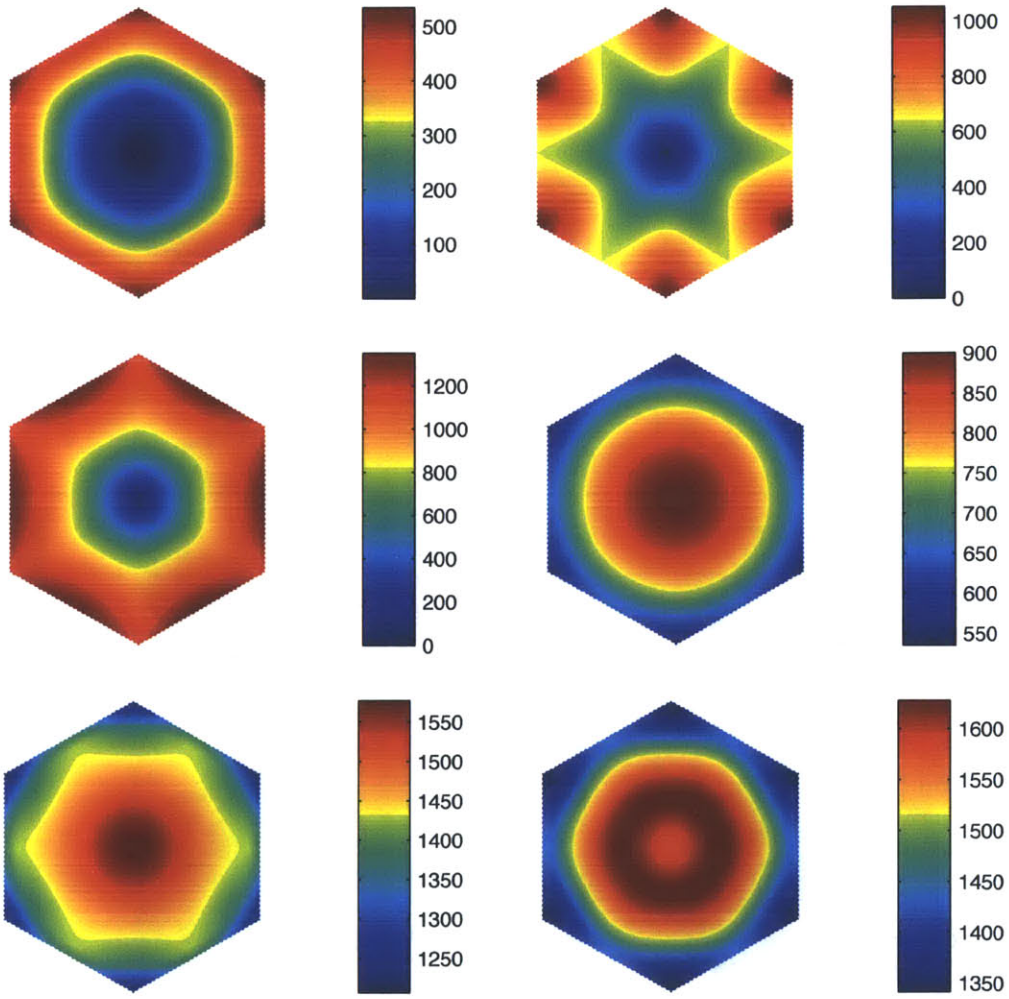


Figure 2-5: Phonon dispersion relation in FBZ sorted by branch, as opposed to incorrect sorted by magnitude (e.g. [2]). Figure shows from left to right ZA, TA (top row); LA, ZO (middle row); TO, LO (bottom row). Units are $cm^{-1}$.

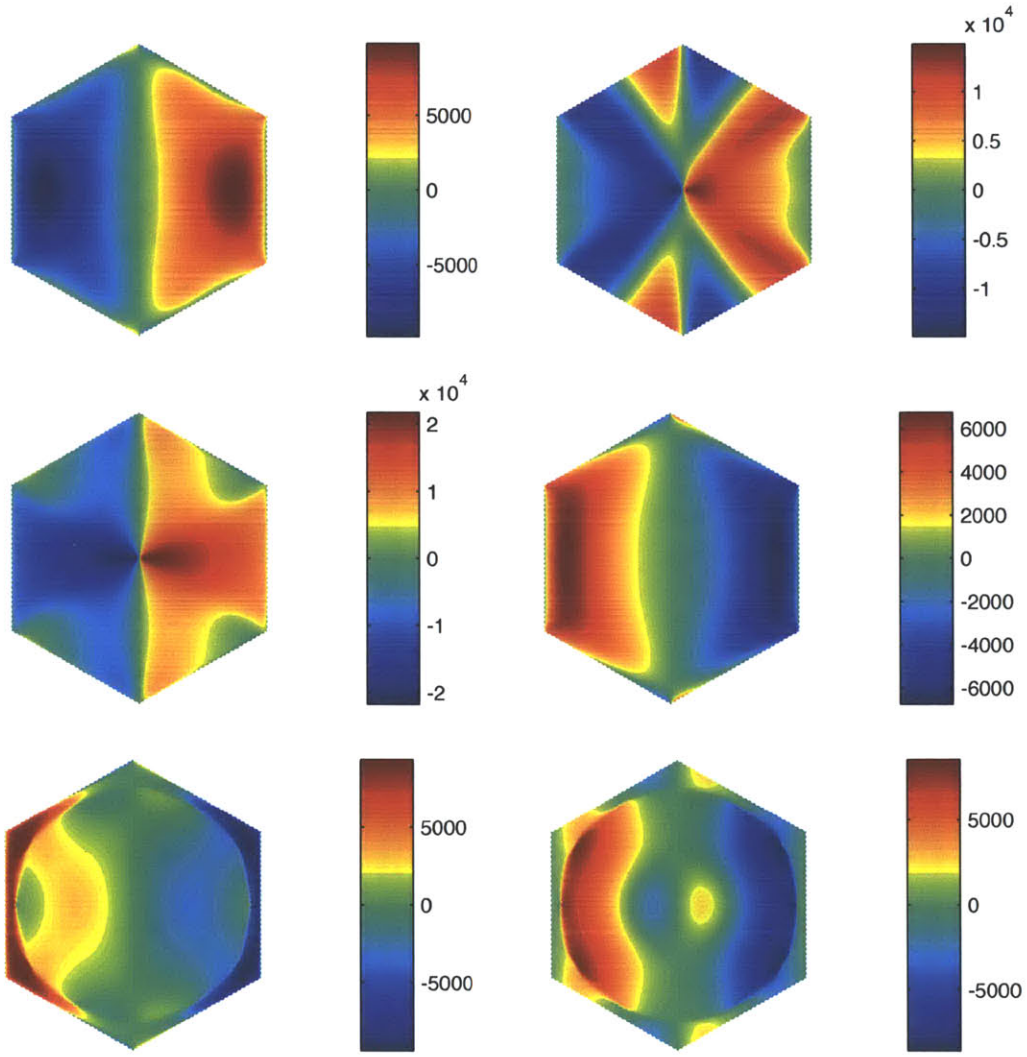


Figure 2-6: Phonon group velocity in the $x$ direction. Figure shows from left to right ZA, TA (top row); LA, ZO (middle row); TO, LO (bottom row). Units are m/s.

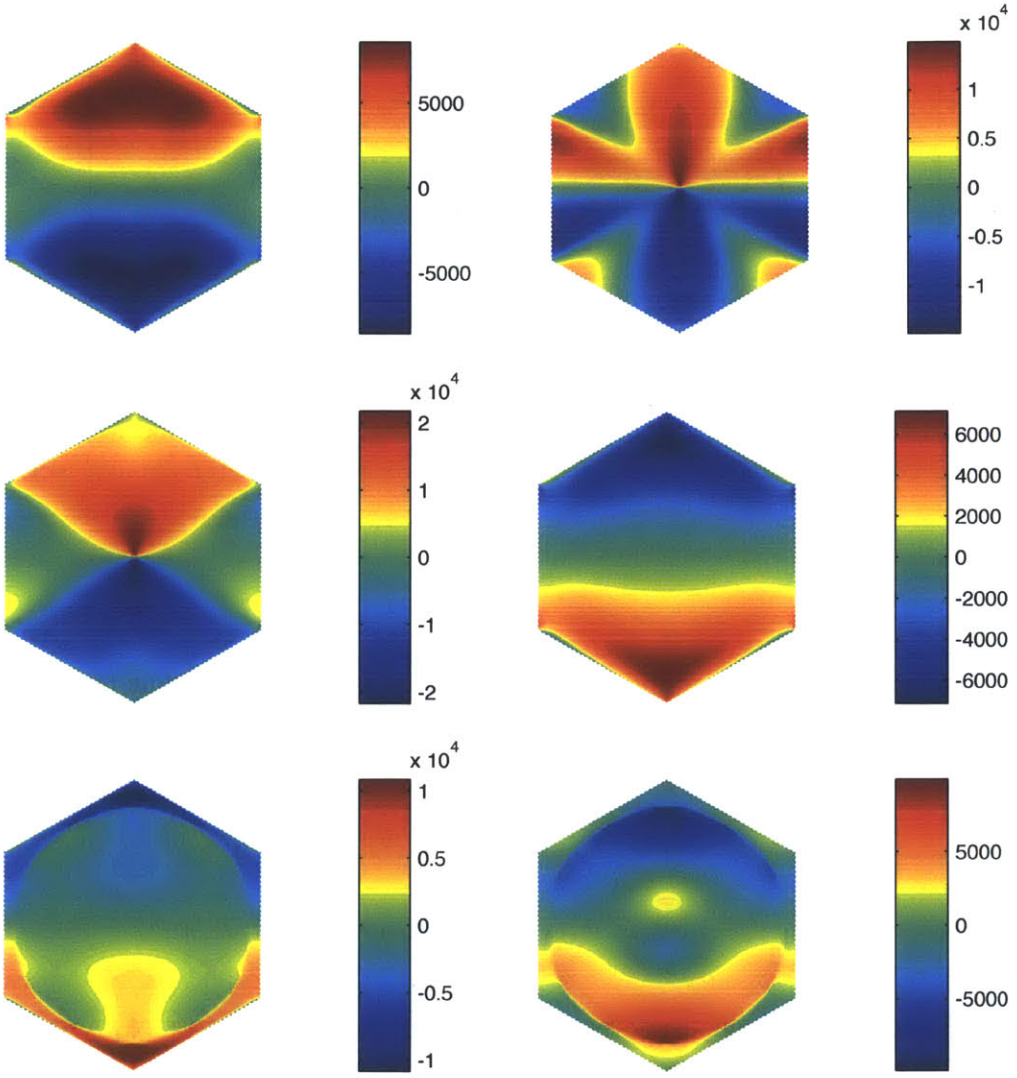


Figure 2-7: Phonon group velocity in the $y$ direction. Figure shows from left to right ZA, TA (top row); LA, ZO (middle row); TO, LO (bottom row). Units are m/s.

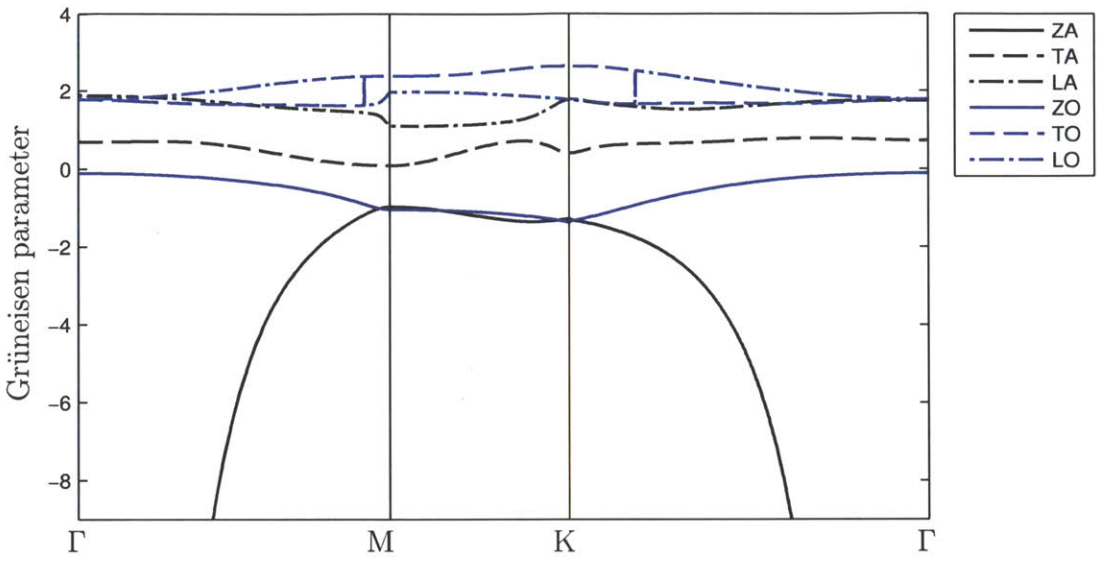


Figure 2-8: The Grüneisen parameter calculated from the force constants used in this work and Equation (2.24), which are in good agreement with those from [81] with the exception of the crossing in the optical branches due to the sorting in this work.

anharmonic energy term. The details can be found in [115, 40], but for brevity, only the result is presented here, namely

$$\begin{aligned}\mathcal{V}_3 &= \frac{i}{3!}\sum_{\boldsymbol{qs},\boldsymbol{q's'},\boldsymbol{q''s''}} \delta_{\boldsymbol{G},\boldsymbol{q}+\boldsymbol{q'}+\boldsymbol{q''}}\tilde{V}_3(\boldsymbol{qs},\boldsymbol{q's'},\boldsymbol{q''s''}) \\ &\quad (a^\dagger_{\boldsymbol{qs}} - a_{-\boldsymbol{qs}})(a^\dagger_{\boldsymbol{q's'}} - a_{-\boldsymbol{q's'}})(a^\dagger_{\boldsymbol{q''s''}} - a_{-\boldsymbol{q''s''}}) \qquad (2.25)\end{aligned}$$

This expression includes the creation and annihilation operators $a^\dagger_{\boldsymbol{qs}}$ and $a_{\boldsymbol{qs}}$, which arise from the quantization of the phonon system [35] and have the useful properties of creating, deleting, or returning the number of quantum particles when integrated with the state. In ket notation this is

$$a^\dagger_{\boldsymbol{qs}}\,|n(\boldsymbol{qs})\rangle = \sqrt{n(\boldsymbol{qs})+1}\,|n(\boldsymbol{qs})+1\rangle \qquad (2.26)$$

$$a_{\boldsymbol{qs}}\,|n(\boldsymbol{qs})\rangle = \sqrt{n(\boldsymbol{qs})}\,|n(\boldsymbol{qs})-1\rangle \qquad (2.27)$$

$$a^\dagger_{\boldsymbol{qs}}a_{\boldsymbol{qs}}\,|n(\boldsymbol{qs})\rangle = n(\boldsymbol{qs})\,|n(\boldsymbol{qs})\rangle \qquad (2.28)$$

Equation (2.25) also introduced $\tilde{V}_3$,

$$\tilde{V}_3(qs,q's',q''s'') = \frac{1}{\sqrt{N_0}} \sum_{bb'b'',\alpha\beta\gamma} \left( \frac{\hbar^3}{8m_b m_{b'} m_{b''} \omega(qs)\omega(q's')\omega(q''s'')} \right)^{1/2} e_\alpha(b|qs) e_\beta(b'|q's') e_\gamma(b''|q''s'') \Psi_{\alpha\beta\gamma}(qb,q'b',q''b'') \quad (2.29)$$

which is the projection along the eigenvectors of the Fourier transform of the third order force constants. In (2.29) $N_0$ is the number of unit cells in the calculation and the Fourier transform of the force constants is

$$\begin{aligned} \Psi_{\alpha\beta\gamma}(qb,q'b',q''b'') &= \sum_{ll'l''} \Psi(lb,l'b',l'',b'') e^{ib\cdot l} e^{ib'\cdot l'} e^{iq''\cdot l''} \\ &= \sum_{h'h''} \Psi(0b,h'b',h'',b'') e^{ib'\cdot h'} e^{iq''\cdot h''} \end{aligned} \quad (2.30)$$

At a later stage, it will be important to consider the symmetry of the interaction term $\tilde{V}_3$. From (2.16), it can be seen that $|\tilde{V}_3|$ is invariant under a permutation of arguments. Furthermore, due to the symmetry of the graphene dispersion relation $|\tilde{V}_3(q,q',q'')| = |\tilde{V}_3(-q,-q',-q'')|$. Another important implication of symmetry is that all force constants must have an even number of $z$-direction terms (that is of the three indices on $\Psi_{\alpha\beta\gamma}$, only zero or two can be $z$), which will lead to the selection rule that three phonon scattering must include an even number (including 0) of out-of-plane modes [71].

## 2.5 Phonon Scattering

The results quoted in the preceding section presented the interaction strength of three phonon coupling, $\mathcal{V}_3$. The golden rule states that the transition rate from an initial state $i$ with energy $E_i$ to a final state $f$ with energy $E_f$ is given by [115]

$$P_i^f = \frac{2\pi}{\hbar} |\langle f|\mathcal{V}_3|i\rangle|^2 \delta(E_f - E_i) \quad (2.31)$$

In the three phonon context, the initial state is described by the occupation number of the three phonon states $n(\boldsymbol{q}s)$, $n(\boldsymbol{q}'s')$, and $n(\boldsymbol{q}''s'')$. Given any initial $n(\boldsymbol{q}s)$, $n(\boldsymbol{q}'s')$, and $n(\boldsymbol{q}''s'')$, the final phonon state is limited by the $\mathcal{V}_3$ term–when this term is zero, no coupling occurs and the transition rate is zero. For example, the delta function in (2.25), $\delta_{\boldsymbol{G},\boldsymbol{q}+\boldsymbol{q}'+\boldsymbol{q}''} = \delta(\boldsymbol{q}+\boldsymbol{q}'+\boldsymbol{q}''-\boldsymbol{G})$, ensures that the coupled phonon states satisfy this relation

$$\boldsymbol{q}+\boldsymbol{q}'+\boldsymbol{q}''=\boldsymbol{G} \tag{2.32}$$

where $\boldsymbol{q}$, $\boldsymbol{q}'$, $\boldsymbol{q}''$ are restricted to the first Brillouin zone (or the parallelepiped reciprocal space unit cell) and $\boldsymbol{G}$ is a reciprocal lattice vector (including $\mathbf{0}$). However, these states (i.e. $\boldsymbol{q}s, \boldsymbol{q}'s', \boldsymbol{q}''s''$) are not necessarily the phonon states that experience a change in occupancy. Specifically, the creation and annihilation operators,

$$(a^\dagger_{\boldsymbol{q}s} - a_{-\boldsymbol{q}s})(a^\dagger_{\boldsymbol{q}'s'} - a_{-\boldsymbol{q}'s'})(a^\dagger_{\boldsymbol{q}''s''} - a_{-\boldsymbol{q}''s''}),$$

identify other states which differ by a wavevector sign whose occupancy is changed by the coupling. By expanding the creation and annihilation terms,

$$\begin{aligned} &a^\dagger_{\boldsymbol{q}s}a^\dagger_{\boldsymbol{q}'s'}a^\dagger_{\boldsymbol{q}''s''} - a^\dagger_{\boldsymbol{q}s}a^\dagger_{\boldsymbol{q}'s'}a_{-\boldsymbol{q}''s''} - a^\dagger_{\boldsymbol{q}s}a_{-\boldsymbol{q}'s'}a^\dagger_{\boldsymbol{q}''s''} + a^\dagger_{\boldsymbol{q}s}a_{-\boldsymbol{q}'s'}a_{-\boldsymbol{q}''s''} \\ &-a_{-\boldsymbol{q}s}a^\dagger_{\boldsymbol{q}'s'}a^\dagger_{\boldsymbol{q}''s''} + a_{-\boldsymbol{q}s}a^\dagger_{\boldsymbol{q}'s'}a_{-\boldsymbol{q}''s''} + a_{-\boldsymbol{q}s}a_{-\boldsymbol{q}'s'}a^\dagger_{\boldsymbol{q}''s''} - a_{-\boldsymbol{q}s}a_{-\boldsymbol{q}'s'}a_{-\boldsymbol{q}''s''} \end{aligned} \tag{2.33}$$

it can be seen that only the first term changes the occupancy of the three states $\boldsymbol{q}s$, $\boldsymbol{q}'s'$, and $\boldsymbol{q}''s''$ by creating a new phonon in each. However, on consideration of the energy delta function in (2.31), creation of three phonons cannot satisfy energy conservation, so this process (and similarly the last term of (2.33)) is impossible. The remaining terms are of one of two types. In type I terms, two phonons are deleted and a third is created. Considering (2.32), this gives rise to the momentum conservation statement

$$-\boldsymbol{q}-\boldsymbol{q}'+\boldsymbol{q}''=\boldsymbol{G} \quad \text{(Type I)} \tag{2.34}$$

The other type I terms are a permutation with respect to the states of this one. From (2.31), energy conservation takes the form

$$-\omega(-\boldsymbol{q}s) - \omega(-\boldsymbol{q}s') + \omega(\boldsymbol{q}''s'') = 0 \quad \text{(Type I)} \tag{2.35}$$

For type II processes (deletion of one phonon and creation of two) momentum conservation is

$$-\boldsymbol{q} + \boldsymbol{q}' + \boldsymbol{q}'' = \boldsymbol{G} \quad \text{(Type II)} \tag{2.36}$$

From (2.31), energy conservation can then be expressed as

$$-\omega(-\boldsymbol{q}s) + \omega(\boldsymbol{q}s') + \omega(\boldsymbol{q}''s'') = 0 \quad \text{(Type II)} \tag{2.37}$$

Since the coupling between $\boldsymbol{q}s$, $\boldsymbol{q}'s'$, and $\boldsymbol{q}''s''$ changes the occupancy of the phonon states $\pm\boldsymbol{q}s$, $\pm\boldsymbol{q}'s'$, and $\pm\boldsymbol{q}''s''$, care must be exercised when calculating the interaction term for a three phonon scattering event.

After expanding the creation and annihilation terms and discarding the unphysical ones, expression (2.31) for type I processes becomes

$$\begin{aligned} P^{\boldsymbol{q}''s''}_{\boldsymbol{q}s,\boldsymbol{q}'s'} &= \frac{2\pi}{\hbar^2} |\langle n(\boldsymbol{q}s)-1, n(\boldsymbol{q}'s')-1, n(\boldsymbol{q}''s'')+1|\mathcal{V}_3(-\boldsymbol{q}s, -\boldsymbol{q}'s', \boldsymbol{q}''s'')| \ldots \\ &\quad n(\boldsymbol{q}s), n(\boldsymbol{q}'s'), n(\boldsymbol{q}''s'')\rangle|^2 \, \delta(-\omega(\boldsymbol{q}s) - \omega(\boldsymbol{q}'s') + \omega(\boldsymbol{q}''s'')) \\ &= \frac{2\pi}{\hbar^2} |\tilde{\mathcal{V}}_3(-\boldsymbol{q}s, -\boldsymbol{q}'s', \boldsymbol{q}''s'')|^2 n(\boldsymbol{q}s) n(\boldsymbol{q}'s') (n(\boldsymbol{q}''s'')+1) \\ &\quad \times \delta(-\omega(\boldsymbol{q}s) - \omega(\boldsymbol{q}'s') + \omega(\boldsymbol{q}''s'')) \delta(-\boldsymbol{q} - \boldsymbol{q}' + \boldsymbol{q}'' + \boldsymbol{G}). \end{aligned} \tag{2.38}$$

Similarly for type II processes,

$$\begin{aligned} P^{\boldsymbol{q}'s',\boldsymbol{q}''s''}_{\boldsymbol{q}s} &= \frac{2\pi}{\hbar^2} |\langle n(\boldsymbol{q}s)-1, n(\boldsymbol{q}'s')+1, n(\boldsymbol{q}''s'')+1|\mathcal{V}_3(-\boldsymbol{q}s, \boldsymbol{q}'s', \boldsymbol{q}''s'')| \\ &\quad n(\boldsymbol{q}s), n(\boldsymbol{q}'s'), n(\boldsymbol{q}''s'')\rangle|^2 \, \delta(-\omega(\boldsymbol{q}s) + \omega(\boldsymbol{q}'s') + \omega(\boldsymbol{q}''s'')) \\ &= \frac{2\pi}{\hbar^2} |\tilde{\mathcal{V}}_3(-\boldsymbol{q}s, \boldsymbol{q}'s', \boldsymbol{q}''s'')|^2 n(\boldsymbol{q}s) (n(\boldsymbol{q}'s')+1) (n(\boldsymbol{q}''s'')+1) \\ &\quad \times \delta(-\omega(\boldsymbol{q}s) + \omega(\boldsymbol{q}'s') + \omega(\boldsymbol{q}''s'')) \delta(-\boldsymbol{q} + \boldsymbol{q}' + \boldsymbol{q}'' + \boldsymbol{G}). \end{aligned} \tag{2.39}$$

The factors of 3! canceled due to the summation of the equivalent terms in (2.33). These expressions for the rate that phonons leave or enter a state due to three phonon scattering will be used in the scattering operator of the phonon Boltzmann equation.

# Chapter 3

# Boltzmann Equation

The preceding chapter ended with expressions for the three phonon scattering rate based on the distribution function $n(\boldsymbol{q}s)$. The complete dynamics of the distribution function can be described as a balance between advection and scattering effects (including but not limited to the three phonon scattering). This concept was put in a mathematical framework by Peierls in 1929 in the form of the phonon Boltzmann equation [89, 124], which is typically valid in devices with lengths larger than $10-30$ nm [97, 26, 106, 27].

$$\frac{\partial n(\boldsymbol{q}s)}{\partial t} + \boldsymbol{v}(\boldsymbol{q}s) \cdot \nabla_{\boldsymbol{x}} n(\boldsymbol{q}s) = \left[\frac{\partial n(\boldsymbol{q}s)}{\partial t}\right]_{\text{scatt}} \tag{3.1}$$

The left-hand side of this equation describes ballistic advection of phonons, while the right-hand side is the significantly more complicated scattering operator. This chapter is devoted to the development of the theory for the state of the art iterative solutions methods of (3.1), as well as for the new simulation method that is the main contribution of this thesis.

## 3.1 Phonon scattering operator

The scattering rate due to three phonon processes can be derived by accounting for all scattering into and out of a phonon state $\boldsymbol{q}s$. Using (2.38) and (2.39) the change

in the occupation number with time due to three phonon scattering can be written as [115]

$$\begin{aligned}
\left[\frac{\partial n(\boldsymbol{q}s)}{\partial t}\right]_{\text{3-ph}} &= \sum_{\boldsymbol{q}'s',\boldsymbol{q}''s''}\left[\left(P^{\boldsymbol{q}s,\boldsymbol{q}'s'}_{\boldsymbol{q}''s''} - P^{\boldsymbol{q}''s''}_{\boldsymbol{q}s,\boldsymbol{q}'s'}\right) + \frac{1}{2}\left(P^{\boldsymbol{q}s}_{\boldsymbol{q}'s',\boldsymbol{q}''s''} - P^{\boldsymbol{q}'s',\boldsymbol{q}''s''}_{\boldsymbol{q}s}\right)\right] \\
&= \frac{2\pi}{\hbar^2}\sum_{\boldsymbol{q}'s',\boldsymbol{q}''s''}|\tilde{\mathcal{V}}_3(-\boldsymbol{q}s,-\boldsymbol{q}'s',\boldsymbol{q}''s'')|^2\delta(-\omega(\boldsymbol{q}s)-\omega(\boldsymbol{q}'s')+\omega(\boldsymbol{q}''s'')) \\
&\quad\times\delta(-\boldsymbol{q}-\boldsymbol{q}'+\boldsymbol{q}''+\boldsymbol{G}) \\
&\quad\times\big((n(\boldsymbol{q}s)+1)(n(\boldsymbol{q}'s')+1)n(\boldsymbol{q}''s'')-n(\boldsymbol{q}s)n(\boldsymbol{q}'s')(n(\boldsymbol{q}''s'')+1)\big) \\
&\quad+\frac{\pi}{\hbar^2}\sum_{\boldsymbol{q}'s',\boldsymbol{q}''s''}|\tilde{\mathcal{V}}_3(-\boldsymbol{q}s,\boldsymbol{q}'s',\boldsymbol{q}''s'')|^2\delta(-\omega(\boldsymbol{q}s)+\omega(\boldsymbol{q}'s')+\omega(\boldsymbol{q}''s'')) \\
&\quad\times\delta(-\boldsymbol{q}+\boldsymbol{q}'+\boldsymbol{q}''+\boldsymbol{G}) \\
&\quad\times\big((n(\boldsymbol{q}s)+1)n(\boldsymbol{q}'s')n(\boldsymbol{q}''s'')-n(\boldsymbol{q}s)(n(\boldsymbol{q}'s')+1)(n(\boldsymbol{q}''s'')+1)\big)
\end{aligned} \tag{3.2}$$

In practice, it is infeasible to explicitly simulate every phonon state because of their overwhelming number. Fortunately, due to the large number of states and their relative proximity when the physical dimensions of a semi-conductor are large enough, the summation can be converted to an integration

$$\begin{aligned}
\left[\frac{\partial n(\boldsymbol{q}s)}{\partial t}\right]_{\text{3-ph}} &= \frac{A_{\text{uc}}^2}{8\pi^3\hbar^2}\sum_{s',s''}\int \mathrm{d}^2\boldsymbol{q}'\int \mathrm{d}^2\boldsymbol{q}''|\tilde{\mathcal{V}}_3(-\boldsymbol{q}s,-\boldsymbol{q}'s',\boldsymbol{q}''s'')|^2 \\
&\quad\times\delta(-\omega(\boldsymbol{q}s)-\omega(\boldsymbol{q}'s')+\omega(\boldsymbol{q}''s''))\delta(-\boldsymbol{q}-\boldsymbol{q}'+\boldsymbol{q}''+\boldsymbol{G}) \\
&\quad\times\big((n(\boldsymbol{q}s)+1)(n(\boldsymbol{q}'s')+1)n(\boldsymbol{q}''s'')-n(\boldsymbol{q}s)n(\boldsymbol{q}'s')(n(\boldsymbol{q}''s'')+1)\big) \\
&\quad+\frac{A_{\text{uc}}^2}{16\pi^3\hbar^2}\sum_{s',s''}\int \mathrm{d}^2\boldsymbol{q}'\int \mathrm{d}^2\boldsymbol{q}''|\tilde{\mathcal{V}}_3(-\boldsymbol{q}s,\boldsymbol{q}'s',\boldsymbol{q}''s'')|^2 \\
&\quad\delta(-\omega(\boldsymbol{q}s)+\omega(\boldsymbol{q}'s')+\omega(\boldsymbol{q}''s''))\times\delta(-\boldsymbol{q}+\boldsymbol{q}'+\boldsymbol{q}''+\boldsymbol{G}) \\
&\quad\times\big((n(\boldsymbol{q}s)+1)n(\boldsymbol{q}'s')n(\boldsymbol{q}''s'')-n(\boldsymbol{q}s)(n(\boldsymbol{q}'s')+1)(n(\boldsymbol{q}''s'')+1)\big),
\end{aligned} \tag{3.3}$$

where $A_{\text{uc}}$ is the area of the direct space unit cell, and the integration is over the first Brillouin zone (see Section 2.2). Integration over $\boldsymbol{q}''$ can be eliminated by the

momentum conservation delta function, which has the properties

$$\frac{A_{\rm uc}}{4\pi^2}\int \mathrm{d}^2\boldsymbol{q}''\delta(\boldsymbol{q}''-\tilde{\boldsymbol{q}})=1 \tag{3.4}$$

and

$$\frac{A_{\rm uc}}{4\pi^2}\int \mathrm{d}^2\boldsymbol{q}'' f(\boldsymbol{q}'')\delta(\boldsymbol{q}''-\tilde{\boldsymbol{q}})=f(\tilde{\boldsymbol{q}}). \tag{3.5}$$

This results in a simpler expression

$$\begin{aligned}\left[\frac{\partial n(\boldsymbol{q}s)}{\partial t}\right]_{\text{3-ph}} &= \frac{A_{\rm uc}}{2\pi\hbar^2}\sum_{s',s''}\int \mathrm{d}^2\boldsymbol{q}'|\tilde{\mathcal{V}}_3(-\boldsymbol{q}s,-\boldsymbol{q}'s',\boldsymbol{q}''s'')|^2\delta(-\omega(\boldsymbol{q}s)-\omega(\boldsymbol{q}'s')+\omega(\boldsymbol{q}''s''))\\ &\times\big((n(\boldsymbol{q}s)+1)(n(\boldsymbol{q}'s')+1)n(\boldsymbol{q}''s'')-n(\boldsymbol{q}s)n(\boldsymbol{q}'s')(n(\boldsymbol{q}''s'')+1)\big)\\ &+\frac{A_{\rm uc}}{4\pi\hbar^2}\sum_{s',s''}\int \mathrm{d}^2\boldsymbol{q}'|\tilde{\mathcal{V}}_3(-\boldsymbol{q}s,\boldsymbol{q}'s',\boldsymbol{q}''s'')|^2\delta(-\omega(\boldsymbol{q}s)+\omega(\boldsymbol{q}'s')+\omega(\boldsymbol{q}''s''))\\ &\times\big((n(\boldsymbol{q}s)+1)n(\boldsymbol{q}'s')n(\boldsymbol{q}''s'')-n(\boldsymbol{q}s)(n(\boldsymbol{q}'s')+1)(n(\boldsymbol{q}''s'')+1)\big).\end{aligned} \tag{3.6}$$

Throughout this work, anytime the variable $\boldsymbol{q}''$ appears without explicit integration or explicit dependence upon another variable as in (3.6), it will be assumed that it is determined by momentum conservation from $\boldsymbol{q}$ and $\boldsymbol{q}'$—specifically, $\boldsymbol{q}''=\boldsymbol{q}+\boldsymbol{q}'+\boldsymbol{G}$ for the first term and $\boldsymbol{q}''=\boldsymbol{q}-\boldsymbol{q}'+\boldsymbol{G}$ for the second term of (3.6).

Up until expression (3.6) the phonon state has been specified by the $\boldsymbol{q}s$ notation to make the functional dependence explicit. However, the scattering operator can be represented much more compactly by using a single variable $\lambda=\boldsymbol{q}s$ or $-\lambda=(-\boldsymbol{q}s)$ to represent the wavevector and polarization.

$$\begin{aligned}\left[\frac{\partial n_\lambda}{\partial t}\right]_{\text{3-ph}} &= \frac{A_{\rm uc}}{2\pi\hbar^2}\sum_{s',s''}\int \mathrm{d}^2\boldsymbol{q}'|\tilde{\mathcal{V}}_3(-\lambda,-\lambda',\lambda'')|^2\delta(-\omega_\lambda-\omega_{\lambda'}+\omega_{\lambda''})\\ &\times\big((n_\lambda+1)(n_{\lambda'}+1)n_{\lambda''}-n_\lambda n_{\lambda'}(n_{\lambda''}+1)\big)\\ &+\frac{A_{\rm uc}}{4\pi\hbar^2}\sum_{s',s''}\int \mathrm{d}^2\boldsymbol{q}'|\tilde{\mathcal{V}}_3(-\lambda,\lambda',\lambda'')|^2\delta(-\omega_\lambda+\omega_{\lambda'}+\omega_{\lambda''})\\ &\times\big((n_\lambda+1)n_{\lambda'}n_{\lambda''}-n_\lambda(n_{\lambda'}+1)(n_{\lambda''}+1)\big).\end{aligned} \tag{3.7}$$

When convenient the phonon state $\lambda$ will appear as a subscript, but it still represents $\boldsymbol{q}s$, the combination of a continuous variable, $\boldsymbol{q}$, for wavevector and a discrete one $s$ for the polarization.

### 3.1.1 Weak form of phonon scattering operator

While expression (3.7) is a relatively standard representation of the three phonon scattering operator [89, 115], it splits phonon scattering events into two types based on a rather arbitrary viewpoint—specifically the viewpoint of an observer in one of the phonon states. The symmetry of three phonon processes, is more faithfully represented by the "weak" form of the scattering operator. To the author's knowledge the weak form of this operator has not been reported elsewhere, so a brief derivation follows.

The weak form of the scattering operator is derived by introducing a delta function $\delta_{\lambda,\tilde{\lambda}} = \frac{A_{\text{uc}}}{4\pi^2}\delta_{s,\tilde{s}}\delta(\boldsymbol{q}-\tilde{\boldsymbol{q}})$, which is a combination of a Kronecker delta for the discrete polarization variable and a Dirac delta for the wavevector variable. Integration over $\boldsymbol{q}$ is also accompanied by summation over $s$. In the following expressions the integration over $\boldsymbol{q}''$ which was eliminated by momentum conservation will also be written explicitly

$$\begin{aligned}
\sum_s \int \mathrm{d}^2\boldsymbol{q}\,\delta_{\lambda,\tilde{\lambda}}\left[\frac{\partial n_\lambda}{\partial t}\right]_{\text{3-ph}} \;=\; & \frac{A_{\text{uc}}^2}{8\pi^3\hbar^2}\sum_{s,s',s''}\int \mathrm{d}^2\boldsymbol{q}\int \mathrm{d}^2\boldsymbol{q}'\int \mathrm{d}^2\boldsymbol{q}''\,\delta_{\lambda,\tilde{\lambda}}|\tilde{V}_3(-\lambda,-\lambda',\lambda'')|^2 \\
& \times\delta(\boldsymbol{q}+\boldsymbol{q}'-\boldsymbol{q}''+\boldsymbol{G})\delta(-\omega_\lambda-\omega_{\lambda'}+\omega_{\lambda''}) \\
& \times\big((n_\lambda+1)(n_{\lambda'}+1)n_{\lambda''}-n_\lambda n_{\lambda'}(n_{\lambda''}+1)\big) \\
& +\frac{A_{\text{uc}}^2}{16\pi^3\hbar^2}\sum_{s,s',s''}\int \mathrm{d}^2\boldsymbol{q}\int \mathrm{d}^2\boldsymbol{q}'\int \mathrm{d}^2\boldsymbol{q}''\,\delta_{\lambda,\tilde{\lambda}}|\tilde{V}_3(-\lambda,\lambda',\lambda'')|^2 \\
& \times\delta(-\boldsymbol{q}+\boldsymbol{q}'+\boldsymbol{q}''+\boldsymbol{G})\delta(-\omega_\lambda+\omega_{\lambda'}+\omega_{\lambda''}) \\
& \times\big((n_\lambda+1)n_{\lambda'}n_{\lambda''}-n_\lambda(n_{\lambda'}+1)(n_{\lambda''}+1)\big). \qquad (3.8)
\end{aligned}$$

A change of variables in the second term, $\lambda\to\lambda''$ and $\lambda''\to\lambda$, makes the distribution

functions of the second term match, up to a minus sign, with the first term

$$\begin{aligned}\left[\frac{\partial n_{\tilde{\lambda}}}{\partial t}\right]_{\text{3-ph}} &= \frac{A_{\text{uc}}^2}{8\pi^3\hbar^2}\sum_{s,s',s''}\int \mathrm{d}^2\boldsymbol{q}\int \mathrm{d}^2\boldsymbol{q}'\int \mathrm{d}^2\boldsymbol{q}''\delta_{\lambda,\tilde{\lambda}}|\tilde{\mathcal{V}}_3(-\lambda,-\lambda',\lambda'')|^2\\ &\times\delta(\boldsymbol{q}+\boldsymbol{q}'-\boldsymbol{q}''+\boldsymbol{G})\delta(-\omega_\lambda-\omega_{\lambda'}+\omega_{\lambda''})\\ &\times\big((n_\lambda+1)(n_{\lambda'}+1)n_{\lambda''}-n_\lambda n_{\lambda'}(n_{\lambda''}+1)\big)\\ &+\frac{A_{\text{uc}}^2}{16\pi^3\hbar^2}\sum_{s,s',s''}\int \mathrm{d}^2\boldsymbol{q}\int \mathrm{d}^2\boldsymbol{q}'\int \mathrm{d}^2\boldsymbol{q}''\delta_{\lambda'',\tilde{\lambda}}|\tilde{\mathcal{V}}_3(-\lambda'',\lambda',\lambda)|^2\\ &\times\delta(-\boldsymbol{q}''+\boldsymbol{q}'+\boldsymbol{q}+\boldsymbol{G})\delta(-\omega_{\lambda''}+\omega_{\lambda'}+\omega_\lambda)\\ &\times\big((n_{\lambda''}+1)n_{\lambda'}n_\lambda-n_{\lambda''}(n_{\lambda'}+1)(n_\lambda+1)\big).\end{aligned}\tag{3.9}$$

The function $|\tilde{\mathcal{V}}_3|$ is symmetric with regards to its arguments as well as multiplying all arguments by $-1$, so the first and second term can be combined into

$$\begin{aligned}\left[\frac{\partial n_{\tilde{\lambda}}}{\partial t}\right]_{\text{3-ph}} &= \frac{A_{\text{uc}}^2}{16\pi^3\hbar^2}\sum_{s,s',s''}\int \mathrm{d}^2\boldsymbol{q}\int \mathrm{d}^2\boldsymbol{q}'\int \mathrm{d}^2\boldsymbol{q}''|\tilde{\mathcal{V}}_3(-\lambda,-\lambda',\lambda'')|^2\\ &\times(2\delta_{\lambda,\tilde{\lambda}}-\delta_{\lambda'',\tilde{\lambda}})\delta(\boldsymbol{q}+\boldsymbol{q}'-\boldsymbol{q}''+\boldsymbol{G})\delta(-\omega_\lambda-\omega_{\lambda'}+\omega_{\lambda''})\\ &\times\big((n_\lambda+1)(n_{\lambda'}+1)n_{\lambda''}-n_\lambda n_{\lambda'}(n_{\lambda''}+1)\big).\end{aligned}\tag{3.10}$$

Again exploiting a change of variables and symmetry, this can be further aligned with the physical process (combination of two phonons into a third or vice versa)

$$\begin{aligned}\left[\frac{\partial n_{\tilde{\lambda}}}{\partial t}\right]_{\text{3-ph}} &= \frac{A_{\text{uc}}^2}{16\pi^3\hbar^2}\sum_{s,s',s''}\int \mathrm{d}^2\boldsymbol{q}\int \mathrm{d}^2\boldsymbol{q}'\int \mathrm{d}^2\boldsymbol{q}''|\tilde{\mathcal{V}}_3(-\lambda,-\lambda',\lambda'')|^2\\ &\times(\delta_{\lambda,\tilde{\lambda}}+\delta_{\lambda',\tilde{\lambda}}-\delta_{\lambda'',\tilde{\lambda}})\delta(\boldsymbol{q}+\boldsymbol{q}'-\boldsymbol{q}''+\boldsymbol{G})\delta(-\omega_\lambda-\omega_{\lambda'}+\omega_{\lambda''})\\ &\times\big((n_\lambda+1)(n_{\lambda'}+1)n_{\lambda''}-n_\lambda n_{\lambda'}(n_{\lambda''}+1)\big).\end{aligned}\tag{3.11}$$

Apart from being a more compact notation, (3.11) makes immediately apparent the symmetry that exists between coupled states in a three phonon process,

$$\left[\frac{\partial n_\lambda}{\partial t}\right]_{\text{3-ph}}=\left[\frac{\partial n_{\lambda'}}{\partial t}\right]_{\text{3-ph}}=-\left[\frac{\partial n_{\lambda''}}{\partial t}\right]_{\text{3-ph}},\tag{3.12}$$

for states chosen such that $\omega_\lambda+\omega_{\lambda'}=\omega_{\lambda''}$.

### 3.1.2 Energy and momentum conservation

Using (3.11) it is easy to see that energy should be invariant during the scattering as a consequence of the delta function in terms of energy:

$$\begin{aligned}\sum_s \int \mathrm{d}^2\boldsymbol{q}\omega_\lambda \left[\frac{\partial n_\lambda}{\partial t}\right]_{3\text{-ph}} &= 0 \\ &= \frac{A_{\mathrm{uc}}}{4\pi\hbar^2}\sum_{s,s',s''}\int \mathrm{d}^2\boldsymbol{q}\int \mathrm{d}^2\boldsymbol{q}'\int \mathrm{d}^2\boldsymbol{q}''\underbrace{(\omega_\lambda+\omega_{\lambda'}-\omega_{\lambda''})}_{=0} \\ &\quad\times|\tilde{V}_3(-\lambda,-\lambda',\lambda'')|^2\delta(-\omega_\lambda-\omega_{\lambda'}+\omega_{\lambda''}) \\ &\quad\times\big((n_\lambda+1)(n_{\lambda'}+1)n_{\lambda''}-n_\lambda n_{\lambda'}(n_{\lambda''}+1)\big). \qquad (3.13)\end{aligned}$$

The condition for momentum conservation in normal processes ($\boldsymbol{G}=0$) also directly follows.

$$\begin{aligned}\sum_s \int \mathrm{d}^2\boldsymbol{q}\,\boldsymbol{q}\left[\frac{\partial n_\lambda}{\partial t}\right]_{3\text{-ph}} &= 0 \\ &= \frac{A_{\mathrm{uc}}}{4\pi\hbar^2}\sum_{s,s',s''}\int \mathrm{d}^2\boldsymbol{q}\int \mathrm{d}^2\boldsymbol{q}'\int \mathrm{d}^2\boldsymbol{q}''\underbrace{(\boldsymbol{q}+\boldsymbol{q}'-\boldsymbol{q}'')}_{=0} \\ &\quad\times|\tilde{V}_3(-\lambda,-\lambda',\lambda'')|^2\delta(-\omega_\lambda-\omega_{\lambda'}+\omega_{\lambda''}) \\ &\quad\times\big((n_\lambda+1)(n_{\lambda'}+1)n_{\lambda''}-n_\lambda n_{\lambda'}(n_{\lambda''}+1)\big). \qquad (3.14)\end{aligned}$$

In order to derive the weak form it was necessary to exploit the symmetry of the $|\tilde{V}_3|$ term. Specifically, the $|\tilde{V}_3|$ term is invariant under any permutation of the arguments or change of sign of all three wavevectors–which is clear mathematically from the form of (2.29) and the Maxwell relations applied to (2.16). It follows that if $|\tilde{V}_3|$ does not have the proper symmetry, energy and momentum conservation will not be satisfied.

The connection between symmetry and conservation is important, because numerical calculation of the third order force constants make use of a third order derivatives and is hence prone to numerical errors. While the force constants used in this work reproduce previous calculations of the Grüneisen parameter (see Figure 2-8 and ref-

erence [81]), and will be shown to yield reasonable values for thermal conductivity, they do not satisfy these symmetries. Discussion of the consequences of this lack of symmetry and methods to ameliorate the situation within the context of the thermal transport simulation will appear in Section 5.3.

### 3.1.3 Linearized scattering operator

It is common to linearize the scattering operator using an expansion of the distribution function $n_\lambda = n_\lambda^0 + n_\lambda^1 + \ldots$ which is then truncating after the first order term [115, 124]. The zero-th order term is the equilibrium distribution, a Bose-Einstein distribution at the temperature $T_0$,

$$n_\lambda^0 = n^{\text{eq}}(\omega_\lambda; T_0) = \frac{1}{\exp\left(\frac{\hbar\omega_\lambda}{k_B T_0}\right) - 1}. \tag{3.15}$$

To linearize (3.7), terms higher than order 1 in $n_\lambda^1$ are also discarded (e.g. $n_\lambda^1 n_{\lambda'}^1$).

Instead of expanding the distribution and truncating to first order, this work employs an analytical decomposition of the distribution into a spatially variable equilibrium part and a non-equilibrium part [102, 91, 93]

$$n_\lambda(\boldsymbol{x}, t) = n^{\text{eq}}(\omega_\lambda; T(\boldsymbol{x})) + n_\lambda^{\text{d}}(\boldsymbol{x}, t). \tag{3.16}$$

We will frequently evaluate the simulation at a location $\boldsymbol{x}$ at the reference temperature $T(\boldsymbol{x}) = T_0$, so that the decomposition is simplified to $n_\lambda = n_\lambda^0 + n_\lambda^{\text{d}}$. This decomposition was introduced for low variance deviational simulation Monte Carlo (LVDSMC) simulations of the Boltzmann transport equation for rarefied gases [7, 52, 51, 8]. This decomposition allows the scattering operator to be written exactly in terms of deviations from equilibrium and to analytically remove the equilibrium contribution, resulting in dramatic reduction in stochastic noise.

In the context of the three phonon scattering operator, the analytical decomposi-

tion leads to linearization in terms of deviations from equilibrium by taking $n_\lambda^{\mathrm{d}} \ll n_\lambda^0$

$$\begin{aligned}\left[\frac{\partial n_\lambda}{\partial t}\right]_{\text{3-ph}} &= \frac{A_{\mathrm{uc}}}{2\pi\hbar^2}\sum_{s',s''}\int \mathrm{d}^2\boldsymbol{q}'|\tilde{\mathcal{V}}_3(-\lambda,-\lambda',\lambda'')|^2\delta(-\omega_\lambda-\omega_{\lambda'}+\omega_{\lambda''})\\ &\times\big((n^0_{\lambda''}-n^0_{\lambda'})n^{\mathrm{d}}_\lambda+(n^0_{\lambda''}-n^0_\lambda)n^{\mathrm{d}}_{\lambda'}+(n^0_\lambda+n^0_{\lambda'}+1)n^{\mathrm{d}}_{\lambda''}\big)\\ &+\frac{A_{\mathrm{uc}}}{4\pi\hbar^2}\sum_{s',s''}\int \mathrm{d}^2\boldsymbol{q}'|\tilde{\mathcal{V}}_3(-\lambda,\lambda',\lambda'')|^2\delta(-\omega_\lambda+\omega_{\lambda'}+\omega_{\lambda''})\\ &\times\big(-(n^0_{\lambda''}+n^0_{\lambda'}+1)n^{\mathrm{d}}_\lambda+(n^0_{\lambda''}-n^0_\lambda)n^{\mathrm{d}}_{\lambda'}+(n^0_{\lambda'}-n^0_\lambda)n^{\mathrm{d}}_{\lambda''}\big).\end{aligned} \tag{3.17}$$

This is equivalent to the iterative solution derivation [87, 77]. Here we note that decomposition (3.16) can also be used to obtain the deviational form valid for arbitrary deviations from equilibrium (if the assumption $n_\lambda^{\mathrm{d}} \ll n_\lambda^0$ is not made). Although not the subject of this thesis, such form would be useful for extending the present work to problems exhibiting large deviations from equilibrium. An example of non-linear deviational methods can be found in [46].

## 3.2 Deviational Boltzmann

The goal of the analytical decomposition is to divide the problem into two parts: an equilibrium part that can be solved analytically and a non-equilibrium part for which the dynamics must be simulated.

The scattering operator of (3.7) can be directly used to govern the deviational distributions because scattering has no effect on the equilibrium distribution, hence

$$\left[\frac{\partial n_\lambda}{\partial t}\right]_{\text{3-ph}} = \left[\frac{\partial n^{\mathrm{d}}_\lambda}{\partial t}\right]_{\text{3-ph}}. \tag{3.18}$$

The left-hand side of the Boltzmann equation for deviations is also obtained by exploiting the time-invariant nature of the equilibrium solution. Allowing for a spatially

variable reference equilibrium distribution, Equation (3.1) can be rewritten as [93]

$$\frac{\partial n^{\mathrm{d}}(\boldsymbol{q}s)}{\partial t} + \boldsymbol{v}(\boldsymbol{q}s)\cdot\nabla_{\boldsymbol{x}} n^{\mathrm{d}}(\boldsymbol{q}s) + \boldsymbol{v}(\boldsymbol{q}s)\cdot\nabla_{\boldsymbol{x}} n^{\mathrm{eq}}(\omega(\boldsymbol{q}s);T(\boldsymbol{x})) = \left[\frac{\partial n^{\mathrm{d}}(\boldsymbol{q}s)}{\partial t}\right]_{\mathrm{scatt}}. \quad (3.19)$$

The state of the art simulations solve the Boltzmann equation for steady-state ($\frac{\partial n^{\mathrm{d}}(\boldsymbol{q}s)}{\partial t} = 0$), spatially homogeneous ($\nabla_{\boldsymbol{x}} n^{\mathrm{d}}(\boldsymbol{q}s) = 0$) problems, formally corresponding to the equation

$$\boldsymbol{v}(\boldsymbol{q}s)\cdot\nabla_{\boldsymbol{x}} T(\boldsymbol{x})\left.\frac{\partial n^{\mathrm{eq}}(\omega(\boldsymbol{q}s);T)}{\partial T}\right|_{T_0} = \left[\frac{\partial n^{\mathrm{d}}(\boldsymbol{q}s)}{\partial t}\right]_{\mathrm{scatt}} \quad (3.20)$$

This equation represents a balance between scattering events and advection due to a spatially uniform, temporally steady (weak) temperature gradient. This work will subsequently show how transient and the full spatially dependent effects can be retained.

We note here that the deviational formulation is not necessarily equivalent to linearization, since at the level of Equations (3.18) and (3.19), no terms have been linearized. Nonlinear-deviational Monte Carlo formulations have been developed [46]. In this work, however, and because only small deviations from equilibrium are of interest, linearization of the scattering operator (see Section 3.1.3) will be used both for the iterative method described in Chapter 4 and the Monte Carlo method of Chapter 6. It is important to note that small deviation from equilibrium ($\Delta T/T_0 \ll 1$, where $\Delta T$ is the characteristic temperature difference and $T_0$ the reference temperature, *does not* imply near continuum behavior ($Kn = \Lambda/L \ll 1$, where $\Lambda$ is the mean free path and $L$ is the system length scale—see Section 3.5.1) as should be clear from the unrelated non dimensional regimes each definition requires. For a more complete discussion, see Ref [93].

## 3.3 System properties

When the distribution function is known, all relevant properties of the system can be recovered through its moments. For convenience real space and reciprocal space will be considered continuous in this section. The number density of phonons in the

system is given by

$$n_{\rm ph}(\boldsymbol{x},t) = \frac{1}{4\pi^2\delta}\sum_s \int \mathrm{d}^2\boldsymbol{q}\, n(\boldsymbol{q}s,\boldsymbol{x},t). \tag{3.21}$$

The energy density in the system is

$$u(\boldsymbol{x},t) \;=\; \frac{1}{4\pi^2\delta}\sum_s \int \mathrm{d}^2\boldsymbol{q}\,\hbar\omega(\boldsymbol{q}s)n(\boldsymbol{q}s,\boldsymbol{x},t). \tag{3.22}$$

The heat flux is

$$\boldsymbol{J}_E(\boldsymbol{x},t) \;=\; \frac{1}{4\pi^2\delta}\sum_s \int \mathrm{d}^2\boldsymbol{q}\,\boldsymbol{v}(\boldsymbol{q}s)\hbar\omega(\boldsymbol{q}s)n(\boldsymbol{q}s,\boldsymbol{x},t), \tag{3.23}$$

where the spatial and time dependence of the distribution function have been made explicit, and the system has a nominal thickness $\delta$.

## 3.4 Thermal conductivity in devices

Of primary importance to this work is the question of a material's (and a device's) ability to transport thermal energy. Assuming diffusive (continuum) behavior [44], Fourier's law of heat conduction describes the response to a temperature gradient using the thermal conductivity tensor $\boldsymbol{\kappa}$,

$$\boldsymbol{J}_E = -\boldsymbol{\kappa}\nabla_{\boldsymbol{x}}T. \tag{3.24}$$

or element-wise

$$\kappa_{\alpha\beta} = -\frac{J_{\alpha,E}}{[\nabla_{\boldsymbol{x}}T]_\beta}. \tag{3.25}$$

It should be emphasized that (3.24) is a continuum constitutive relation and is not necessarily valid for thermal transport in micro scale devices where kinetic effects may be important [93], but it is always possible to define an effective thermal conductivity for a temperature difference $\Delta T$ applied across a length $L$. For simplicity, and without loss of generality, this study will be confined to 1-d temperature gradients that align with one of the cartesian axes. Given a temperature gradient $\Delta T_x/L_x$ in the $x$

direction the effective thermal conductivity is

$$\kappa_{xx,\text{eff}} = -\frac{J_{x,E}L_x}{\Delta T_x} \tag{3.26}$$

$$\kappa_{yx,\text{eff}} = -\frac{J_{y,E}L_x}{\Delta T_x}. \tag{3.27}$$

Similarly, with a gradient in the $y$ direction, the effective thermal conductivity is

$$\kappa_{yy,\text{eff}} = -\frac{J_{y,E}L_y}{\Delta T_y} \tag{3.28}$$

$$\kappa_{xy,\text{eff}} = -\frac{J_{x,E}L_y}{\Delta T_y}. \tag{3.29}$$

which are *device* and not material properties. In this work, the Γ-M direction of the reciprocal space will be aligned with the $x$-direction, and the Γ−K' direction will be aligned with the $y$ direction.

## 3.5 Scattering rates

A simple measure of the anharmonic effects on a phonon distribution is the phonon lifetime. Under the single mode relaxation time (SMRT) approximation, this lifetime is straightforward to calculate. The SMRT approximation is that the phonon distribution decays exponentially towards the local equilibrium value independent of any other mode occupations

$$\left[\frac{\partial n_\lambda}{\partial t}\right]_{\text{scatt}} = \frac{n_\lambda^0 - n_\lambda}{\tau_\lambda} = \frac{-n_\lambda^{\text{d}}}{\tau_\lambda}. \tag{3.30}$$

Under this assumption, the scattering rate can be obtained as [57, 124, 115]

$$\Gamma_\lambda = \frac{1}{\tau_\lambda} = -\frac{1}{n_\lambda^{\text{d}}}\left[\frac{\partial n_\lambda^{\text{d}}}{\partial t}\right]_{\text{scatt}}. \tag{3.31}$$

This can be readily evaluated from (3.7) by setting $n^{\mathrm{d}}_{\lambda'} = n^{\mathrm{d}}_{\lambda''} = 0$ (in words, allowing only a single mode to be out of equilibrium), yielding

$$\begin{aligned}\Gamma_\lambda &= \frac{A_{\mathrm{uc}}}{2\pi\hbar^2}\sum_{s',s''}\int \mathrm{d}^2q'|\tilde{\mathcal{V}}_3(-\lambda,-\lambda',\lambda'')|^2\delta(-\omega_\lambda-\omega_{\lambda'}+\omega_{\lambda''}) \\ &\quad\times(n^0_{\lambda'}-n^0_{\lambda''}) \\ &\quad+\frac{A_{\mathrm{uc}}}{4\pi\hbar^2}\sum_{s',s''}\int \mathrm{d}^2q'|\tilde{\mathcal{V}}_3(-\lambda,\lambda',\lambda'')|^2\delta(-\omega_\lambda+\omega_{\lambda'}+\omega_{\lambda''}) \\ &\quad\times(n^0_{\lambda'}+n^0_{\lambda''}+1). \end{aligned} \tag{3.32}$$

Note that for scattering pathways where $\lambda = \lambda'$ or $\lambda' = \lambda''$ in (3.32) this rate is too small by a factor of 2, for type I and type II processes respectively. Those cases may be important when branch dispersions are linear, but significant regions of linearity do not occur in practice based on the present force constants.

This same expression for the phonon lifetime can be derived from the anharmonic phonon self energy by neglecting the effect of the anharmonic terms on the phonon dispersion relation—a quasi harmonic approximation, which is typically a reasonable approximation [33, 31, 72, 115] and consistent with the treatment of the dispersion relation in this work. The scattering rate calculated in this manner does not consider the effect of coupling between out of equilibrium modes, but for lack of a better measure, Equation (3.32) will be used to approximate the phonon lifetimes consistent with the recent literature [79, 33, 40].

### 3.5.1 Knudsen number

In many systems with simple geometry and under the SMRT approximation, the effective thermal conductivity (modified due to the structure) can be calculated as an additional function of the Knudsen number alone (the ratio of the mean free path to the characteristic length scale of the device) [23, 36, 32, 121]. We will show this to be the case for the effective thermal conductivity in graphene ribbons in Section 6.7.2 and Chapter 7 (see also Ref. [67]).

In the present work, which is expected to extend beyond the simple geometries

and assumptions that facilitate analytical solution, the Knudsen number will be used as a measure of the strength of kinetic effects. In order to provide a simple measure for kinetic effects that is consistent with the formulation for rarefied gas dynamics [119], the following mean free path definition will be used

$$\Lambda(T) = \frac{\int \mathrm{d}^2\boldsymbol{q} \sum_s ||\boldsymbol{v}(\boldsymbol{q}s)||\tau(\boldsymbol{q}s)n^{\mathrm{eq}}(\omega(\boldsymbol{q}s);T))}{\int \mathrm{d}^2\boldsymbol{q} \sum_s n^{\mathrm{eq}}(\omega(\boldsymbol{q}s);T)} \tag{3.33}$$

to evaluate the Knudsen number

$$Kn = \frac{\Lambda}{L_{\mathrm{c}}}, \tag{3.34}$$

where $L_{\mathrm{c}}$ is the characteristic length scale of the device and $\tau(\boldsymbol{q}s)$ is the mode lifetime given by

$$\Gamma(\boldsymbol{q}s) = \frac{1}{\tau(\boldsymbol{q}s)} = -\frac{1}{n^{\mathrm{d}}(\boldsymbol{q}s)}\left[\frac{\partial n^{\mathrm{d}}(\boldsymbol{q}s)}{\partial t}\right]_{\mathrm{scatt}}. \tag{3.35}$$

Equation (3.33) is the average distance any phonon travels between scattering events calculated at equilibrium. This follows standard practice in kinetic theory [114] and is consistent with the fact that the mean free path is a reference quantity. In the problems of interest here, the deviation from equilibrium is small providing additional justification for neglecting non-equilibrium effects.

Definition (3.33) results in a dramatic simplification compared to the mode dependent mean free path $\boldsymbol{\Lambda}(\boldsymbol{q}s)$ discussed elsewhere [33, 79, 123], while still allowing for comparison of kinetic effects in more traditional systems [24] and aiding in the system level understanding. For example, one traditionally expects [119] three transport regimes: 1)The continuum regime ($Kn \lesssim 0.1$) where kinetic effects are minor and transport is generally diffusive [44], 2) the transition regime ($0.1 \lesssim Kn \lesssim 10$) where diffusive and ballistic transport are important, and 3) the collisionless regime ($10 \lesssim Kn$) where transport is almost entirely ballistic. In the first regime, transport can be represented with the diffusive models (e.g. Navies-Stokes for rarefied gases and Fourier's Law for phonon transport). In the collisionless regime, radiative transfer methods provide the most efficient solutions. In the transition regime, solution of the Boltzmann equation is typically required. In Chapter 7, we will discuss these regimes

in the context of thermal transport in graphene.

# Chapter 4

# Solution of the homogeneous Boltzmann equation using an iterative method

Direct or stochastic integration of the linearized Boltzmann equation (3.19) with the three phonon scattering term (3.7) has, to date, defied numerical solution for general problems other than spatially homogeneous, steady state, linearized problems. The later can be solved using an iterative solution [87, 88, 77] which can be derived from (3.17) and (3.20) by grouping $n_\lambda^{\mathrm{d}}$ terms onto the left-hand side

$$\begin{aligned} n_\lambda^{\mathrm{d}} \;=\; & -\frac{\boldsymbol{v}_\lambda \cdot \nabla_{\boldsymbol{x}} T(\boldsymbol{x})}{\Gamma_\lambda} \frac{\partial n^{\mathrm{eq}}(\omega_\lambda, T)}{\partial T}\bigg|_{T_0} \\ & + \frac{A_{\mathrm{uc}}}{\Gamma_\lambda 2\pi\hbar^2} \sum_{s',s''} \int \mathrm{d}^2\boldsymbol{q}' |\tilde{\mathcal{V}}_3(-\lambda, -\lambda', \lambda'')|^2 \delta(-\omega_\lambda - \omega_{\lambda'} + \omega_{\lambda''}) \\ & \times \Big( (n^0_{\lambda''} - n^0_\lambda) n^{\mathrm{d}}_{\lambda'} + (n^0_\lambda + n^0_{\lambda'} + 1) n^{\mathrm{d}}_{\lambda''} \Big) \\ & + \frac{A_{\mathrm{uc}}}{\Gamma_\lambda 4\pi\hbar^2} \sum_{s',s''} \int \mathrm{d}^2\boldsymbol{q}' |\tilde{\mathcal{V}}_3(-\lambda, \lambda', \lambda'')|^2 \delta(-\omega_\lambda + \omega_{\lambda'} + \omega_{\lambda''}) \\ & \times \Big( (n^0_{\lambda''} - n^0_\lambda) n^{\mathrm{d}}_{\lambda'} + (n^0_{\lambda'} - n^0_\lambda) n^{\mathrm{d}}_{\lambda''} \Big), \end{aligned} \tag{4.1}$$

which can be iteratively used to obtain new estimates of $n_\lambda^{\mathrm{d}}$ based on previous iteration values (of $n_\lambda^{\mathrm{d}'}$, $n_\lambda^{\mathrm{d}''}$, etc). This is repeated until convergence is obtained. The first term

on the right-hand side of (4.1) is a constant that does not include coupling between out of equilibrium modes. Thus by analogy, this corresponds to the solution of the single mode relaxation time approximation problem

$$n_{\lambda}^{\mathrm{d,SMRT}} = \frac{\boldsymbol{v}_{\lambda} \cdot \nabla_{\boldsymbol{x}} T(\boldsymbol{x})}{\Gamma_{\lambda}} \left. \frac{\partial n^{\mathrm{eq}}(\lambda, T)}{\partial T} \right|_{T_0} \tag{4.2}$$

Numerical integration of the distribution function by iteration of (4.1) or even the single mode relaxation time solution (4.2) remains challenging for two primary reasons: 1) The third order force constants are expensive to calculate and 2) the integral of the scattering operator contains delta functions enforcing energy and momentum conservation.

For the present work, the first point is addressed by using density functional perturbation theory (DFPT) to calculate the force constants of graphene, which are then used in (2.25). Both the second and third order force constants have been calculated using the local density approximation (LDA) with the Perdew-Zunger parameterization [94] and provided by Sangyeop Lee, using code developed by himself and Keivan Esfarjani [33]. We are deeply grateful to both.

The second issue, numerical integration of the delta function, is fairly common in solid state physics [115, 77] and other fields [122]. For example, a similar integration of a delta function occurs in the immersed boundary method where it is referred to as regularization of the delta function—that is, calculating the contribution of a delta function using a regular computational grid.

This chapter describes in detail an interpolation based quadrature which allows for regularization of the delta function without introducing a smearing parameter which would further complicate convergence studies. It also is an opportunity to present the reciprocal space discretization scheme that will be used throughout this thesis, thus laying the foundation for the Monte Carlo method to be developed in subsequent chapters.

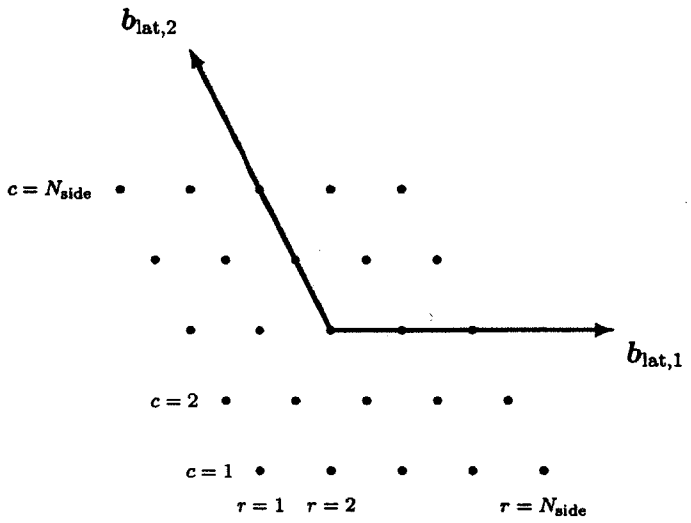


Figure 4-1: Sketch of reciprocal space discretization with $N_{side} = 5$. By adding a reciprocal lattice vector, the top most and right most grid points are equivalent to the bottom most and left most, respectively.

## 4.1 Discretization of reciprocal space

The parallelepiped unit cell of Figure 2-2 will be used to represent reciprocal space. The reciprocal space grid points are chosen as fractions of the reciprocal lattice basis vectors as follows

$$\boldsymbol{q}_{r,c} = \begin{cases} \frac{(r-1)\boldsymbol{b}_{lat,1}}{(N_{side}-1)} + \frac{(c-1)\boldsymbol{b}_{lat,2}}{(N_{side}-1)} - \frac{\boldsymbol{b}_{lat,1}+\boldsymbol{b}_{lat,2}}{2} & N_{side} \text{ is odd} \\ \frac{(r-0.5)\boldsymbol{b}_{lat,1}}{(N_{side}-1)} + \frac{(c-0.5)\boldsymbol{b}_{lat,2}}{(N_{side}-1)} - \frac{\boldsymbol{b}_{lat,1}+\boldsymbol{b}_{lat,2}}{2} & N_{side} \text{ is even} \end{cases} \tag{4.3}$$

where $N_{side}$ is the number of grid points along each side of the unit cell as shown in Figure 4-1 and $r, c \in \{1, 2, .., N_{side}\}$. The odd and even cases have different offsets so that both include the gamma point of the Brillouin zone, which means that the sum of the wavevectors of any two grid points (plus the appropriate reciprocal lattice vector) always falls on another grid point—allowing momentum conservation to be satisfied exactly on the grid.

Points along the boundary of the unit cell are symmetrically equivalent to those grid points on the opposite edge of the unit cell. Hence, the number of unique points is

$N_{\text{pts}} = (N_{\text{side}} - 1)^2$. At each reciprocal space grid point, there will exist 6 polarization. For convenience, six copies of the discretized Brillouin zone will be used, so that each grid point $j$ identifies a unique combination of wavevector and polarization $\boldsymbol{q}_j s_j$ with a total number of grid points (or states) $N_{\text{states}} = 6N_{\text{pts}}$.

## 4.2 System properties

The easiest integrals to evaluate in this work are the moments of the distribution function for the system properties (3.21)-(3.23). While it would not be unreasonable to simply present a standard quadrature for these integrals, in order to prepare for subsequent need to integrate delta functions in reciprocal space, consider the following derivation of a quadrature scheme based on linear interpolation.

Given the discretization of reciprocal space of Section 4.1, the unit cell can be tessellated with $N_{\text{tri}}$ equal area triangles. The wavevector at the $n$th vertex of the $m$th triangle is denoted by $\boldsymbol{q}^{\text{v}}_{m,n}$—see Figure 4-2. The integral of the form of (3.21)-(3.23) of an unspecified function $f(\boldsymbol{q}s)$ over a single unit cell

$$I = \frac{1}{4\pi^2\delta} \sum_s \int_{\text{Unit cell}} \mathrm{d}^2\boldsymbol{q} f(\boldsymbol{q}s) \tag{4.4}$$

can be written as a sum of the integrals over the $m$th triangle for $m$ from 1 to $N_{\text{tri}}$

$$I = \frac{1}{4\pi^2\delta} \sum_s \sum_{m=1}^{N_{\text{tri}}} \int_{m\text{th triangle}} \mathrm{d}^2\boldsymbol{q} f(\boldsymbol{q}s). \tag{4.5}$$

Assuming that the integrand is linear inside each triangle, the integral over the $m$th triangle is the average of the three corner values times the area of the triangle ($S_{\text{tri}} = \frac{4\pi^2}{A_{\text{uc}} N_{\text{tri}}}$, see (2.7)):

$$I = \frac{S_{\text{tri}}}{12\pi^2\delta} \sum_s \sum_{m=1}^{N_{\text{tri}}} \sum_{n=1}^{3} f(\boldsymbol{q}^{\text{v}}_{mn} s). \tag{4.6}$$

As a matter of computational efficiency this can be rewritten as a summation over the grid points and for further convenience, the index $j$ will indicate a grid point and

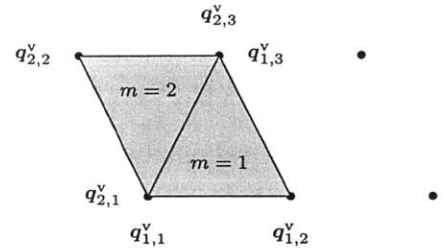


Figure 4-2: Sketch of first two triangles of the tessellation. Each grid point serves as the vertex for more than one triangle.

branch combination $\boldsymbol{q}_j s_j$

$$I = \frac{1}{A_{\text{uc}}\, N_{\text{tri}} \delta} \sum_{j=1}^{N_{\text{states}}} g_j f(\lambda_j), \tag{4.7}$$

Considering only $(N_{\text{side}} - 1)^2$ grid points by exploiting symmetry, each grid point will be a vertex of 6 different triangles and hence make 6 separate but equivalent contributions to the integral. By comparison of (4.6) and (4.7), it can be determined that, for this case, all weights are equal, $g_j = 2$. This allows evaluation of system properties as summations over the grid points, yielding, for example,

$$n_{\text{ph}}(\boldsymbol{x}, t) = \frac{2}{A_{\text{uc}}\, N_{\text{tri}} \delta} \sum_{j=1}^{N_{\text{states}}} n(\lambda_j, \boldsymbol{x}, t) \tag{4.8}$$

and

$$u(\boldsymbol{x}, t) = \frac{2}{A_{\text{uc}}\, N_{\text{tri}} \delta} \sum_{j=1}^{N_{\text{states}}} \hbar\omega_j\, n(\lambda_j, \boldsymbol{x}, t), \tag{4.9}$$

where for notational convenience $\omega_j = \omega(\lambda_j)$. Equation (4.9) also provides the method for defining the temperature, namely by finding the equilibrium distribution with parameter $T$ which has the desired energy density by inverting the relation:

$$u_{\text{eq}}(T) = \frac{2}{A_{\text{uc}}\, N_{\text{tri}} \delta} \sum_{j=1}^{N_{\text{states}}} \hbar\omega_j\, n^{\text{eq}}(\omega_j, T). \tag{4.10}$$

Also of particular interest in thermal transport calculations is the heat flux

$$\boldsymbol{J}_E(\boldsymbol{x},t) = \frac{2}{A_{\text{uc}}\, N_{\text{tri}}\delta} \sum_{j=1}^{N_{\text{states}}} \boldsymbol{v}(\lambda_j)\hbar\omega(\lambda_j)n(\lambda_j,\boldsymbol{x},t) \tag{4.11}$$

from which the thermal conductivity is evaluated as described in Section 3.4.

## 4.3 Linear triangular (tetrahedron) method

In his recent review of ab initio thermal transport [77], Mingo identifies three approaches for performing the integration of the energy delta function in (4.1)

1. Explicit determination of the points (not necessarily grid points) that satisfy momentum and energy conservation, which he calls Gaussian quadrature

2. Interpolation methods that evaluate the function only on the grid points

3. Smearing of the delta function using a Gaussian function

Of these methods, the last is perhaps the easiest to implement, but it requires an additional parameter to represent the smearing, which further complicates convergence studies. Due to the uncertainty principle, it is possible that this may be a step towards physically realistic numerics, but this method requires the finest discretizations of the three [77]. In order to facilitate efficient numerics, this work employs an interpolation based method. Brief experiments with Gaussian quadrature did not appear to provide sufficient improvement to justify the added complexity. The interpolation method used here is a two dimensional version [63] of the linear tetrahedron method [42]. It is briefly described below and will be referred to as the linear triangle method.

The linear triangle method divides the Brillouin zone into $N_{\text{tri}}$ equal area triangles (see Figure 4-2); the $m$th triangle has the vertices $\boldsymbol{q}^{\text{v}}_{m,1}$, $\boldsymbol{q}^{\text{v}}_{m,2}$, $\boldsymbol{q}^{\text{v}}_{m,3}$ which belong to the set of $N^2_{\text{side}}$ grid points. The goal of the linear triangle method in this work is to approximate the integration of (3.17) and related integrals with a summation over

the grid points

$$\left[\frac{\partial n_\lambda}{\partial t}\right]_{\text{3-ph}} = \frac{A_{\text{uc}}}{2\pi\hbar^2}\sum_{j=1}^{N_{\text{states}}}\sum_{k=1}^{N_{\text{states}}} W_{\text{I}}(\lambda,j,k) \times\big((n_k^0-n_j^0)n_\lambda^{\text{d}}+(n_k^0-n_\lambda^0)n_j^{\text{d}}+(n_\lambda^0+n_j^0+1)n_k^{\text{d}}\big) + \frac{A_{\text{uc}}}{4\pi\hbar^2}\sum_{j,k} W_{\text{II}}(\lambda,j,k) \times\big(-(n_k^0+n_j^0+1)n_\lambda^{\text{d}}+(n_k^0-n_\lambda^0)n_j^{\text{d}}+(n_j^0-n_\lambda^0)n_k^{\text{d}}\big). \tag{4.12}$$

where, for convenience, the polarization and grid point indices have been combined into a single index, and a single subscript $j$ replaces the cumbersome $\lambda_j$ and likewise $\lambda_k \rightarrow k$. In this expression, $W_{\text{I}}(\lambda,j,k)$ and $W_{\text{II}}(\lambda,j,k)$ are weights that represent the regularization of the delta function times the value of the interaction element: $|\tilde{\mathcal{V}}_3(-\lambda,-\lambda_j,\lambda_k)|^2$ for type I and $|\tilde{\mathcal{V}}_3(-\lambda,\lambda_j,\lambda_k)|^2$ for type II processes. Due to momentum conservation, $W_{\text{I}}(\lambda,j,k)$ is only non-zero when $-\boldsymbol{q}-\boldsymbol{q}_j+\boldsymbol{q}_k+\boldsymbol{G}=0$ and $W_{\text{II}}(\lambda,j,k)$ is only non-zero when $\boldsymbol{q}-\boldsymbol{q}_j-\boldsymbol{q}_k+\boldsymbol{G}=0$. Thus, this expression could be rendered with a summation over branch $s''$ instead of over $k$ analogous to the difference between (3.3) and (3.7), but here the summation over $k$ is retained in the interest of clarity. Computationally efficient implementations will be further discussed in Section 4.4.

The calculation proceeds as follows: given a state $\lambda$ and the index of another state $k$ (or equivalently and much more computationally efficient only the branch $s''$ of the third state is specified and its wavevector is calculated by momentum conservation), the level set function is calculated for every point $j$ in the set of $N_{\text{states}}$ grid points and these values are stored in memory for later use.

Considering the same states $\lambda$ and $k$ (or just $s''$), the calculation then loops over every triangle $m$ in the tessellation of the reciprocal space unit cell. Each vertex of each triangle will make a contribution to the weight of the associated grid point. The values of the level set function at the vertices of the $m$th triangle are sorted so that $\varphi(\lambda,\boldsymbol{q}^{\text{v}}_{m,1}s',k) \leq \varphi(\lambda,\boldsymbol{q}^{\text{v}}_{m,2}s',k) \leq \varphi(\lambda,\boldsymbol{q}^{\text{v}}_{m,3}s',k)$. Allowing the notation $(\boldsymbol{q}^{\text{v}}_{m,n}s') = j_n$, the triangle under consideration will make contributions to the weights $W_{\text{I}}(\lambda,j_n,k)$

and $W_{\mathrm{II}}(\lambda, j_n, k)$ for $n \in \{1,2,3\}$. More specifically, the contribution at the $n$th vertex of the $m$th can be calculated from the following expressions for $\mathcal{I}_{mn}$ (see [63])

- If $0 \leq \varphi_1$, then

$$\mathcal{I}_{mn} = 0 \quad (n \in \{1,2,3\}) \tag{4.13}$$

- if $\varphi_1 < 0 \leq \varphi_2$, then

$$\mathcal{I}_{m1} = \frac{S_{\mathrm{tri}}\varphi_{21}\varphi_{31}}{-\varphi_1}(\varphi_{12} + \varphi_{13}), \tag{4.14}$$

and

$$\mathcal{I}_{mn} = \frac{S_{\mathrm{tri}}\varphi_{21}\varphi_{31}}{-\varphi_1}\varphi_{n1} \quad (n \in \{2,3\}). \tag{4.15}$$

- if $\varphi_2 < 0 \leq \varphi_3$, then

$$\mathcal{I}_{mn} = \frac{S_{\mathrm{tri}}\varphi_{13}\varphi_{23}}{\varphi_3}\varphi_{n3} \quad (n \in \{1,2\}). \tag{4.16}$$

and

$$\mathcal{I}_{m3} = \frac{S_{\mathrm{tri}}\varphi_{13}\varphi_{23}}{\varphi_3}(\varphi_{31} + \varphi_{32}) \tag{4.17}$$

- If $0 > \varphi_3$, then

$$\mathcal{I}_{mn} = 0 \quad (n \in \{1,2,3\}) \tag{4.18}$$

where the reciprocal space area of the triangle is $S_{\mathrm{tri}} = \frac{4\pi^2}{A_{\mathrm{uc}}N_{\mathrm{tri}}}$, and

$$\varphi_{pq} = \frac{-\varphi_q}{\varphi_p - \varphi_q} \quad (p, q \in \{1,2,3\}).$$

Ultimately, the weights are obtained by summing the contributions of all triangles multiplied by the appropriate interaction term

$$W_{\mathrm{I}}(\lambda, j, k) = \sum_m \sum_n \mathcal{I}_{mn} |\tilde{V}_3(-\lambda, -j_n, k)|^2 \delta_{q_j, j_n} \delta_{q+q_j-q_k, G} \tag{4.19}$$

and

$$W_{\mathrm{II}}(\lambda, j, k) = \sum_m \sum_n \mathcal{I}_{mn} |\tilde{V}_3(-\lambda, j_n, k)|^2 \delta_{q_j, j_n} \delta_{q-q_j-q_k, G} \tag{4.20}$$

where $\delta_{q_j,j_n}$ is an indicator to place the contribution of the $n$th vertex of the $m$th triangle in the array of weights at the appropriate location and the momentum conservation delta function is written explicitly here, because the weight only interpolates the energy delta function. Clearly, the weights $W(\lambda, j, k)$ are mostly zero due to the requirements of energy and momentum conservation. The following section discusses an efficient method for storing these weights and evaluation of the scattering operator integrals.

## 4.4 Efficient weight storage and integration of the Boltzmann equation

The preceding section discussed integration of the scattering operator for an arbitrary value of $\lambda$. In practice, this scattering operator must only be known for the discrete values of $\lambda$ represented by the $N_{\text{states}}$ of the computational grid. Thus, the weights can be represented by three-dimensional arrays $W_{\text{I}}(i, j, k)$ and $W_{\text{II}}(i, j, k)$ where $(i, j, k) \in \{1, .., N_{\text{states}}\}$. This three dimensional array is remarkably sparse due to the requirements of energy and momentum conservation (see Equations (4.19) and (4.20)). In particular, due to the choice of a grid for which momentum is always conserved exactly at a grid point for any combination of two grid points, the weights need be stored only for two indices $i, j$ and the polarization index for the third grid dimension $s''$.

Similarly, the sparsity due to the delta function in energy as implemented through the linear interpolation scheme (i.e. the zeros in (4.13) and (4.18)) can also be exploited to further reduce storage and computational requirements.This is achieved by only storing the non-zero values of weights along with the corresponding indices $(i, j, s'', p)$ in a table, where $p$ indicates the type of weight either I or II. Subsequently in this work, when a summation includes the weights, it will be calculated sparsely, by only summing over the non-zero weights stored in the table. This table is independent of the temperature of the simulation and can be calculated and stored once

for each discretization.

### 4.4.1 Temperature dependence and numerical integration

The temperature dependence of the scattering operator (3.17) is hidden in the equilibrium distribution functions $n_\lambda^0 = n^{\text{eq}}(\omega_\lambda; T_0)$. In preparation for a calculation either with the iterative method or the more sophisticated method presented hereafter, the temperature dependence is calculated and stored in memory as coefficients

$$C_1(i,j,k,p) = \begin{cases} W_p(i,j,k)(n_k^0 - n_j^0) & \text{if } p = \text{type I} \\ -\frac{1}{2}W_p(i,j,k)(n_k^0 + n_j^0 + 1) & \text{if } p = \text{type II} \end{cases} \tag{4.21}$$

$$C_2(i,j,k,p) = \begin{cases} W_p(i,j,k)(n_k^0 - n_i^0) & \text{if } p = \text{type I} \\ \frac{1}{2}W_p(i,j,k)(n_k^0 - n_i^0) & \text{if } p = \text{type II} \end{cases} \tag{4.22}$$

$$C_3(i,j,k,p) = \begin{cases} W_p(i,j,k)(n_i^0 + n_j^0 + 1) & \text{if } p = \text{type I} \\ \frac{1}{2}W_p(i,j,k)(n_j^0 - n_i^0) & \text{if } p = \text{type II} \end{cases} \tag{4.23}$$

In terms of these coefficients, the collision operator can be simply written as

$$\left[\frac{\partial n_i}{\partial t}\right]_{\text{3-ph}} = \frac{A_{\text{uc}}}{2\pi\hbar^2} \sum_{j,k,p} C_1(i,j,k,p) n_i^{\text{d}} + C_2(i,j,k,p) n_j^{\text{d}} + C_3(i,j,k,p) n_k^{\text{d}}, \tag{4.24}$$

the SMRT scattering rate as

$$\Gamma_i = \sum_{j,k,p} -C_1(i,j,k,p), \tag{4.25}$$

and the iterative solution as

$$\begin{aligned} n_i^{\text{d}} &= \frac{\boldsymbol{v}_\lambda \cdot \nabla_{\boldsymbol{x}} T(\boldsymbol{x})}{\Gamma_i} \left.\frac{\partial n^{\text{eq}}(\lambda, T)}{\partial T}\right|_{T_0} \\ &\quad + \frac{A_{\text{uc}}}{\Gamma_i 2\pi\hbar^2} \sum_{j,k,p} \left(C_2(i,j,k,p) n_j^{\text{d}} + C_3(i,j,k,p) n_k^{\text{d}}\right) \end{aligned} \tag{4.26}$$

Although not named or labeled as above, this formulation appears in the literature in various forms related via use of the equilibrium condition as described in Appendix A. Utilizing the equilibrium condition, the coefficients can be grouped yielding the following expressions:

$$\begin{aligned}\left[\frac{\partial n_i}{\partial t}\right]_{\text{3-ph}} &= \frac{A_{\text{uc}}}{2\pi\hbar^2}\sum_{j,k,p} C_{\text{I}}(i,j,k)\left(-\frac{n_i^{\text{d}}}{n_i^0(n_i^0+1)}-\frac{n_j^{\text{d}}}{n_j^0(n_j^0+1)}+\frac{n_k^{\text{d}}}{n_k^0(n_k^0+1)}\right)\\ &\quad+\frac{A_{\text{uc}}}{2\pi\hbar^2}\sum_{j,k,p} C_{\text{II}}(i,j,k)\left(-\frac{n_i^{\text{d}}}{n_i^0(n_i^0+1)}+\frac{n_j^{\text{d}}}{n_j^0(n_j^0+1)}+\frac{n_k^{\text{d}}}{n_k^0(n_k^0+1)}\right),\end{aligned} \tag{4.27}$$

$$\Gamma_i = \sum_{j,k,p} -\frac{C(i,j,k,p)}{n_i^0(n_i^0+1)}, \tag{4.28}$$

and

$$\begin{aligned}n_i^{\text{d}} &= \frac{\boldsymbol{v}_\lambda\cdot\nabla_{\boldsymbol{x}}T(\boldsymbol{x})}{\Gamma_i}\frac{\partial n^{\text{eq}}(\lambda,T)}{\partial T}\bigg|_{T_0}\\ &\quad+\frac{A_{\text{uc}}}{\Gamma_i 2\pi\hbar^2}\sum_{j,k,p} C(i,j,k,p)\left(\mp\frac{n_j^{\text{d}}}{n_j^0(n_j^0+1)}+\frac{n_k^{\text{d}}}{n_k^0(n_k^0+1)}\right)\end{aligned} \tag{4.29}$$

where the "$-$" applies if $p$ =I and the "$+$" applies if $p$ =II.

Numerical tests have shown that the thermal conductivity in a homogeneous problem converges with respect to discretization more rapidly when the coefficients for the type I and type II processes are symmetric—specifically when $C_{\text{I}}(i,j,k)/W_{\text{I}}(i,j,k) = C_{\text{II}}/(k,i,j)/W_{\text{II}}(k,i,j)$. In this work the following coefficients will be used

$$\begin{aligned}C_{\text{I}}(i,j,k) &= W_{\text{I}}(i,j,k)n_i^0 n_j^0(n_k^0+1)\\ C_{\text{II}}(i,j,k) &= W_{\text{II}}(i,j,k)\frac{1}{2}(n_i^0+1)n_j^0 n_k^0.\end{aligned} \tag{4.30}$$

## 4.5 Relaxation parameter

The iterative update for the distribution (4.29) in practice is a little too aggressive and often leads to numerical instabilities. This situation is easily avoided by applying

a relaxation parameter $\alpha$, such that the updated distribution is $\alpha$ times the result of (4.29) plus $1-\alpha$ times the distribution function value before the iterative expression was calculated. Numerical tests show that $\alpha = 0.5$ is a reasonable compromise between stability and efficiency.

## 4.6 Special treatment of the $\Gamma$ point

The acoustic branches at the $\Gamma$ point have zero frequency. In practice, the DFT calculations return a small negative value for $\omega^2$ which is then set to zero. Having zero frequency and zero wavevector, these phonons could in theory combine with any other phonon and exactly satisfy energy and momentum conservation. Furthermore, in the interaction term $\tilde{V}_3$, the frequency appears in the denominator, resulting in a prediction of a lifetime, $\tau$, that is also 0. Clearly the condition for existence of phonons as elementary excitations ($\omega_\lambda \tau_\lambda > 1$) is not satisfied [13]. However, care must be exercised in removing this singularity, because the largest contributions to thermal conductivity are expected to come from near the $\Gamma$ point [71]. In this work, the linear triangle method includes the $\Gamma$ point in the discretization, but grid points with frequency equal to zero are excluded from contributing to thermal transport by artificially setting $\tilde{V}_3 = 0$. This allows non-zero contributions to the scattering operator from the two other corners of a triangle whose third corner is the $\Gamma$ point. Preliminary numerical tests show that this dramatically improves the convergence in terms of discretization coarseness. After the regularization of the delta function, the $\Gamma$ point for the acoustic branches is removed from the discretization–instead of $N_{\text{states}}$ grid points, the calculation is left with $N_{\text{states}} - 3$ grid points.

## 4.7 Convergence of the iterative solution with discretization

Having specified the method of integration in the preceding sections, the convergence of (4.29) and (4.2) with discretization refinement will be presented. The convergence

Table 4.1: Convergence behavior of the iterative solution thermal conductivity with respect to discretization $N_{\text{side}}$.

| $N_{\text{side}}$ | $\kappa_{xx,\text{SMRT}}$ | $\kappa_{yy,\text{SMRT}}$ | $\kappa_{xx}$ | $\kappa_{yy}$ | CPU time per iteration (s) |
|---|---|---|---|---|---|
| 5 | 657.787 | 647.045 | 1504.26 | 1531.3 | 0.000133308 |
| 11 | 465.104 | 464.751 | 3033.04 | 2970.02 | 0.00188646 |
| 21 | 513.593 | 516.84 | 3781.03 | 3631.12 | 0.0150403 |
| 31 | 524.063 | 528.6 | 4239.37 | 3942.93 | 0.0469064 |
| 41 | 526.013 | 530.819 | 4371.41 | 4020.69 | 0.103659 |
| 51 | 527.965 | 532.793 | 4589.39 | 4138.74 | 0.204134 |
| 61 | 528.438 | 533.286 | 4735.46 | 4220.7 | 0.495263 |
| 71 | 528.912 | 533.794 | 4755.4 | 4215.91 | 0.688384 |
| 81 | 528.223 | 533.13 | 4772.39 | 4216.31 | 1.04151 |
| 91 | 528.415 | 533.281 | 4800.41 | 4231.62 | 1.6263 |
| 101 | 528.758 | 533.661 | 4833.24 | 4249.19 | 2.05466 |

of the thermal conductivity in the $\Gamma$ to M direction ($\kappa_{xx}$) and in the $\Gamma$ to K' direction ($\kappa_{yy}$) with respect to $N_{\text{side}}$ is shown in Figure 4-3 and Table 4.1. While the SMRT solution converges a little more quickly, the iterative solution does not converge to within 1% until a discretization of at least $N_{\text{side}} > 90$. Also shown in Figure 4-4 is the evolution of the iterative solution for the case of $N_{\text{side}} = 101$. Due to the relaxation parameter $\alpha = 0.5$, a relatively large number of iterations is required for convergence.

The computational time per iteration is shown in Figure 4-5, and scales a little worse than $\mathcal{O}(N_{\text{side}}^3)$. Calculation of the distribution function from (4.29) involves a triple loop (over $i$, $j$, and $k$) and each loop variable has $\sim N_{\text{side}}^2$ values. Fortunately, the summation over $k$ can be eliminated by momentum conservation and the energy delta function should reduce the fullness of the array by about another factor of $N_{\text{side}}$, so this scaling is as expected. The computational cost refers to a single core of an AMD Opteron 6348 2.8 GHz processor.

## 4.8 Results using the iterative solution

For purposes of this discussion, the thermal conductivity calculated with $N_{\text{side}} = 81$ will be considered to be the converged result, which at room temperature is $\kappa_{xx} =$ 4772.4 W/mK along the $\Gamma$–M line and $\kappa_{yy} = 4216.31$ W/mK along the $\Gamma$–K' line

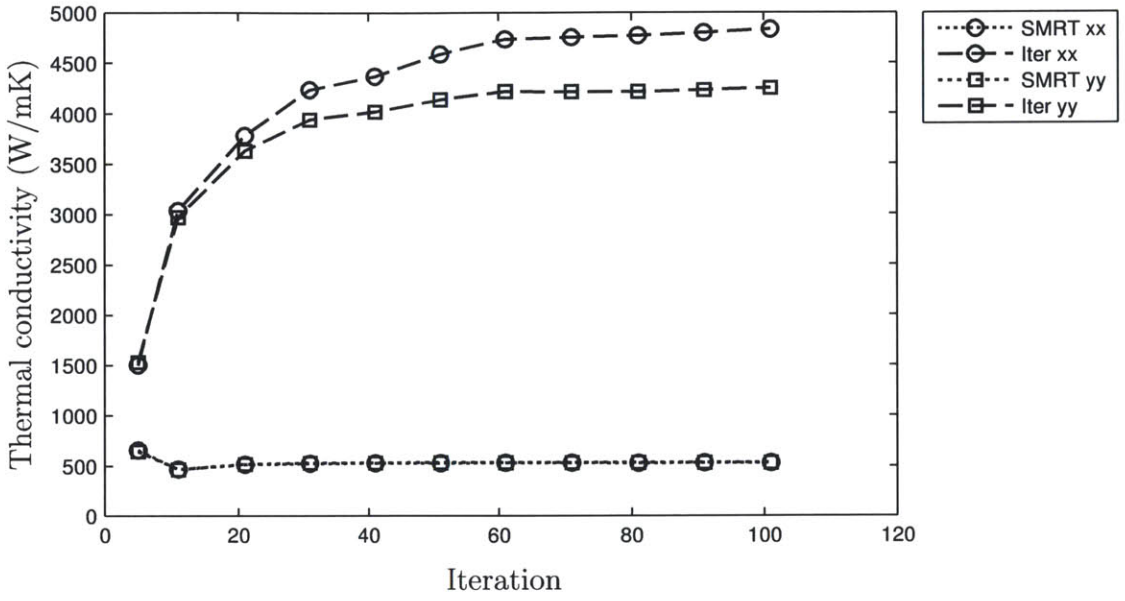


Figure 4-3: Convergence of the SMRT thermal conductivity and the iterative thermal conductivity.

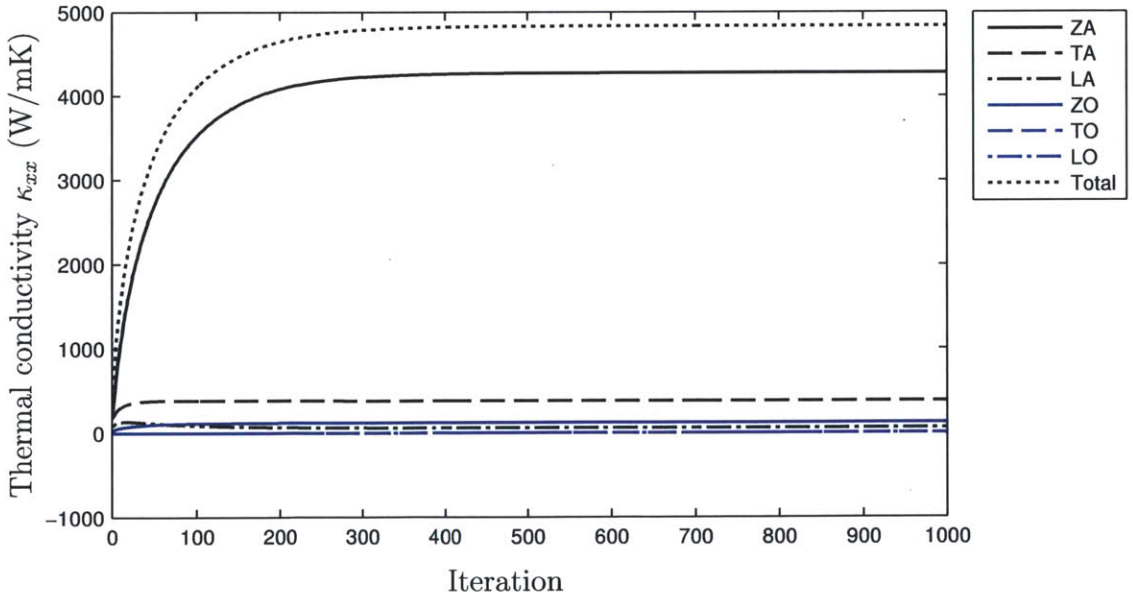


Figure 4-4: Evolution of the iterative solution with relaxation parameter $\alpha = 0.5$ for $N_{\text{side}} = 101$

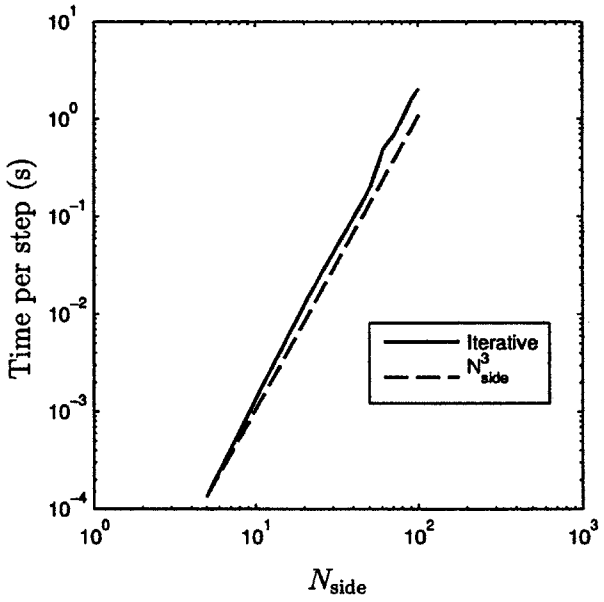


Figure 4-5: The computational time per step of the iterative method scales approximately as $N^3_{side}$ when calculated exploiting sparsity.

with approximately 85-88% of the energy being carried in the ZA branch. Based on the results of the previous section, this should be within a few percent of the converged result. The accuracy of these results depends upon the force constants used in this study. As seen from Table 2.3, the second order force constants produce a dispersion relation that is in reasonable agreement with other works [81, 64], but differing parameterizations for DFT can lead to discrepancies of a few percent for phonon energies [64] in the branches important for heat transfer (i.e. the lower 4 branches). Further studies are required to quantify the effect of the uncertainty of the second order force constants on thermal conductivity calculations.

Regarding the third order force constants, the Grüneisen parameter was reproduced also to within a few percent (see Figure 2-8 and Ref. [81]), but as mentioned in Section 3.1.2 the third order force constants fail to preserve required symmetries. To quantify the magnitude of the error related to the lack of symmetry, a symmetrized

interaction term is introduced that explicitly includes the required symmetry

$$\begin{aligned} 6|V_{3,\mathrm{sym}}(\lambda,\lambda',\lambda'')|^2 &= |V_3(\lambda,\lambda',\lambda'')|^2 + |V_3(\lambda',\lambda,\lambda'')|^2 \\ &\quad + |V_3(\lambda'',\lambda',\lambda)|^2 + |V_3(\lambda'',\lambda,\lambda')|^2 \\ &\quad + |V_3(\lambda',\lambda'',\lambda)|^2 + |V_3(\lambda,\lambda'',\lambda')|^2. \end{aligned} \tag{4.31}$$

This symmetrized interaction term results in similar convergence behavior (see Table 4.2) and a "converged" thermal conductivity at $N_{\mathrm{side}} = 81$ of $\kappa_{xx} = 3600.0$ W/mK and $\kappa_{yy} = 3452.7$ W/mK, which are 25% and 18% different, respectively, from the calculation with the unsymmetrized interaction term. The thermal conductivity resulting from the symmetrization of (4.31) is in closer agreement with other iterative solutions of the phonon BTE using empirical potentials instead of DFPT (see Table 4.3), so this symmetrized term will be used for the remainder of the calculations unless explicitly stated otherwise. The discrepancy between the thermal conductivity from the unsymmetrized $\tilde{V}_3$ term and the symmetrized one suggests that the uncertainty in this calculation is on the order of 20% due to errors in the calculation of the third order force constants in the DFPT calculations. However, it can be hoped that by using the symmetrized term the actual error is something significantly smaller. Nevertheless, with thermal conductivities that vary by almost an order of magnitude between the SMRT and iterative result and given the uncertainties inherent in measurement of thermal conductivity in graphene (e.g. [28]), the uncertainty of 20% is not unacceptable.

Two particular insights are readily apparent from the results in Table 4.3. First, the SMRT dramatically under predicts the thermal conductivity when relaxation times are calculated from the ab initio scattering operator. It is possible to develop phenomenological models for the relaxation time that bring this prediction into better agreement with experiments [84, 1], but as illustrated in a recent study, this agreement occurs only because of a fortuitous cancellation of errors [112]. Furthermore, the phenomenological models predict that the out-of-plane branches make no appreciable contribution to thermal transport at room temperature [9]. This is in striking contrast

Table 4.2: Convergence behavior of the iterative solution thermal conductivity with the symmetrized interaction term with respect to discretization $N_{\text{side}}$.

| $N_{\text{side}}$ | $\kappa_{xx,\text{SMRT}}$ | $\kappa_{yy,\text{SMRT}}$ | $\kappa_{xx}$ | $\kappa_{yy}$ |
|---|---|---|---|---|
| 5 | 601.592 | 596.219 | 1506.31 | 1470.11 |
| 11 | 475.032 | 487.7 | 2685.55 | 2633.86 |
| 21 | 511.508 | 531.447 | 3169.77 | 3075.36 |
| 31 | 515.766 | 535.619 | 3322.16 | 3213.01 |
| 41 | 513.974 | 533.485 | 3314.94 | 3201.4 |
| 51 | 515.053 | 534.232 | 3477.64 | 3352.01 |
| 61 | 514.843 | 533.824 | 3580.05 | 3444.97 |
| 71 | 514.433 | 533.322 | 3594.33 | 3453.11 |
| 81 | 513.147 | 531.925 | 3600.03 | 3452.74 |

to the ab initio thermal transport simulations that indicate the out-of-plane branches as the dominant carriers of thermal energy [71, 109, 113]. On this point, all the results shown in Table 4.3 agree.

In order to better compare these results to other solutions of the phonon BTE as well as to experiments, the effect of boundary scattering must also be included. Boundary effects can be approximated in a spatially homogenous simulation by introducing an additional scattering rate [22, 124] representing interaction with the boundaries [87, 77]. For circular Corbino membranes [21, 29, 34] this new scattering rate is

$$\Gamma_i^{\text{circ}} = \Gamma_i + \frac{||\boldsymbol{v}_i||}{L_{\text{b}}} \tag{4.32}$$

where $L_{\text{b}}$ is the membrane diameter.

Approximating the boundary scattering in this manner for an $L_{\text{b}} = 10\mu$m diameter Corbino membrane, which agrees with the geometry of available reference [71, 113], brings the predictions from this method into reasonable agreement with previous ab initio thermal transport simulations using empirical potentials (see Table 4.3). Introduction of the boundary scattering term may also slightly improve the convergence—see Table 4.4. While the goal of this work is to move beyond the homogeneous scattering rate approximation to boundaries, the implication that boundary scattering may allow use of a coarser discretization is important.

After introduction of the boundary scattering term, the iterative solution for the

Table 4.3: Thermal conductivity (along the Γ to M line where available) from this work and other sources as well as the relative importance of each branch in terms of total energy carried.

| Source | $\kappa$ | % ZA | % TA | % LA | % ZO | %TO | %LO |
|---|---|---|---|---|---|---|---|
| Unmodified | 4772.4 | 88.42 | 7.84 | 1.20 | 2.58 | -0.02 | -0.02 |
| $V_{3,\text{sym}}$ | 3600.0 | 86.10 | 9.10 | 2.47 | 2.37 | -0.02 | -0.02 |
| $L_\text{b} = 10\mu\text{m}$, $V_{3,\text{sym}}$ | 2999.0 | 83.06 | 10.78 | 3.57 | 2.63 | -0.02 | -0.02 |
| Ref. [113] | 3215.5 | 88.91 | 7.53 | 2.85 | 0.0072 | – | – |
| Ref. [71] | 3435 | 75.69 | 15.14 | 9.17 | – | – | – |

Table 4.4: Convergence behavior of the iterative solution thermal conductivity with the symmetrized interaction term and scattering rate including the homogenous approximation of Corbino membrane boundary scattering.

| $N_\text{side}$ | $\kappa_{xx,\text{SMRT}}$ | $\kappa_{yy,\text{SMRT}}$ | $\kappa_{xx}$ | $\kappa_{yy}$ |
|---|---|---|---|---|
| 5 | 586.142 | 581.441 | 1410.41 | 1379.84 |
| 11 | 466.665 | 479.598 | 2362.33 | 2323.28 |
| 21 | 503.737 | 523.637 | 2744.45 | 2680.45 |
| 31 | 509.111 | 528.771 | 2857.04 | 2787.18 |
| 41 | 507.951 | 527.207 | 2839.62 | 2769.46 |
| 51 | 509.308 | 528.227 | 2941.04 | 2868.39 |
| 61 | 509.304 | 528.022 | 3001.48 | 2926.51 |
| 71 | 509.05 | 527.672 | 3001.12 | 2925.62 |
| 81 | 507.889 | 526.401 | 2998.98 | 2922.05 |

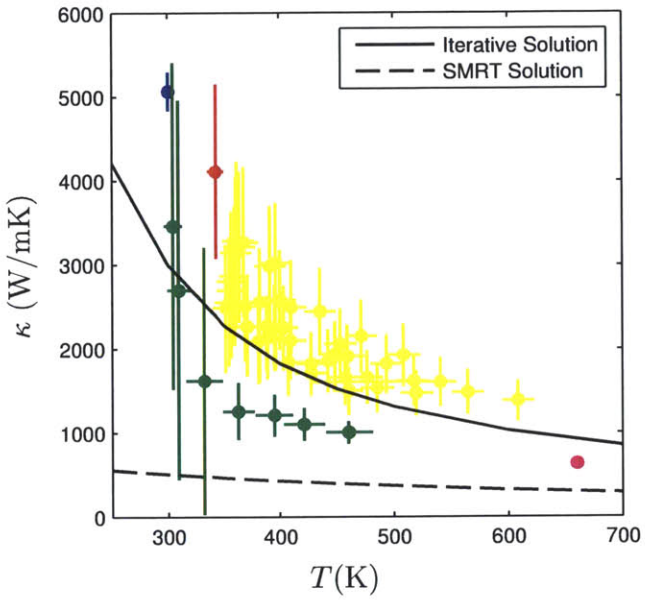


Figure 4-6: Temperature dependence of the iterative solution thermal conductivity compared to various recent experimental measurements (red [41], blue [10], yellow [29], green [69], magenta [34]). Calculated using the symmetrized interaction term and Corbino membrane scattering rate with $L_b = 10\mu$m.

thermal conductivity with the symmetrized interaction term and the appropriate boundary scattering is compared across a broad range of temperatures to experimental results. Although, from the error bars in Figure 4-6, it is apparent that the amount of uncertainty in the experiments is still remarkably high due to uncertainties in the experimental procedure [29], the iterative solution fits within the trend of the data as with previous ab initio thermal transport simulations [113, 71].

While a boundary scattering length of $10\mu$m is reasonable in terms of common experiments [21, 29, 34], the parameter $L_b$ can be varied to obtain estimates of the domain over which kinetic effects are important. Figure 4-7, which was generated using (4.32), shows the dependence of the effective thermal conductivity on the Knudsen number. The mean free path as calculated from (3.33) and (3.35) and (4.27) is shown in Figure 4-8. At room temperature, the mean free path of 600nm agrees well with other predictions [41, 98].

Figure 4-7 also includes a Landauer-like estimate for the effective thermal conduc-

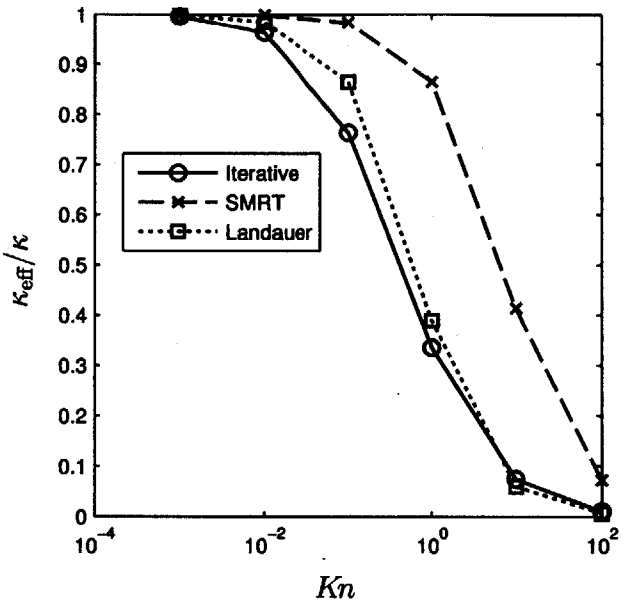


Figure 4-7: The effect of boundaries on thermal conductivity for the corbino membrane geometry [21] is estimated using the homogeneous scattering rate (4.32) as a function of membrane diameter $L_{\text{b}}$. Calculated with $N_{\text{side}} = 81$.

tivity [100, 98]

$$\frac{\kappa_{\text{eff}}(Kn)}{\kappa} = \frac{1}{1 + \frac{\pi}{2} Kn}, \tag{4.33}$$

This model is appealing because it uses only the Knudsen number to represent the transition from diffusive to collisionless transport, and it is expected to be correct in those two limits–see Chapter 7 for more details. As shown in Figure 4-7, the iterative solution predicts transitional regime transport over a broader range of $Kn$ than Equation (4.33). The effect of the boundaries is shown to be important diameters from 60nm to 60$\mu$m ($0.01 \lesssim Kn \lesssim 10$). At a diameter of 10$\mu$m, the effective thermal conductivity is only about 80% of the true thermal conductivity. The longevity of the kinetic effects agrees generally with the same analysis for graphene performed using empirical potentials [112]; although in that work, the logarithmic scale of the $y$-axis makes exact comparison difficult. The SMRT approximation fails to capture the appropriate trend of the thermal conductivity reduction.

This broad transition regime has important implications for experiments. For example, the experiments referenced in Figure 4-6 span Knudsen numbers from about

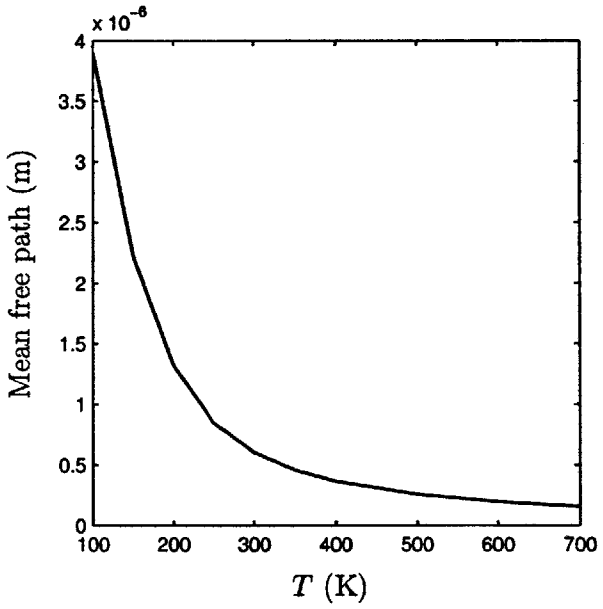


Figure 4-8: The mean free path of phonons in graphene varies from 600 nm at 300 K to 160 nm at 700 K.

0.06 to about 0.02, all within the transition regime. Based on the results of Figure 4-7, neglecting kinetic effects would lead to errors on the order of 5-10% in thermal conductivity calculations. Considering the level of uncertainty in these experiments and even in the ab initio calculation, perhaps this error is acceptable, but for membrane diameters less than 10 microns, kinetic effects may no longer be neglected.

This analysis relies on a homogeneous approximation of boundary scattering including the Matthiessen rule. This is known to yield incorrect results both in terms of localized transport [124] and in terms of averaged effective thermal conductivity [67] as we will show in Chapter 7. The simulation method that is presented hereafter provides a means to model these systems without the homogeneous approximation.

# Chapter 5

# Phonon Scattering as a Linear System of ODEs

The spatially inhomogeneous, time dependent phonon Boltzmann equation (3.19) is not amenable to analytical solutions. The two primary processes involved (namely advection and scattering) each introduce unique challenges: the advection propagates discontinuities and leads to numerical instabilities, while the scattering events, as shown in the previous chapters, are cumbersome to describe mathematically.

Solution is significantly simplified if these two processes are treated separately via a splitting algorithm wherein the system is updated by a small time increment $\Delta t$ due to the action of one of these (e.g. homogeneous relaxation for the scattering step), while the other is assumed inactive. Subsequently, the system is updated for the other (e.g. ballistic advection), while the first is assumed inactive [12, 104].

This chapter will describe the fundamentals for developing a time stepping algorithm for the scattering operator which will be arrived at after a few simple manipulations of the governing equations (3.19) and (4.27). The resulting propagator will integrate the homogeneous scattering step exactly (no time step error) and will interface naturally with variance-reduced Monte Carlo solutions of the Boltzmann equation presented in the subsequent chapter.

## 5.1 Matrix formulation

In order to exploit the linearity of the scattering model (4.27), we proceed to write it in matrix form (similar to Ref. [88])

$$\dot{n}_i^{\mathrm{d}} = \sum_j A_{ij} n_j^{\mathrm{d}}, \tag{5.1}$$

where the elements of the transition rate matrix are

$$A_{\bar{i}\bar{j}} = \frac{A_{\mathrm{uc}}}{2\pi\hbar^2} \frac{1}{n_{\bar{j}}^0(n_{\bar{j}}^0+1)} \Big( \sum_{ijk} \big[ C_{\mathrm{I}}(i,j,k) \left( -\delta_{i,\bar{i}}\delta_{j,\bar{i}} - \delta_{i,\bar{i}}\delta_{j,\bar{j}} + \delta_{i,\bar{i}}\delta_{k,\bar{j}} \right) + C_{\mathrm{II}}(i,j,k) \left( -\delta_{i,\bar{i}}\delta_{j,\bar{i}} + \delta_{i,\bar{i}}\delta_{j,\bar{j}} + \delta_{i,\bar{i}}\delta_{k,\bar{j}} \right) \big] \Big) \tag{5.2}$$

The homogeneous relaxation problem now corresponds to the well studied problem of a system of coupled ODEs [80], from which a time integration scheme will be developed.

## 5.2 Energy formulation

One highly desirable feature of numerical integration scheme is conservation of system energy. Implementation of a numerical scheme that exactly conserves energy will be facilitated by rewriting the governing equations in terms of energy distributions ($\hbar\omega_\lambda n_\lambda$) rather than phonon densities [91]. For convenience, the formulation will also include the density of states and a constant multiplier, namely

$$f_i = \frac{2}{A_{\mathrm{uc}} N_{\mathrm{tri}} \delta} \hbar\omega_i n_i. \tag{5.3}$$

The analytical decomposition (3.16) then becomes

$$f_i = f^{\mathrm{eq}}(\omega_i; T_0) + f_i^{\mathrm{d}} \tag{5.4}$$

and the equilibrium distribution is

$$f^{\mathrm{eq}}(\omega;T) = \frac{2}{A_{\mathrm{uc}}\,N_{\mathrm{tri}}\delta}\frac{\hbar\omega}{\exp\left(\frac{\hbar\omega}{k_{\mathrm{b}}T}\right)-1}, \tag{5.5}$$

From Equation (4.9), the energy density of a system is given by

$$u = \frac{2}{A_{\mathrm{uc}}\,N_{\mathrm{tri}}\delta}\sum_{i=1}^{N_{\mathrm{states}}}\hbar\omega_i n_i, \tag{5.6}$$

and the deviational energy density of a system $u_{\mathrm{d}} = u - u_0$—where $u_0$ is the energy density of a system at equilibrium at $T_0$—is given by

$$u = \sum_{i=1}^{N_{\mathrm{states}}} f_i^{\mathrm{d}} + u_0. \tag{5.7}$$

For later purposes we also note that the heat flux is given by

$$\boldsymbol{J_E} = \sum_{i=1}^{N_{\mathrm{states}}} \boldsymbol{v}_i f_i^{\mathrm{d}}. \tag{5.8}$$

The scattering operator now becomes

$$\dot{f}_i^{\mathrm{d}} = \sum_j B_{ij} f_j^{\mathrm{d}}, \tag{5.9}$$

where the transition matrix for energy distributions ($B_{ij}$) is related to the transition matrix for number of phonons by

$$B_{ij} = A_{ij}\frac{\omega_i}{\omega_j}. \tag{5.10}$$

In terms of energy deviations, the Boltzmann equation is simply

$$\frac{\partial f_i^{\mathrm{d}}(\boldsymbol{x},t)}{\partial t} + \boldsymbol{v}_i\cdot\nabla_{\boldsymbol{x}} f_i^{\mathrm{d}}(\boldsymbol{x},t) + \boldsymbol{v}_i\cdot\nabla_{\boldsymbol{x}} T(\boldsymbol{x})\left.\frac{\partial f^{\mathrm{eq}}(\omega_i;T(\boldsymbol{x}))}{\partial T}\right|_{T_0} = \sum_j B_{ij} f_j^{\mathrm{d}}(\boldsymbol{x},t), \tag{5.11}$$

where the time and space dependence of the distribution function is shown explicitly.

We reiterate that the iterative solution [87] introduced first in Chapter 4 and presented in discrete form in (4.29), is an implementation of standard iterative approaches for solution of matrix equations [118] that iterates toward the steady state distribution more efficiently at the cost of discarding all information about the transient behavior. The steady-state, spatially homogeneous (with a 1-d temperature gradient) LHS of the Boltzmann equation (from (5.11)) is

$$\cancelto{0}{\frac{\partial f_i^{\mathrm{d}}}{\partial t}} + \boldsymbol{v}_i \cdot \cancelto{0}{\nabla_{\boldsymbol{x}} f_i^{\mathrm{d}}} + v_{x,i} \left.\frac{\partial f^{\mathrm{eq}}(\omega_i;T)}{\partial T}\right|_{T_0} \frac{\mathrm{d}T}{\mathrm{d}x} = \sum_j B_{ij} f_j^{\mathrm{d}}(t=\infty), \tag{5.12}$$

whose solution can be found iteratively through the recursion

$$f_i^{\mathrm{d}} = -\frac{v_{x,i}}{B_{ii}} \left.\frac{\partial f^{\mathrm{eq}}(\omega;T)}{\partial T}\right|_{T_0} + \frac{1}{B_{ii}} \sum_{j \neq i} B_{ij} f_j^{\mathrm{d}}. \tag{5.13}$$

This is slightly different from (4.29) in two ways. The most obvious difference is that (5.13) is in terms of $f^{\mathrm{d}}$ instead of $n^{\mathrm{d}}$. The second difference is more subtle—the contribution to the scattering rate $\Gamma_i$ from pathways with repeated indices is too small by a factor of 2, whereas $B_{ii}$ here correctly includes the contribution of both of the repeated states–see Equation (3.32) and the text thereafter. The first of these two differences should have no impact on thermal transport and the second should have only minimal impacts. As can be seen from Table 5.1, this matrix formulation agrees well with the convergence behavior of Equation (4.29). The differences at each discretization level are negligible.

Table 5.1: Comparison of the SMRT and the iterative thermal conductivity from the matrix formulation with the original formulation (see Table 4.2–i.e. no symmetrization of the interaction term) for the first few discretizations.

| $N_{\mathrm{side}}$ | $\kappa_{xx,\mathrm{SMRT}}$ | % diff | $\kappa_{xx}$ | % diff |
|---|---|---|---|---|
| 5 | 600.697 | 1.5 | 1506.31 | 0.2e-6 |
| 11 | 474.612 | 0.08 | 2685.55 | 0.7e-6 |
| 21 | 511.406 | 0.02 | 3169.77 | 0.9e-6 |
| 31 | 515.713 | 0.01 | 3322.16 | 1.1e-6 |
| 41 | 513.941 | 0.006 | 3314.94 | 1.3e-6 |
| 51 | 515.033 | 0.004 | 3477.64 | 1.5e-6 |

## 5.3 Numerical issues for energy conservation

Energy conservation demands that the system energy remain invariant during the scattering processes. In the three phonon picture, this is satisfied because the coupled states are selected such that $\omega_\lambda + \omega_{\lambda'} - \omega_{\lambda''} = 0$. Due to the linearization and linear interpolation necessary for the ab initio thermal transport methods, and then the reformulation into matrix form, three phonon scattering is essentially calculated by considering sequentially all combinations of the pairs of phonons involved in scattering process–represented by the two indices of the transition matrix $B_{ij}$. As a result, it is more convenient to write the conservation requirement in terms of net energy transfer. The rate energy density is removed from a system due to the scattering process is equal to

$$\dot{u}^{\text{out}} = -\sum_j B_{jj} f_j^{\text{d}}, \tag{5.14}$$

which, due to the sign of the diagonal elements, $B_{ii}$, should be positive. The rate energy density is added to the system during the scattering process is

$$\dot{u}^{\text{in}} = \sum_{ij} B_{ij}(1 - \delta_{ij}) f_j^{\text{d}} \tag{5.15}$$

The balance is then simply

$$\sum_i \dot{f}_i^{\text{d}} = 0 = \sum_{ij} B_{ij} f_j^{\text{d}}, \tag{5.16}$$

which leads to the requirement

$$\sum_i B_{ij} = 0. \tag{5.17}$$

In order to consider momentum conservation we briefly revert to the number density formulation and the transition matrix $A$. The scattering matrix is decomposed into normal and umklapp processes ($\boldsymbol{A} = \boldsymbol{A}^{\text{N}} + \boldsymbol{A}^{\text{U}}$). For momentum conserving

normal processes, momentum conservation is equivalent to

$$\sum_i \boldsymbol{q}_i A^{\mathrm{N}}_{ij} = 0. \tag{5.18}$$

Returning to the energy based formulation, the momentum conservation statement is

$$\sum_i \frac{\boldsymbol{q}_i}{\omega_i} B^{\mathrm{N}}_{ij} = 0. \tag{5.19}$$

Given the use of a finite grid and linear interpolation, as well as the possibility of numerical errors in the force constants, one should not expect energy to be conserved exactly. Expressions (5.17) and (5.19) will thus not be satisfied. Let the calculated transition matrix elements be denoted $\tilde{B}_{ij}$, such that, due to numerical errors in its calculation,

$$\sum_i \tilde{B}_{ij} = \Delta_j \neq 0, \tag{5.20}$$

$$\sum_i \frac{q_{x,i}}{\omega_i} \tilde{B}^{\mathrm{N}}_{ij} = \Delta^{\mathrm{N}}_{x,j} \neq 0, \tag{5.21}$$

$$\sum_i \frac{q_{y,i}}{\omega_i} \tilde{B}^{\mathrm{N}}_{ij} = \Delta^{\mathrm{N}}_{y,j} \neq 0. \tag{5.22}$$

In order to understand this measure of lack of conservation, it is useful to consider the physical implications of the scattering transition matrix. The off diagonal elements $B_{ij}$ represent the rate energy from a state $j$ moves to state $i$ and the diagonal elements represent the rate that the energy in state $j$ is changed—if energy is conserved, then rate energy goes from $j$ into any other state should be equal to the rate that energy in state $j$ is depleted. Equation (5.20) provides a measure of the rate at which energy is created or destroyed (based on the sign of $\Delta_j$) due to energy occupying state $j$. If the amount of energy created or destroyed $|\Delta_j|$ is small compared to the total rate of energy being moved (measured conveniently by $\sum_i |B_{ij}|$), then the lack of conservation is of less importance. Consequently, a convenient measure of the average rate of lack of conservation compared to the total rate of energy transfer

(with each state being weighted by the rate of energy transfer for that state) is

$$\epsilon_\omega = \frac{1}{\sum_{ij}|\tilde{B}_{ij}|}\sum_j \frac{|\Delta_j|\sum_i|\tilde{B}_{ij}|}{\sum_i|\tilde{B}_{ij}|} = \frac{\sum_j|\Delta_j|}{\sum_{ij}|\tilde{B}_{ij}|}, \tag{5.23}$$

and similarly for momentum conservation in normal processes

$$\epsilon_x = \frac{\sum_j|\Delta^{\mathrm{N}}_{x,j}|}{\sum_{ij}\left|\frac{q_{x,i}}{\omega_i}\tilde{B}_{ij}\right|}, \tag{5.24}$$

$$\epsilon_y = \frac{\sum_j|\Delta^{\mathrm{N}}_{y,j}|}{\sum_{ij}\left|\frac{q_{y,i}}{\omega_i}\tilde{B}_{ij}\right|}. \tag{5.25}$$

The value of these conservation faults shown in Table 5.2 and Figure 5-1 converge to a non-zero value on the order of $10^{-1}$. This non-vanishing error indicates one of three things: 1) a bug in numerical implementation, 2) a problem with the theory or 3) errors in the force constants used in this study. In order to have confidence in the primary contributions of this work, the first two of these must be ruled out.

Table 5.2: Conservation faults for the scattering operator in matrix form vs discretization for the unsymmetrized interaction term.

| $N_{\mathrm{side}}$ | $\epsilon_\omega$ | $\epsilon_x$ | $\epsilon_y$ |
|---|---|---|---|
| 5 | 0.260854 | 0.263774 | 0.291882 |
| 11 | 0.108108 | 0.208469 | 0.215358 |
| 21 | 0.0746952 | 0.144109 | 0.154785 |
| 31 | 0.068881 | 0.127416 | 0.13876 |
| 41 | 0.0620872 | 0.1161 | 0.127466 |
| 51 | 0.0610346 | 0.112865 | 0.125237 |
| 61 | 0.0585888 | 0.111636 | 0.122857 |
| 71 | 0.0562385 | 0.110827 | 0.122514 |
| 81 | 0.0557885 | 0.108008 | 0.118863 |

As previously argued, the lack of symmetry of the interaction term $\tilde{V}_3$ should directly contribute to this error. To illustrate this, consider the results in Table 5.3 which presents the conservation faults calculated using the symmetrized interaction terms (4.31). The symmetrization reduces the conservation fault by nearly a factor of 2 for energy and a slightly better for momentum. The symmetrized interaction

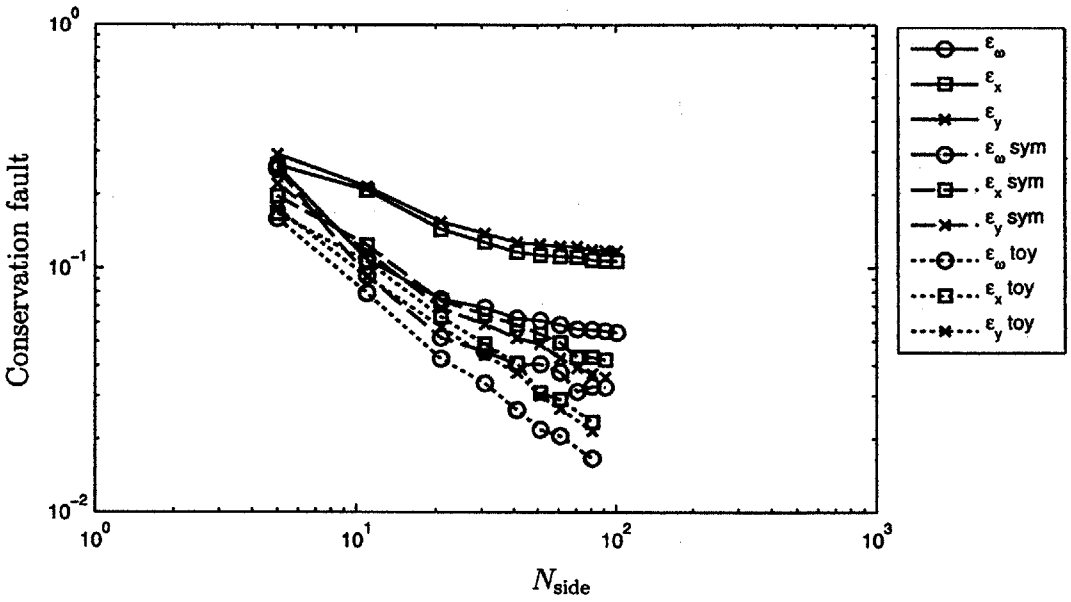


Figure 5-1: Conservation faults do not appear to converge to zero as discretization $N_{\text{side}}$ is increased for the unsymmetrized interaction term, but may do so for the symmetrized term and certainly appear to do so for the toy model of Equation (5.26).

term may indeed eliminate conservation faults entirely, but with the available computational resources and time, a conclusive convergence study was not feasible.

Table 5.3: Conservation faults for the scattering operator in matrix form vs discretization using the symmetrized interaction element from Equation (4.31).

| $N_{\text{side}}$ | $\epsilon_\omega$ | $\epsilon_x$ | $\epsilon_y$ |
|---|---|---|---|
| 5 | 0.253839 | 0.196822 | 0.221322 |
| 11 | 0.0929621 | 0.124286 | 0.116467 |
| 21 | 0.0518293 | 0.0733655 | 0.0683349 |
| 31 | 0.045572 | 0.0646509 | 0.0589449 |
| 41 | 0.040336 | 0.0584694 | 0.0516954 |
| 51 | 0.0404563 | 0.0537662 | 0.0487405 |
| 61 | 0.0375152 | 0.0495192 | 0.0427301 |
| 71 | 0.0311938 | 0.0431613 | 0.0389457 |
| 81 | 0.032736 | 0.0430679 | 0.0369658 |

In order to help to rule out implementation bugs or problems with the theory, the interaction term is replaced with a simplistic approximation motivated by Klemens' popular form for the relaxation time for Debye solids [56, 57, 59, 112], but modified

here in that we do not require any approximate relationships between $\lambda$, $\lambda'$, and $\lambda''$ and also modified to preserve they symmetry of the more complicated dispersion relation. The toy model is

$$|\tilde{V}_3(\lambda,\lambda',\lambda'')| = \frac{\hbar^3}{M_{\text{atom}}}(\gamma_\lambda\gamma_{\lambda'}\gamma_{\lambda''})^{2/3}(\omega_\lambda\omega_{\lambda'}\omega_{\lambda''})(|\boldsymbol{q}|\,|\boldsymbol{q}'|\,|\boldsymbol{q}''|)^{2/3}, \tag{5.26}$$

where $\gamma_\lambda$ is the Grüneisen parameter. In order to isolate this approximation from the force constants, and given the level of approximation, the Grüneisen parameter will be approximated as uniformly equal to 1. Equation (5.26) is properly symmetric and has the right units, but it is presented with no further justification and is not expected to provide any reasonable accuracy in thermal transport calculations. It will only be used to demonstrate that lack of conservation can disappear when the interaction term is appropriately chosen, which is shown in Figure (5-1).

The results of this section suggest that the lack of conservation arises from the anharmonic force constants used in this study and specifically from the lack of symmetry of the force constants. In any case, the lack of conservation is relatively small (only a few percent) especially when using the symmetrized interaction term. The error is further mitigated because the signs of $\Delta_j$ and the related measures of momentum conservation faults are both positive and negative, so while one state loses energy another state gains it and the lack of conservation of the system as a whole is an order of magnitude better than reflected by (5.23). Due to the relatively small magnitude and the rapid convergence of the iterative method, these conservation faults tend not to be an issue for the iterative solution, but in order to perform explicit time integration of the phonon scattering operator, these conservation faults must be eliminated.

## 5.4 Enforced conservation

As will be detailed in Chapter 6, the particle scheme developed for integrating (5.11) is exactly energy conserving. This is a very desirable feature, which however does not tolerate any error (in terms of lack of energy conservation) in the matrix elements $B_{ij}$.

In order to address the lack of conservation due to numerical errors in the interaction element and the finite discretization, an additive correction $\beta_{ij}$ is proposed such that the calculated matrix element $\tilde{B}_{ij}$ plus the correction satisfies energy conservation or

$$B_{ij} = \tilde{B}_{ij} + \beta_{ij}. \tag{5.27}$$

This leads to a constraint equation

$$\sum_i \beta_{ij} = -\Delta_j \tag{5.28}$$

The magnitude of each element $\beta_{ij}$ should be small in order to minimize the unintended impacts of this correction. If formulated as a constrained optimization (Lagrange multiplier), the objective function is

$$F_j = \sum_i \beta_{ij}^2 + \lambda_j \left( \sum_i \beta_{ij} + \Delta_j \right). \tag{5.29}$$

After differentiation with respect to $\beta_{mn}$,

$$\frac{\partial F_j}{\partial \beta_{mn}} = 2\beta_{mn} + \lambda_n, \tag{5.30}$$

one fines that the minimum occurs at $\beta_{mn} = -\frac{\lambda_n}{2}$. Using (5.28), it is determined that

$$\beta_{ij} = \frac{\Delta_j}{N_{\text{states}}} \tag{5.31}$$

Thus, an "optimal" correction is constructed for the calculated transition matrix in order to conserve energy simply by adding back the mean of the deficit of each column to each of the $N_{\text{states}}$ elements of the column. If we decompose the scattering into momentum conserving normal process, and non conservative umklapp processes $B_{ij} = B_{ij}^{\text{U}} + B_{ij}^{\text{N}}$, then, in a related manner both energy and momentum conservation can be corrected for the normal processes by considering $B_{ij}^{\text{N}} = \tilde{B}_{ij}^{\text{N}} + \beta_{ij}^{\text{N}}$. Again using Lagrange multipliers to minimize the size of the correction results in an objective

Table 5.4: Comparison of the thermal conductivities calculated with the energy and momentum corrections. Calculated at $N_{\text{side}} = 21$.

| Source | $\kappa_{xx,\text{SMRT}}$ | $\kappa_{yy,\text{SMRT}}$ | $\kappa_{xx}$ | $\kappa_{yy}$ |
|---|---|---|---|---|
| Sym, no correction | 511.406 | 531.335 | 3169.77 | 3075.36 |
| Sym, energy correction | 511.431 | 531.37 | 3169.77 | 3075.36 |
| Sym, both corrections | 510.51 | 530.404 | 3099.31 | 3013.94 |

function

$$\begin{aligned} F_j^{\text{N}} &= \sum_i (\beta_{ij}^{\text{N}})^2 + \lambda_j \left( \sum_i \beta_{ij}^{\text{N}} + \Delta_j^{\text{N}} \right) \\ &+ \lambda_{x,j} \left( \sum_i \frac{q_{x,i}}{\omega_i} \beta_{ij}^{\text{N}} + \Delta_{x,j}^{\text{N}} \right) + \lambda_{y,j} \left( \sum_i \frac{q_{y,i}}{\omega_i} \beta_{ij}^{\text{N}} + \Delta_{y,j}^{\text{N}} \right). \end{aligned} \tag{5.32}$$

After minimization the correction is prescribed by

$$2\beta_{ij}^{\text{N}} = -\lambda_j - \frac{q_{x,i}}{\omega_i} \lambda_{x,j} - \frac{q_{y,i}}{\omega_i} \lambda_{y,j} \tag{5.33}$$

with the multipliers being obtained by inverting the linear system

$$\begin{bmatrix} \sum_i 1 & \sum_i \frac{q_{x,i}}{\omega_i} & \sum_i \frac{q_{y,i}}{\omega_i} \\ \sum_i \frac{q_{x,i}}{\omega_i} & \frac{\sum_i q_{x,i}^2}{\omega_i^2} & \sum_i \frac{q_{x,i} q_{y,i}}{\omega_i^2} \\ \sum_i \frac{q_{y,i}}{\omega_i} & \sum_i \frac{q_{x,i} q_{y,i}}{\omega_i^2} & \sum_i \frac{q_{y,i}^2}{\omega_i^2} \end{bmatrix} \begin{bmatrix} \lambda_j \\ \lambda_{x,j} \\ \lambda_{y,j} \end{bmatrix} = \begin{bmatrix} 2\Delta_j^{\text{N}} \\ 2\Delta_{x,j}^{\text{N}} \\ 2\Delta_{y,j}^{\text{N}} \end{bmatrix}. \tag{5.34}$$

We note that it should also be possible to determine the exact number of reciprocal lattice vectors expected to be added by the umklapp process and strictly enforce it in a similar manner, but we expect the effects to be small. Enforcing energy conservation had minimal impact on the thermal conductivity and enforcing momentum conservation tended to change the values of thermal conductivity by less than a few percent. The thermal conductivity for the system with energy conservation is shown in Table 5.4.

Perhaps the greatest drawback of the enforced energy conservation approach is that it destroys the sparsity of the transition matrix. As a result, the calculation time per iteration will scale as $\mathcal{O}(N_{\text{side}}^4)$ instead of $\mathcal{O}(N_{\text{side}}^3)$. An alternative to the

above enforced conservation scheme would be to spread the correction over only the non-zero elements of the transition matrix. This approach would preserve the sparsity of the transition matrix and the more efficient scaling, but the correction does not affect all directions equally. As a result it tends to bias the thermal conductivity more than adding the correction to every element in each column. Furthermore, the time integration scheme that will be described hereafter also causes a loss of sparsity. Ultimately, the effect of the "gentler correction" (applied to all matrix elements) is not so detrimental.

## 5.5 Solution of homogeneous relaxation problem

Having posed the problem in terms of a matrix equation representing a system of first order ODEs, there are a number of solution methods available. This section presents a few such methods written in terms of the transition matrix and energy distributions. The most important contribution of this section is the development of the propagator that facilitates the step wise integration in time required for the homogeneous relaxation part of the splitting scheme.

Before presenting a time stepping solution we begin by noting that the homogeneous relaxation problem:

$$\dot{f}_i^{\mathrm{d}}(t) = \sum_j B_{ij} f_j^{\mathrm{d}}(t). \tag{5.35}$$

can be solved analytically

$$f_i^{\mathrm{d}}(t) = \sum_{j=1}^{N_{\mathbf{states}}} h_j g_{j,i} e^{\zeta_j t}, \tag{5.36}$$

where $g_{j,i}$ is the $i$th element of the $j$th eigenvector, $\zeta_j$ is the corresponding eigenvalue, and $h_j$ is a coefficient prescribed by the initial condition. When $N_{\mathbf{states}}$ is small and the problem is homogeneous (i.e. the spatial derivative on the left hand side of (3.1) is zero), this is a powerful method for solving the scattering part of the phonon Boltzmann equation. Nevertheless for large systems, the computational cost associated with solving for the eigenvalues and eigenvectors can be limiting.

The solution of 5.35 is also conveniently expressed by

$$f_i^{\mathrm{d}}(t+\Delta t) = \sum_j P_{ij}(\Delta t) f_j^{\mathrm{d}}(t) \tag{5.37}$$

where $P_{ij}$ are the elements of the generator or propagator matrix [68] Although we have chosen to reserve the bold symbol notation only for cartesian vectors, we will briefly violate that convention to prescribe the form for the propagator

$$\boldsymbol{P}(t) = e^{\boldsymbol{B}t} = \sum_{k=0}^{\infty} \frac{t^k}{k!} \boldsymbol{B}^k. \tag{5.38}$$

where $\boldsymbol{P}$ is a $N_{\mathbf{states}} \times N_{\mathbf{states}}$ matrix and contains all the information about the dynamics of the system. We note that number of computations required to calculate the propagator scales as $N_{\mathbf{states}}^4$, but it can be done once for each timestep size and stored to disk. We use a scale and square method to calculate the propagator which guarantees stability in the calculation of the same [80].

The propagator of the system can be used to sequentially step forward in time by the recursion

$$\boldsymbol{P}(n\Delta t) = [\boldsymbol{P}(\Delta t)]^n. \tag{5.39}$$

This discrete time stepping allows the distribution function to be integrated forward in time with no truncation error.

## 5.6 Deterministic scheme for evaluating spatially homogenous, time dependent Boltzmann

In the case of a homogeneous relaxation, the Boltzmann equation simplifies to

$$\frac{\partial f_i^{\mathrm{d}}(t)}{\partial t} + \boldsymbol{v}_i \cdot \cancelto{0}{\nabla_{\boldsymbol{x}} f_i^{\mathrm{d}}(t)} + v_{x,i} \left.\frac{\partial f^{\mathrm{eq}}(\omega_i; T)}{\partial T}\right|_{T_0} \frac{\mathrm{d}T}{\mathrm{d}x} = \sum_j B_{ij} f_j^{\mathrm{d}}(t). \tag{5.40}$$

This can be evaluated deterministically using the splitting scheme discussed previously. In the advection sub step, the distribution is updated according to

$$\frac{\partial f_i^{\mathrm{d}}(t)}{\partial t} + v_{x,i} \left.\frac{\partial f^{\mathrm{eq}}(\omega_i;T)}{\partial T}\right|_{T_0} \frac{\mathrm{d}T}{\mathrm{d}x} = 0 \tag{5.41}$$

which using a first order forward Euler scheme gives

$$f_i^{\mathrm{d,advect}}(t+\Delta t) = f_i^{\mathrm{d}}(t) - \Delta t\, v_{x,\lambda} \left.\frac{\partial f^{\mathrm{eq}}(\omega_i;T)}{\partial T}\right|_{T_0} \frac{\mathrm{d}T}{\mathrm{d}x}, \tag{5.42}$$

This is followed by the RHS update which utilizes the propagator introduced in Section 5.5 to integrate in time (with no timestep error)

$$f_i^{\mathrm{d}}(t+\Delta t) = \sum_j P_{ij}(\Delta t) f_i^{\mathrm{d,advect}}(t+\Delta t), \tag{5.43}$$

This deterministic method requires $\mathcal{O}(N_{\mathrm{states}})$ calculations for the LHS update and $\mathcal{O}(N_{\mathrm{states}}^2)$ calculations for the RHS update. This scaling could potentially be improved to $\sim \mathcal{O}(N_{\mathrm{states}}^{3/2})$ like the iterative method if sparsity is preserved by using the first order approximation of the propagator

$$P_{ij} \approx \delta_{ij} + B_{ij}\Delta t, \tag{5.44}$$

where $\delta_{ij}$ is the Kronecker delta and momentum and energy conservation of $B_{ij}$ have been calculated in a manner that preserves sparsity. Unlike the iterative method, this approach provides the correct time-dependent dynamics of the distribution function, but due to the difficulties associated with spatial integrations in a deterministic scheme and the advantages of a stochastic integration, the deterministic scheme will only be employed in the homogeneous case.

## 5.7 Propagator validation

In this section, the homogeneous relaxation of a system with no driving force (i.e. $\nabla_{\boldsymbol{x}} = 0$) with only three states is investigated with the deterministic time stepping scheme of Section 5.6. The relaxation behavior predicted by this scheme is compared to the eigenvalue decomposition solution from (5.36). Specifically, the system to be solved is

$$\frac{\mathrm{d}f_i^{\mathrm{d}}}{\mathrm{d}t} = \sum_j B_{ij} f_j^{\mathrm{d}} \tag{5.45}$$

which is chosen to have a transition matrix

$$B = \begin{bmatrix} -0.03 & 0.025 & -0.015 \\ 0.04 & -0.05 & 0.025 \\ -0.01 & 0.025 & -0.01 \end{bmatrix} \tag{5.46}$$

with the initial condition

$$\begin{bmatrix} f_1^{\mathrm{d}}(0) \\ f_2^{\mathrm{d}}(0) \\ f_3^{\mathrm{d}}(0) \end{bmatrix} = \begin{bmatrix} -10 \\ 1 \\ 9 \end{bmatrix}. \tag{5.47}$$

These parameters have been chosen to illustrate the complexity of the dynamics that may exist within this framework, while still being somewhat representative of the phonon system (i.e. having negative diagonal elements, columns that sum to one, and distribution function that sums to zero). The time stepping solution uses a time step of $\Delta t = 1$ and extends to $t = 300$, but because the propagator introduces no time step error and it is a homogenous relaxation, the time step does not affect the results. The results can be seen in Figure 5-2. The coupling between states in this simple example introduces dynamics that could not be captured by the SMRT exponential decay of each state.

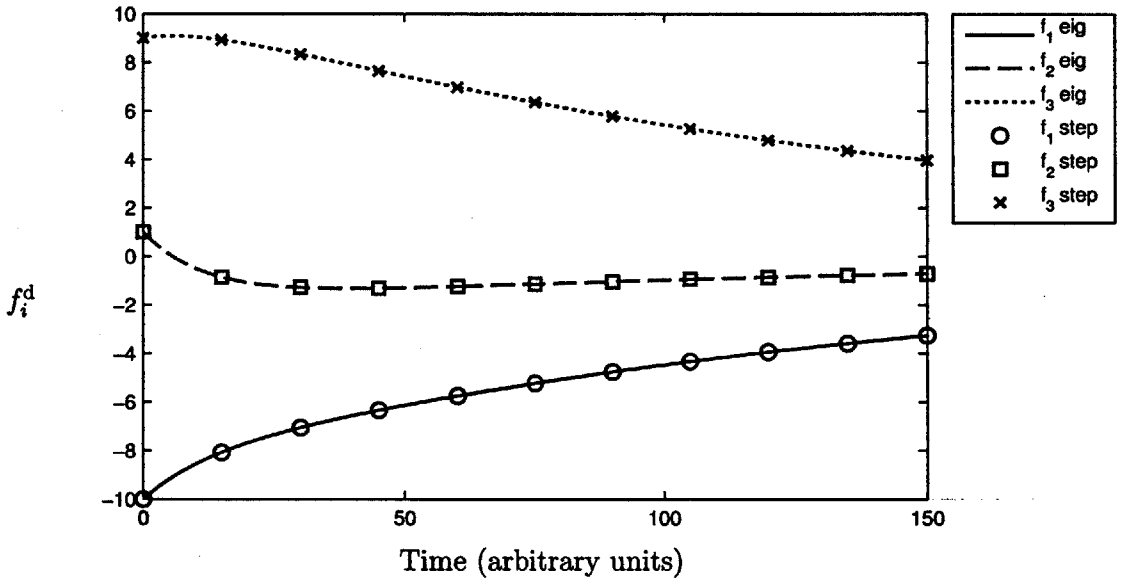


Figure 5-2: Toy problem compares the eigenvalue decomposition solution (Equation (5.36)—denoted by "eig") and the propagator stepping solution (Equation (5.37)—denoted by "step") for a three state, homogeneous relaxation. The two solutions are in perfect agreement.

# Chapter 6

# Stochastic particle method

Monte Carlo methods can be used to create stochastic integration techniques for generating samples of the distribution function that solves the non equilibrium, transient dynamics of the Boltzmann equation. For example, in the related case of rarefied gas dynamics, such methods have been shown to converge to the correct solution of the governing Boltzmann equation given suitable choices of numerical parameters (e.g. sufficiently small time step, sufficiently large number of particles, sufficiently small spatial cell) [104, 120].

Due to the stochastic nature of MC methods, simulation results are typically interpreted by sampling the distribution function to obtain statistical estimates of its moments, which correspond to macroscopic observables of interest (e.g. energy, and heat flux). The associated stochastic noise has a standard deviation that scales with the square root of the number of independent samples [47, 45]. This unfavorable scaling means the simulation cost must increase by a factor of $M^2$ in order to reduce the uncertainty by a factor of $M$; on the other hand, this means that the computational cost can be reduced by reducing the sampling effort without significantly increasing the statistical uncertainty.

For these reasons as well as other considerations described in Section 1.2—namely MC methods are very efficient due to importance sampling [51], can capture discontinuities in the distribution function naturally and accurately [7, 52, 5], and they are conceptually simple and easy to code, lending themselves particularly well to simula-

tion of complex geometries—the focus of this chapter and the primary contribution of this work is an efficient Monte Carlo method for simulating the ab initio phonon Boltzmann equation via the splitting algorithm discussed in the previous chapter (see for example Section 5.5). Our method is distinguished from prior iterative ab initio simulations [87, 88, 71, 113, 77] by its ability to resolve spatially and time dependent problems, which is accomplished efficiently using a low variance deviational simulation Monte Carlo formulation [52]. At the same time, this work is distinguished from previous phonon Monte Carlo simulations which were limited by the SMRT approximation [96, 49, 90, 67, 93]. Remarkably, the scattering step integration developed in Section 5.5 introduces no time step error and will be shown to improve the computational cost scaling compared to the iterative method and the deterministic (i.e. Euler) method of Section 5.6, albeit at the relatively minor cost of matrix sparsity loss and stochastic noise.

We will refer to our method as linearized ab initio phonon low variance deviational Monte Carlo (LAIP-LVDSMC). The LAIP-LVDSMC algorithm is presented hereafter and summarized in Section 6.6.

## 6.1 Particle representation of the distribution function

The underlying principle for stochastic integration is to distribute computational particles as prescribed by the distribution function and then to evolve the position and wavevector of those particles according to the governing equation. Formally, the distribution function is approximated by a collection of $N_{\text{parts}}$ particles by writing

$$f_i^{\text{d}}(\boldsymbol{x}) = \sum_{j=1}^{N_{\text{parts}}} E_{\text{eff}} \sigma_j \delta_{\lambda_j,\lambda_i} \delta(\boldsymbol{x} - \boldsymbol{x}_j) \tag{6.1}$$

where $E_{\text{eff}}$ is the effective energy that each computational particle represents and $\sigma_j$ is the sign ($\pm 1$) of the particle. The particles are signed because this formulation is

deviational [7, 8, 52]—particles simulate the deviation from equilibrium. Equation (6.1) also reflects the fact that this work uses a discrete representation of the reciprocal space required by the scattering model, but a continuous representation of direct space.

In order to sample properties, the continuous spatial domain is divided into cells of volume $V_{\text{cell}} = A_{\text{cell}}\delta$; spatial variation in properties can be calculated in cell-averaged sense. For example, the energy density in a cell of volume $V_{\text{cell}}$ is

$$u_m = \frac{\sum_{\{j|\boldsymbol{x}_j \in \text{cell } m\}} E_{\text{eff}}\sigma_j}{V_{\text{cell}}} + u_{\text{eq}}(T_0) \tag{6.2}$$

where $u_{\text{eq}}(T_0)$ is the energy density at the reference temperature $T_0$ calculated from (4.10). The heat flux is given by

$$\boldsymbol{J}_{E,m} = \frac{1}{V_{\text{cell}}} \sum_{\{j|\boldsymbol{x}_j \in \text{cell } m\}} E_{\text{eff}}\sigma_j \boldsymbol{v}_j \tag{6.3}$$

These estimators for the relevant cell properties, have been variance-reduced [7, 52] by separating out the equilibrium contribution to the estimator and adding that portion analytically. This strategy can significantly reduce stochastic noise and improve computational efficiency, particularly in small-driving force problems. Generation of computational particles that represent a given distribution function and their evolution in time will be described in the following sections.

## 6.2 Initialization and distribution function sampling

Initialization requires sampling particles from a prescribed distribution function. In practice, it is convenient to initialize a simulation from the reference equilibrium so that $f_i^{\text{d}} = 0$. In that case, no particles are required and the simulation is exact due to the analytic decomposition. Since it will be necessary to generate particles from non-uniform distributions during other stages of the simulation, we consider here, as

an example, initializing at $f^{\text{eq}}(\omega_i; T)$ leading to

$$f_i^{\text{d,init}}(T) = f^{\text{eq}}(\omega_i; T) - f^{\text{eq}}(\omega_i; T_0), \tag{6.4}$$

where $T_0$ is the reference equilibrium temperature and $T$ is the initial equilibrium temperature. The equilibrium distribution function is given by (5.5).

While more sophisticated methods for sampling a distribution function in the context of stochastic particle simulation of the Boltzmann equation have been developed [102], the most straight-forward is a simple acceptance-rejection scheme [12], which is discussed below.

### 6.2.1 Acceptance-rejection (A-R) algorithm

With the example of an initial distribution given by (6.4) and using the $N_{\text{states}}$ mesh points prescribed in Section 4.1, the acceptance rejection algorithm proceeds as follows:

1. Determine the number of particles to generate. Specifically for initialization according to (6.4) in a volume $V$, the number of particles and the effective energy are related by

$$N_{\text{parts}} = \frac{V f^{\text{d,abs}}}{E_{\text{eff}}} = \frac{\sum_i V |f_i^{\text{d,init}}(T)|}{E_{\text{eff}}}. \tag{6.5}$$

   When the simulation is initialized from the reference equilibrium ($f_i^{\text{d,init}} = 0$), the effective energy is determined by other considerations—for example, the number of particles desired to enter through the boundaries per time step (see Equation (6.11)) or the number of particles generated by a source term per time step (see Section 6.3.3).

2. Calculate the largest magnitude of the $f_i^{\text{d,init}}$ for any state $i$—$f^{\text{d,max}} = \max(|f_i^{\text{d,init}}(T)|)$.

3. Randomly select a mesh point $i$.

4. Draw a random number $\mathcal{R} \in [0,1)$; if $\frac{|f_i^{\mathrm{d,init}}(T)|}{f^{\mathrm{d,max}}} < \mathcal{R}$ keep the particle; otherwise, go back to 3.

5. Assign the particle the sign $\sigma = \mathrm{sgn}(f_i^{\mathrm{d,init}}(T))$.

6. Assign the particle a spatial location $\boldsymbol{x}$, typically chosen randomly and uniformly throughout the volume $V$.

7. Go back to 3 until the appropriate number of samples have been accepted.

## 6.3 Left hand side–Advection

The advection sub step simulates the left hand side of (5.11), which will be further separated into two parts. The first part

$$\frac{\partial f_i^{\mathrm{d}}}{\partial t} + \boldsymbol{v}_i \cdot \nabla_{\boldsymbol{x}} f_i^{\mathrm{d}} = 0$$

describes ballistic motion of the particles

$$\boldsymbol{x}_i(t + \Delta t) = \boldsymbol{x}_i(t) + \boldsymbol{v}_{x,i}(t)\Delta t. \tag{6.6}$$

Particles move ballistically until the end of the time step or encountering a boundary.

In this work, two types of boundaries will be considered, namely, prescribed temperature boundaries and diffusely reflecting adiabatic boundaries.

The second part of the advection sub step represents the effect of an imposed temperature gradient

$$\boldsymbol{v}_\lambda \cdot \left.\frac{\partial f^{\mathrm{eq}}(\omega_\lambda; T(\boldsymbol{x}))}{\partial T}\right|_{T_0} \nabla_{\boldsymbol{x}} T(\boldsymbol{x})$$

and will be treated as a source of particles [93].

### 6.3.1 Prescribed temperature boundaries

Prescribed temperature boundaries are primarily used to represent large heat sinks, so it is typically assumed that the phonons emitted from such a boundary will be

distributed according to an equilibrium distribution function. The net heat flux across a prescribed temperature boundary with inward normal (pointing into the material) $\hat{\boldsymbol{n}}_{\text{wall}}$ is given by

$$J_{E,\text{wall}} = \sum_{\{i|\boldsymbol{v}_i\cdot\hat{\boldsymbol{n}}_{\text{wall}}>0\}} \boldsymbol{v}_i\cdot\hat{\boldsymbol{n}}_{\text{wall}}\left(f^{\text{eq}}(\omega_i;T_{\text{wall}})\right) + \sum_{\{i|\boldsymbol{v}_i\cdot\hat{\boldsymbol{n}}_{\text{wall}}<0\}} \boldsymbol{v}_i\cdot\hat{\boldsymbol{n}}_{\text{wall}} f_i \tag{6.7}$$

Using the analytical decomposition (5.4), the flux is given by

$$\begin{aligned} J_{E,\text{wall}} = & \sum_{\{i|\boldsymbol{v}_i\cdot\hat{\boldsymbol{n}}_{\text{wall}}>0\}} \boldsymbol{v}_i\cdot\hat{\boldsymbol{n}}_{\text{wall}}\left(f^{\text{eq}}(\omega_i;T_{\text{wall}})\right) \\ & + \sum_{\{i|\boldsymbol{v}_i\cdot\hat{\boldsymbol{n}}_{\text{wall}}<0\}} \boldsymbol{v}_i\cdot\hat{\boldsymbol{n}}_{\text{wall}}(f_i^0 + f_i^{\text{d}}) \end{aligned} \tag{6.8}$$

If the boundary aligns with a reciprocal space symmetry plane then $\sum_{\{i|\boldsymbol{v}_i\cdot\hat{\boldsymbol{n}}_{\text{wall}}>0\}} f_i^0 = -\sum_{\{i|\boldsymbol{v}_i\cdot\hat{\boldsymbol{n}}_{\text{wall}}<0\}} f_i^0$, leading to the expression

$$\begin{aligned} J_{E,\text{wall}} = & \sum_{\{i|\boldsymbol{v}_i\cdot\hat{\boldsymbol{n}}_{\text{wall}}>0\}} \boldsymbol{v}_i\cdot\hat{\boldsymbol{n}}_{\text{wall}}\left(f^{\text{eq}}(\omega_i;T_{\text{wall}}) - f_i^0\right) \\ & + \sum_{\{i|\boldsymbol{v}_i\cdot\hat{\boldsymbol{n}}_{\text{wall}}<0\}} \boldsymbol{v}_i\cdot\hat{\boldsymbol{n}}_{\text{wall}} f_i^{\text{d}}. \end{aligned} \tag{6.9}$$

This mathematical expression makes clear how to implement prescribed temperature boundary conditions in a particle simulation. Particles of the simulation encounter the boundary proportional to $|\boldsymbol{v}_i\cdot\hat{\boldsymbol{n}}_{\text{wall}}|f_i^{\text{d}}$ and can be discarded (as seen by the fact that $\boldsymbol{v}_i\cdot\hat{\boldsymbol{n}}_{\text{wall}} < 0$ ). New particles must be introduced to represent

$$J_{\text{E,wall,in}} = \sum_{\{i|\boldsymbol{v}_i\cdot\hat{\boldsymbol{n}}_{\text{wall}}>0\}} \boldsymbol{v}_i\cdot\hat{\boldsymbol{n}}_{\text{wall}}\left(f^{\text{eq}}(\omega_i;T_{\text{wall}}) - f_i^0\right) \tag{6.10}$$

For a boundary segment of length $L_{\text{wall}}$ during a time step of length $\Delta t$, the total number of particles that must be generated is

$$N_{\text{parts,wall,in}} = \frac{L_{\text{wall}}\delta\Delta t}{E_{\text{eff}}} \sum_{\{i|\boldsymbol{v}_i\cdot\hat{\boldsymbol{n}}_{\text{wall}}>0\}} \left|\boldsymbol{v}_i\cdot\hat{\boldsymbol{n}}_{\text{wall}}\left(f^{\text{eq}}(\omega_i;T_{\text{wall}}) - f_i^0\right)\right| \tag{6.11}$$

Sampling from this distribution is accomplished with the acceptance-rejection procedure of Section 6.2.1, with Equation (6.4) being replaced by

$$f_i^{\mathrm{d,wall,in}} = \begin{cases} \boldsymbol{v}_i \cdot \hat{\boldsymbol{n}}_{\mathrm{wall}} \left( f^{\mathrm{eq}}(\omega_i; T_{\mathrm{wall}}) - f_i^0 \right) & \text{if } \boldsymbol{v}_i \cdot \hat{\boldsymbol{n}}_{\mathrm{wall}} > 0 \\ 0 & \text{otherwise} \end{cases} \tag{6.12}$$

and Equation (6.5) being replaced by (6.11) and particles being distributed uniformly along the boundary segment in time and space.

A special case of this boundary condition that is particularly easy to implement is when the wall temperature is chosen to be the reference equilibrium temperature $T_0$. In this case, the particles encountering the wall are destroyed and no additional particles need be generated.

### 6.3.2 Diffuse adiabatic walls

While diffuse and specular adiabatic walls are exceedingly simple to implement in a simulation with a continuous isotropic dispersion relation [96, 93], the anisotropic reciprocal space and its discretization significantly complicates matters. Re-emitting each particle that collides with a wall would likely require interpolation over many states to satisfy momentum and energy conservation. Instead, we will treat these boundaries in an average sense. Specifically, the particles encountering a boundary will be used to calculate the temperature of that boundary via inversion of (6.10). Then the boundary segment will be treated as a prescribed temperature wall at that calculated temperature for the current time step.

### 6.3.3 Source term for simulating a temperature gradient

The analytical decomposition (Equation (3.16)) allows for a spatially variable control temperature enabling the simulation of a temperature gradient via a source term without simulating the spatial dimension in which the gradient acts. For a temperature

gradient in the $x$ direction, the source term is given by

$$f_i^{\text{d,source}} = v_{x,i} \frac{\partial f^{\text{eq}}(\omega_i; T)}{\partial T} \frac{\mathrm{d}T}{\mathrm{d}x}. \tag{6.13}$$

Because of the symmetry inherent in the source term—specifically $f^{\text{d,source}}(q_x, q_y, s) = -f^{\text{d,source}}(-q_x, q_y, s)$, since $\omega(q_x, q_y, s) = \omega(-q_x, q_y, s)$ and $\boldsymbol{v}(q_x, q_y, s) = -\boldsymbol{v}(-q_x, q_y, s)$ due to the symmetry operators of Table 2.2—the source term is efficiently implemented using antithetic variates [91]. Specifically, although the number of particles to generate during a time step $\Delta t$ in a volume $V$ due to the source term is

$$N_i^{\text{parts,source}} = \frac{V \Delta t}{E_{\text{eff}}} \sum_i \left| v_{x,i} \frac{\partial f^{\text{eq}}(\omega_i; T)}{\partial T} \frac{\mathrm{d}T}{\mathrm{d}x} \right|, \tag{6.14}$$

only half of this number is drawn using the acceptance rejection technique discussed 6.2.1 (replacing (6.4) with (6.13) and with (6.5) being replaced by $N_i^{\text{parts,source}}/2$). These particles are uniformly spread through the volume and time step; also, for each particle $i$ (with wavevector $\boldsymbol{q}_i$), a new particle is created of opposite sign at the symmetrically equivalent state $\tilde{i}$ (with wavevector $(-q_{x,i}, q_{y,i})$). This ensures that the correct number of particles is generated and energy and momentum in the $y$ direction (the sum of state $i$ and $\tilde{i}$) are exactly zero. This antithetic variate approach virtually eliminates drift in properties resulting from random walks due to stochastic noise in sampling the source term.

This source term implementation was first presented in the context of SMRT approximation based Monte Carlo simulations [91] and is directly applicable in this context. We emphasize here that in the limit of an infinitely large simulation domain, this approach is an exact representation of a temperature gradient (i.e. it introduces no approximation), but this source term must be carefully evaluated when device structures are introduced.

## 6.4 Scattering operator

The scattering sub step must implement the homogeneous relaxation problem

$$\frac{\partial f_i^{\mathrm{d}}}{\partial t} = \sum_j B_{ij} f_j^{\mathrm{d}}. \tag{6.15}$$

With perhaps the exception of Ref. [48], to the author's knowledge, the relaxation problem using this linearized ab initio scattering operator has never been implemented in a particle simulation. Due to its low dimensionality graphene, is a computationally less computationally less demanding than three dimensional semi conductors, but the computation is still computational resource intense. The matrix representation of the scattering operator bears strong resemblance to Kinetic Monte Carlo and Continuous time Markov Chain simulations [68] and suggests possible numerical methods to efficiently simulate the scattering operator in a particle sense, but due to the analytical decomposition (Equation (3.16) in see Section 3.1.3), which makes these simulations possible, and due to the three state coupling inherent in the phonon scattering, there are significant differences from the established Markov Chain methods. Specifically, we recall that here, particles represent deviations from the equilibrium distribution function and hence can be positively or negatively signed; off diagonal elements of the transition matrix $B_{ij}$ can also be negative–for example, $B_{ij}$ can be negative if particles in state $j$ and state $i$ combine to make a phonon in some other state $k$.

In order to motivate the method for implementing this scattering operator in a particle simulation, first consider the following two state system for a single time step,

$$\begin{bmatrix} f_1^{\mathrm{d}}(t+\Delta t) \\ f_2^{\mathrm{d}}(t+\Delta t) \end{bmatrix} = \begin{bmatrix} \alpha & \gamma \\ \beta & \delta \end{bmatrix} \begin{bmatrix} f_1^{\mathrm{d}}(t) \\ f_2^{\mathrm{d}}(t) \end{bmatrix},$$

where due to energy conservation

$$\alpha + \beta = 1, \quad \text{and} \quad \gamma + \delta = 1.$$

A naive algorithm for simulating the transition of particles that exist in state 1 would

be to leave a particle in state 1 with probability $\alpha$ and move it to state 2 with probability $\beta$. However, it is not immediately clear what to do if $\alpha$ or $\beta$ are negative or greater than one.

To be specific, the system of ODEs representing phonon scattering (5.9) has two significant differences from the continuous time Markov chain problems that affect the resulting particle simulation:

1. The distribution $f_i^{\mathrm{d}}$ can take positive or negative values (since it represents a deviational quantity).

2. The elements of propagator, $P_{ij}$, can be negative (a consequence of having negative off diagonal elements $B_{ij}$ due to three phonon coupling).

The first issue is easily remedied by recognizing that (5.37) is linear in $f_i^{\mathrm{d}}$, so that the dynamics of positive and negative distributions (or particles) are identical. A dilemma similar to the second issue has been addressed in [7] which renormalizes transition rates by the sum of their absolute values. However, this does not preserve exactly the dynamics of the system, and will require a correction—which here is implemented as a source of computational particles.

To derive the dynamics of particle state transitions and particle generation, we first recognize that the sum of the absolute values of a column of the generator matrix will be greater than 1

$$\sum_k |P_{kj}(\Delta t)| = 1 + 2 \sum_{k|P_{kj}(\Delta t)<0} |P_{kj}(\Delta t)|. \tag{6.16}$$

To simplify the notation we define a column normalization

$$\mathcal{P}_j = \sum_k |P_{kj}(\Delta t)| \tag{6.17}$$

while the sum of all of the negative elements of the column is denoted by

$$\mathcal{P}_j^- = \sum_{k|P_{kj}<0} |P_{kj}(\Delta t)| \tag{6.18}$$

such that the normalization is equal to unity plus twice the magnitude of the sum of the negative elements

$$\mathcal{P}_j = 1 + 2\mathcal{P}_j^- . \tag{6.19}$$

Now considering (5.37) element wise and using the convenient trick of multiplying by a clever form of $1 = \frac{\mathcal{P}_j}{\mathcal{P}_j}$, the integrator step can be written as

$$\begin{aligned} f_i(t+\Delta t) &= \sum_j P_{ij}(\Delta t) f_j(t) \\ f_i(t+\Delta t) &= \sum_j \frac{P_{ij}(\Delta t)}{\mathcal{P}_j} \mathcal{P}_j f_j(t) \\ f_i(t+\Delta t) &= \sum_j \frac{P_{ij}(\Delta t)}{\mathcal{P}_j} \left(1 + 2\mathcal{P}_j^-\right) f_j(t). \end{aligned} \tag{6.20}$$

The first part of the latter expression is easy to interpret in a particle sense—with probability $\frac{|P_{ij}(\Delta t)|}{\mathcal{P}_j}$ a particle in state $j$ moves to state $i$ and if $P_{ij}(\Delta t) < 0$, its transition is accompanied by a sign change. The second part is more complicated, but can be simplified using the same trick as before

$$\begin{aligned} f_i(t+\Delta t) &= \sum_j \frac{P_{ij}(\Delta t)}{\mathcal{P}_j} \left(1 + \frac{2\mathcal{P}_j^-}{\mathcal{P}_j} \mathcal{P}_j\right) f_j(t) \\ f_i(t+\Delta t) &= \sum_j \frac{P_{ij}(\Delta t)}{\mathcal{P}_j} \left(1 + \frac{2\mathcal{P}_j^-}{\mathcal{P}_j} \left(1 + 2\mathcal{P}_j^-\right)\right) f_j(t) \\ f_i(t+\Delta t) &= \sum_j \frac{P_{ij}(\Delta t)}{\mathcal{P}_j} \left(\sum_{n=0}^{\infty} \left(2\frac{\mathcal{P}_j^-}{\mathcal{P}_j}\right)^n\right) f_j(t) \end{aligned} \tag{6.21}$$

This recursive formula can be implemented as a follows: particles representing $f_j(t)$, transition to state $i$ with probability $\frac{P_{ij}(\Delta t)}{\mathcal{P}_j}$ and with probability $\frac{\mathcal{P}_j^-}{\mathcal{P}_j}$ two new particles are generated in state $j$ existing at time $t$ (i.e. needing to be transitioned to time $t + \Delta t$). We note that these two new particles are generated at the same rate at which particles experience a sign change due to negative propagator elements $P_{ij}$.

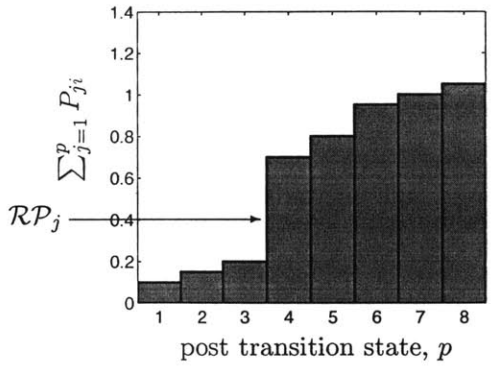


Figure 6-1: Schematic representing selection of the post scattering state. In this figure, the quantity $\mathcal{RP}_j$ has a value of 0.4 which indicates the post scattering state should be state $p = 4$. The selection of the post scattering state can be accomplished in $\mathcal{O}(\log(N_{\text{states}}))$ time using a binary search algorithm.

This connection between sign change and particle generation will allow us to develop a particle method that exactly conserves energy during the homogeneous relaxation sub step.

### 6.4.1 Scattering sub step algorithm

Given a particle in state $i$ with sign $\sigma$, let $\mathcal{P}_i = \sum_{j=1}^{N_{\text{states}}} |P_{ji}|$

1. Transition the particle from state $i$ to the state $p$ where

$$\sum_{j=1}^{p-1} |P_{ji}| \leq \mathcal{RP}_i < \sum_{j=1}^{p} |P_{ji}|.$$

2. Assign a new sign to the particle $\sigma' = \text{sgn}(P_{pi}\sigma)$.

3. If $\sigma' \neq \sigma$, generate 2 more particles at i, $\sigma$ and go back to 1 for each

This scheme has the convenient feature of exactly conserving energy during the scattering evaluation and using a binary search algorithm to identify the state to which a particle transfers, can be implemented in $O(\log(N_{\text{states}}))$ operations—as opposed to the deterministic approach which would scale as $O((N_{\text{states}}))$.

## 6.5 Particle cancellation

Due to particle generation in the scattering term and also in the source and boundary terms, the number of particles in the simulation can grow unmanageably large. This growth is controlled by deleting particles at the boundary, but for large systems, this sink is insufficient to maintain stability. As an alternative, particles that reside in the same spatial cell and at the same reciprocal space bin, but that have opposite signs can be cancelled. This is accomplished with a sorting algorithm that counts the net sign in each bin and then randomly selects which pairs of particles can be deleted. For large simulation domains ($L \gg \Lambda$), this cancelation routine tends to accelerate the computational speed, whereas for very small domains ($L \ll \Lambda$) where stability is not an issue, it slows down the calculations [8]. The frequency of the cancellation can be adjusted accordingly.

## 6.6 LAIP-LVDSMC algorithm

In summary, the resulting algorithm is as follows:

1. **Initialize**

   (a) Choose $E_{\text{eff}}$, the effective energy each particle will represent either based on the initial condition, the boundary condition, or the source term.

   (b) Distribute the particles according to the initial condition. Specifically, for each particle $i$ draw a uniform random variate $\mathcal{R} \in [0, 1)$ and assign the particle to state $j$ such that

   $$\sum_{i=1}^{j-1} |f_i(0)|/E^{\text{abs,d}} \leq \mathcal{R} < \sum_{i=1}^{j} |f_i(0)|/E^{\text{abs,d}}.$$

   Store the state for the $i$th particle $s_i(t=0) = j$ and also store the sign of the particle $\sigma_i(t=0) = \text{sgn}(f_j(t=0))$

2. **Advect**

(a) Move particles ballistically until encountering a boundary or the end of the time step

(b) Track particles encountering each boundary

(c) Calculate the temperature of each boundary and insert new particles as appropriate (allowing those particles to also advect until the end of the time step.

(d) If applicable, draw the appropriate number of particles for the homogenous source term.

3. **Collision/Homogenous relaxation**

(a) Calculate the generator from

$$\boldsymbol{P}(\Delta t) = \sum_{k=0}^{\infty} \frac{(\Delta t)^k}{k!} \boldsymbol{B}^k,$$

where we briefly violate our index-based notation convention for the transition matrix and propagator in order to succinctly express the matrix exponentiation. This step is typically done before starting the time integration and then stored to the disk for future use.

(b) Define a normalization for each generator column

$$\mathcal{P}_j = \sum_{q=1}^{N_{\text{states}}} |P_{qj}|$$

(c) For each time step of interest and for each particle $i$ in state $s_i = j$, draw a random number and transition a particle from state $j$ to the state $p$ where

$$\sum_{q=1}^{p-1} |P_{qj}|/\mathcal{P}_j \leq \mathcal{R} < \sum_{q=1}^{p} |P_{qj}|/\mathcal{P}_j.$$

Store the new state $s_i(t + \Delta t) = p$. Assign a new sign to the particle $\sigma_i(t+\Delta t) = \text{sgn}(P_{pj}(\Delta t))\sigma_i(t)$. If there is a sign change, this step effectively

deletes a particle of sign $\sigma_i(t)$ in addition to generating a new particle with sign $-\sigma_i(t)$, for a net change of energy of the system of $-2E_{\text{eff}}\sigma_i(t)$, this is balanced by the next step.

(d) If a particle $i$ experiences a sign change during transition from $\sigma_i(t)$ to $\sigma_i(t+\Delta t)$, generate two new particles of sign $\sigma_i(t)$, and process them for transition in an identical manner. Specifically, if the selected post transition state for a newly generated particle also changes the particles sign, then generate two additional new particles in state $j$ with sign $\sigma_i(t)$, and so on.

4. **Sample**

(a) The time history of the macroscopic observables can be calculated by summing over the particles at time $t$ times their sign in each spatial cell. For example, if the particles in a cell $m$ with volume $V_{\text{cell}}$ reside in states $s_i(t) = j$ and those states have associated velocities $\boldsymbol{v}_j$, then the energy flux would be

$$\boldsymbol{J}_{E,m}(t) = \frac{E_{\text{eff}}}{V_{\text{cell}}} \sum_{i=1}^{N_{\text{part}}} \sigma_i(t) \boldsymbol{v}_{s_i(t)}.$$

## 6.7 Validation

Neither analytical nor numerical non-trivial solutions of the ab initio phonon Boltzmann transport equation with spatial and time dependence are available, so we present two partial validation problems: a homogenous "thermal conductivity measurement problem" and an infinitely long 2D ribbon under the SMRT approximation. The former will be compared with the solution from the iterative method and a deterministic scheme we developed for the same; the latter will be compared to the analytical solution we recently reported [67] and present hereafter.

### 6.7.1 Homogeneous validation

The steady state solution of a spatially homogenous problem subject to the source term

$$\cancelto{0}{\frac{\partial f_i^{\mathrm{d}}(t)}{\partial t}} + v_i \cdot \cancelto{0}{\nabla_x f_i^{\mathrm{d}}(t)} + v_{x,i} \left.\frac{\partial f^{\mathrm{eq}}(\omega_i;T)}{\partial T}\right|_{T_0} \frac{\mathrm{d}T}{\mathrm{d}x} = \sum_j B_{ij} f_j^{\mathrm{d}}(t=\infty). \tag{6.22}$$

can be efficiently calculated using the iterative method discussed in the preceding chapters. We also note that in the time dependent spatially homogeneous case (Equation (5.40)), the deterministic scheme presented in Section 5.6 is relatively straightforward—the difficulties associated with the deterministic approach tend to arise in the advection routine, which in a homogeneous problem is unnecessary. Hence in order to demonstrate the correct time-dependent behavior (as prescribed by (5.40)) and steady state averages, the heat flux of a homogeneous system subject to a temperature gradient is calculated using the deterministic, time-dependent Euler-based scheme of Section 5.6 and the LAIP-LVDSMC method.

Figure 6-2 shows that the LAIP-LVDSMC solution reproduces the time history of the heat flux as provided by an Euler-type integrator. In this figure, the heat flux is normalized by the steady state solution from the iterative method. The difference between the deterministic solution and the LAIP-LVDSMC solution is less than 1% and is due to stochastic noise. After 20000 transient simulation steps of 1 ps and averaging over 20000 steady state steps, the discrepancy between the LAIP-LVDSMC and the iterative solution is 0.06% (not shown on the figure). These results validate the time-dependent integration aspect of the LAIP-LVDSMC simulation. The parameters used for these simulations are listed in Table B.1 and a discussion of how they may be appropriately determined appears in Section 6.8.

### 6.7.2 Infinitely long 2D ribbon under SMRT approximation

While this work and others [71, 112] have shown that the SMRT is not appropriate for thermal transport in graphene, its simplicity makes it attractive as an approximate

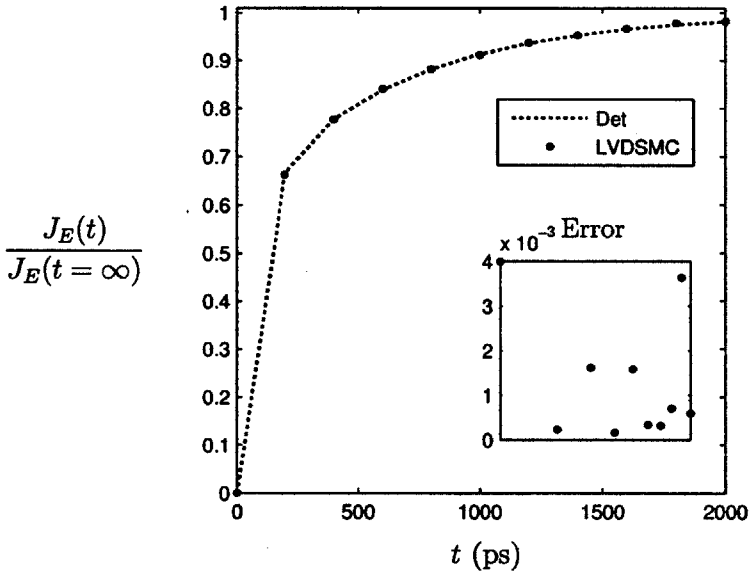


Figure 6-2: Validation of a homogenous time dependent LAIP-LVDSMC simulation with a deterministic scheme. Both converge towards the iterative solution of $J_E(t = \infty)$.

model. As we show below, the SMRT model can be used for validating part of our LVDSMC implementation.

Under the SMRT approximation, the RHS of (5.11) can be replaced with

$$\left[\frac{\partial f_i^{\mathrm{d}}(\boldsymbol{x},t)}{\partial t}\right]_{\mathrm{scatt}} = B_{ii} f_i^{\mathrm{d}}(\boldsymbol{x},t) = -\frac{f_i^{\mathrm{d}}(\boldsymbol{x},t)}{\tau_i}, \tag{6.23}$$

where, due to symmetry, we have assumed that the local equilibrium distribution everywhere is $f_i^0$. This simple scattering model permits closed form evaluation of the distribution function (see Equation (4.2)), and the heat flux in a *homogeneous* volume $V$ with a one dimensional temperature gradient ($\mathrm{d}T/\mathrm{d}x$) is

$$J_{E,\mathrm{homo,SMRT}} = -\frac{1}{V}\sum_{i=1}^{N_{\mathrm{states}}} v_{i,x}^2 \frac{\mathrm{d}T}{\mathrm{d}x}\tau_i \left.\frac{\partial f^{\mathrm{eq}}(\omega_i;T)}{\partial T}\right|_{T_0}, \tag{6.24}$$

where $\tau_i = B_{ii}^{-1}$, $f^{\mathrm{eq}}$ is given by Equation (5.5), and for simplicity we only consider the heat flux in the direction of the temperature gradient.

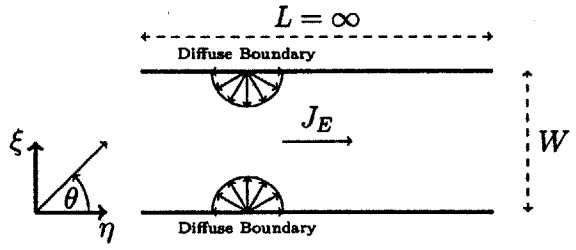


Figure 6-3: Schematic of an infinitely long graphene ribbon with diffuse boundaries which is subject to a temperature gradient (not shown).

In order to implement the SMRT approximation in the LVDSMC framework, the scattering step of Section 6.4 is replaced with the following, *considerably simpler* procedure:

- For a particle in state $i$, draw a uniform random variate $\mathcal{R}$.
- If $\mathcal{R} < 1 - \exp(B_{ii}\Delta t)$, discard the particle; otherwise retain the particle.

This simple procedure implements the scattering model as described above, but does not strictly conserve energy. For details on the correct energy conserving algorithm as well as more efficient SMRT algorithms see [65, 49, 91, 67, 93]. The simulations employing this scattering procedure will be referred to as SMRT-LVDSMC.

### Analytical Solution for the effective conductivity of long ribbons

Thin films under the action of a constant temperature gradient are sufficiently simple to admit analytical solutions under the SMRT. The exact solution for a three-dimensional thin film with diffuse boundaries can be found in various sources [124, 27, 91]. Although the extension of that solution to two-dimensions is straightforward, prior to our recent work [67], it appears to have not yet been applied to transport in two-dimensional ribbons.

For the ribbon geometry shown in Figure 6-3, the Boltzmann equation under the

SMRT approximation in steady state can be written as

$$\cancelto{0}{\frac{\partial f_i^{\mathrm{d}}(\xi)}{\partial t}} + \boldsymbol{v}_i \cdot \nabla_{\boldsymbol{x}} f_i^{\mathrm{d}}(\xi) + \boldsymbol{v}_i \cdot \nabla_{\boldsymbol{x}} T(\boldsymbol{x}) \left.\frac{\partial f^{\mathrm{eq}}(\omega_i; T(\boldsymbol{x}))}{\partial T}\right|_{T_0} = -\frac{f_i^{\mathrm{d}}(\xi)}{\tau_i}. \tag{6.25}$$

The boundary conditions can be set as $f_i^{\mathrm{d}}(\xi = 0) = f_i^{\mathrm{d}}(\xi = 1) = 0$, following the observation [124] that for this problem, diffuse boundaries can be modeled using this boundary condition, which leads to the solution

$$f_i^{\mathrm{d}}(\xi) = \begin{cases} f_i^{\mathrm{d,SMRT}}\left(1 - \exp\left(-\frac{\xi}{Kn_{i,W}\sin(\theta_i)}\right)\right) & 0 \le \theta_i < \pi \\ f_i^{\mathrm{d,SMRT}}\left(1 - \exp\left(-\frac{\xi - 1}{Kn_{i,W}\sin(\theta_i)}\right)\right) & \pi \le \theta_i < 2\pi \end{cases} \tag{6.26}$$

where the mode specific Knudsen number is given by

$$Kn_{i,W} = \frac{||\boldsymbol{v}_i||\tau_i}{W}. \tag{6.27}$$

Here, the angle $\theta_i$ is measured between the wavevector and the $\eta$ axis as shown in Figure 6-3, and the distribution function in the homogeneous system with the single mode relaxation time is given by

$$f_i^{\mathrm{d,SMRT}} = -\tau_i \boldsymbol{v}_i \cdot \nabla_{\boldsymbol{x}} T(\boldsymbol{x}) \left.\frac{\partial f^{\mathrm{eq}}(\omega_i; T)}{\partial T}\right|_{T_0}. \tag{6.28}$$

From (5.8), the exact solution for the width-averaged heat flux for a ribbon of volume $LW\delta$ is

$$\boldsymbol{J}_{E,\mathrm{avg,SMRT}}(W) = \frac{1}{LW\delta} \int_0^1 \mathrm{d}\xi \sum_{i=1}^{N_{\mathrm{states}}} \boldsymbol{v}_{i,x} f_i^{\mathrm{d}}(\xi) \tag{6.29}$$

which is easily integrated to give

$$\begin{aligned} \boldsymbol{J}_{E,\mathrm{avg,SMRT}}(W) \;=\; & \sum_{i=1}^{N_{\mathrm{states}}} \boldsymbol{v}_i f_i^{\mathrm{d,SMRT}} \\ & \times \left(1 - Kn_{i,W}|\sin(\theta_i)|\left(1 - \exp\left(-\frac{1}{Kn_{i,W}|\sin(\theta_i)|}\right)\right)\right). \end{aligned} \tag{6.30}$$

Although heat flux is a vector, in this section we will only consider the heat flux in the direction of the applied temperature gradient $J_{E,\text{avg,SMRT}}(W)$. This heat flux expression is analytic in terms of the spatial integration, but must still be evaluated using the reciprocal space discretization.

Figure 6-4 shows a comparison between the prediction of the Equation (6.30) and spatially-dependent SMRT-LVDSMC simulations of the same problem. As expected, the analytical solution and the SMRT-LVDSMC solution are in essentially perfect agreement (less than 1% discrepancy). A comparison of heat flux profiles for various ribbon widths is also shown in Figure 6-5. The error present is due to the finite discretization of the LVDSMC simulation which can be further reduced as will be discussed in Section 6.8. Simulation parameters are given in Table B.2. These results serve as a validation of the advection part of the present implementation of the LVDSMC method.

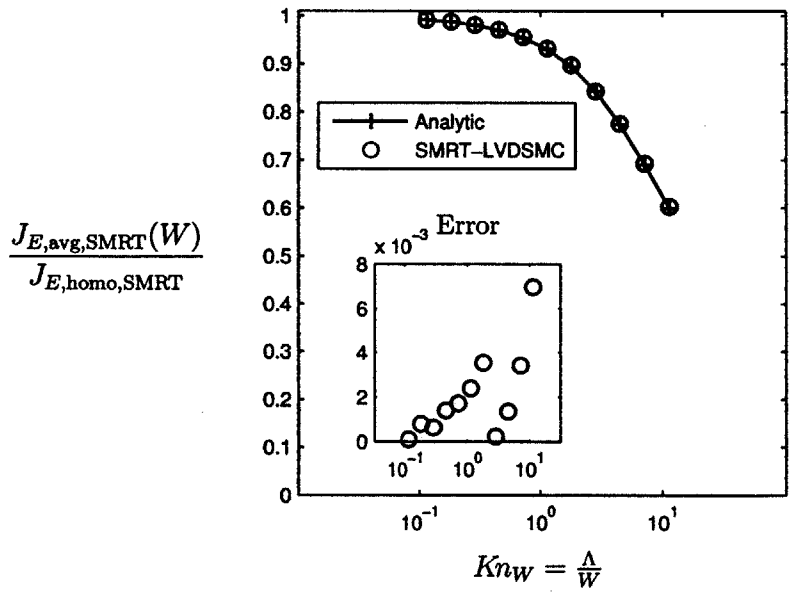


Figure 6-4: Effective thermal conductivity of infinitely long graphene ribbon with diffusely reflecting boundaries under the SMRT approximation as calculated by SMRT-LVDSMC and the analytical solution (6.30). The error of the SMRT-LVDSMC calculation from the analytical solution (inset) is calculated assuming the analytic result is exact.

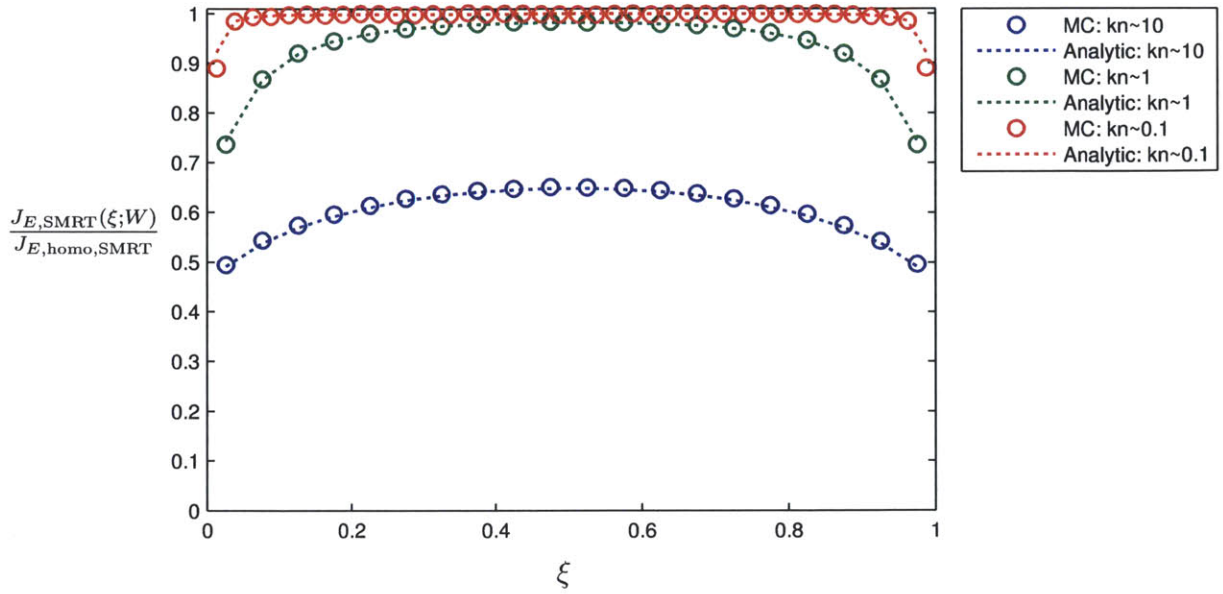


Figure 6-5: Heat flux profile across infinitely long graphene ribbons of various widths. Comparison between the analytical solution (dashed lines) from Equation (6.26) and the SMRT-LVDSMC simulation (circles).

## 6.8 Simulation parameters and error

The stochastic particle method as described above includes four types of discretization: reciprocal space is discretized into states, real space is subdivided into cells in which the distribution is treated as homogeneous during cancellation, time is advanced in discrete steps, and the distribution function is discretized into computational particles. Each of these discretizations is expected to introduce its own discretization error and to be interrelated with the others [101] making it difficult to analyze or theoretically predict the convergence of each. However we note that, in the context of DSMC, rigorous proof of the convergence of most of these types of discretization exists [104, 120].

A one dimensional simulation for a given type of boundaries is completely specified by the parameters in Table 6.1. The first three parameters specify the problem: temperature, temperature gradient, and length scale. The next four specify the discretization: reciprocal space, time, particles, and direct space. The frequency of the

cancellation routine allows the user to tune the simulation for more stability (more frequent cancellation) at the cost of potentially more spatial discretization error—pairs of particles for cancellation are selected from within a spatial cell. For steady state averaging, it is important to run the simulation past the transient behavior. The number of transient timesteps controls the onset of steady state averaging.

Transport properties calculated by averaging are expected to suffer from statistical uncertainty due to finite sampling; according to the central limit theorem, the uncertainty is inversely proportional to the square root of the number of *independent* samples. For dilute gases and fluids, Hadjiconstantinou *et al.* [45] showed that explicit expressions for the statistical uncertainty can be developed for all physical properties of interest using statistical mechanics. The use of equilibrium statistical mechanics is justified when characteristic temperature changes are small (e.g. compared to the absolute reference temperature) as is typical in micro-scale applications [44]. These results were validated by DSMC and molecular dynamics simulations in [45]. Theoretical description of fluctuations for a simplified representation of phonon MC simulations is presented [93]. The last two parameters in Table 6.1 are used to control stochastic noise: number of steady state time steps and number of ensembles. The latter providing independent samples while the steady state samples may have some time correlation.

Table 6.1: Legend of abbreviations for input parameters for 1D simulation.

| Abbreviation | Description |
|---|---|
| T0 | Reference temperature $T_0$ |
| TG | Temperature gradient in K/m |
| LS | Simulation length scale (e.g. width, length, or diameter) |
| NS | Reciprocal space discretization $N_{\text{side}}$ |
| DT | Timestep $\Delta t$ in picoseconds |
| PT | Particles generated per time step (advection) |
| NC | Number of spatial cells along simulation domain |
| CF | Frequency of cancellation routine |
| TS | Number of transient timesteps |
| SS | Number of steady timesteps |
| NE | Number of ensembles |

Due to the finite computational resources at out disposal it is essential to find a

balance between computational cost and error (discretization error, stochastic error, or error from including transient effects in a steady state average). As a general rule of thumb used in DSMC simulations of rarefied gases [12], the discretization error is reduced to appropriate levels by choosing the number of particles per cell to be greater than 20, the spatial discretization to be less than one third of the mean free path [3, 43], and the time step to be less than one third the scattering time scale $\Delta t < \bar{\tau}/3$ [43] as well as less than the cell traversal time $\Delta t < \frac{\tau_{\text{cell}}}{3}$. For our purposes we will use an average scattering time defined in analogy to the mean free path as

$$\bar{\tau} = \frac{\int \mathrm{d}^2\boldsymbol{q} \sum_s \tau(\boldsymbol{q}s) n^{\text{eq}}(\omega(\boldsymbol{q}s); T))}{\int \mathrm{d}^2\boldsymbol{q} \sum_s n^{\text{eq}}(\omega(\boldsymbol{q}s); T)} \tag{6.31}$$

and the cell traversal time is defined as

$$\tau_{\text{cell}} = \frac{1}{v_{\text{rms}}} \min\left(\Delta x, \Delta y\right). \tag{6.32}$$

with the root mean square velocity being calculated from the equilibrium distribution

$$v_{\text{rms}}^2 = \frac{\sum_i ||\boldsymbol{v}_i||^2 f_i^0}{\sum_i f_i^0}. \tag{6.33}$$

Compliance with these rules can be verified by the dimensionless numbers listed in Table 6.2. Also shown is the length of the transient normalized by the average scattering timescale, $\bar{\tau}$ and the ballistic or advective timescale

$$\tau_{\text{advect}} = \frac{\text{LS}}{v_{\text{rms}}} \tag{6.34}$$

For the homogeneous $Kn = 0$ problem of Figure 6-2, the system was within 5% of steady state by $\sim 100\bar{\tau}$ and (although not shown on the figure) was within 0.05% of steady state by $180\bar{\tau}$. For spatially dependent, low Knudsen number problems, the length of the transient will also be determined by the diffusive timescale, which is proportional to $L^2/\alpha \propto Kn^{-2}$, where $\alpha \propto \Lambda^2$ is the thermal diffusivity. For high Knudsen number problems, the length of the transient will depend upon the advective

time scale. A ballistic transient should be expected to last $100\tau_{\text{advect}}$ to allow the slowest particles to traverse the domain.

The computational time per timestep for a single ensemble (CM) will be used to evaluate the cost of the discretization.

Table 6.2: Legend of abbreviations for derived parameters.

| Abbreviation | Description |
|---|---|
| PC | Number of particles per reciprocal space cell per spatial cell |
| LC | Length of cell over mean free path |
| TM | Timestep normalized by mean scattering time, $\Delta t/\bar{\tau}$ |
| TC | Timestep normalized by minimum cell traversal time, $\Delta t/\tau_{\text{cell}}$ |
| KN | Knudsen number |
| TT | Length of transient normalized by mean free time |
| TB | Length of transient normalized by ballistic time scale |
| CM | Computational time per timestep per MC ensemble |

These rules of thumb for time, particle, and spatial discretizations will be briefly investigated hereafter as well as the length of transient effects and strength of stochastic noise. The convergence due to reciprocal space discretization has already been treated in Section 4.7.

### 6.8.1 Timestep error convergence

The propagator formulation described in Section 5.5 introduces no timestep error. However, splitting the advection and the collision steps introduces its own time step error. In the naive implementation (i.e. advect for time step of length $\Delta t$, then process collision effects for a time step of length $\Delta t$), the error is expected to scale proportionally to the timestep [43]. This first order scaling can generally be improved to second order using a symmetrized algorithm [116]. The second order convergence of timestep discretization error has been extensively validated in DSMC [3, 4, 43, 38, 101]. In this work we are only able to achieve second order scaling for homogenous problems; we report our progress below. Additionally, we detail the error associated with a first order approximation of the propagator that can preserve the sparsity of the matrix.

The Strang method to achieve second order convergence [116] amounts to splitting the LHS update into two half steps symmetrically. For a spatially homogenous problem (i.e. Equation (5.40)) this corresponds to

$$f_i^{\mathrm{d,s}}(t+\Delta t) = f_i^{\mathrm{d}}(t) - \frac{\Delta t}{2} v_{x,\lambda} \left.\frac{\partial f^{\mathrm{eq}}(\omega_i;T)}{\partial T}\right|_{T_0} \frac{\mathrm{d}T}{\mathrm{d}x}, \tag{6.35}$$

followed by the RHS update

$$f_i^{\mathrm{d,c}}(t+\Delta t) = \sum_j P_{ij}(\Delta t) f_i^{\mathrm{d,s}}(t+\Delta t), \tag{6.36}$$

followed by an additional half LHS step

$$f_i^{\mathrm{d}}(t+\Delta t) = f_i^{\mathrm{d,c}}(t+\Delta t) - \frac{\Delta t}{2} v_{x,\lambda} \left.\frac{\partial f^{\mathrm{eq}}(\omega_i;T)}{\partial T}\right|_{T_0} \frac{\mathrm{d}T}{\mathrm{d}x}. \tag{6.37}$$

Figure 6-6 compares the thermal conductivity predicted by the iterative solution with the thermal conductivity calculated by a symmetrized and unsymmetrized time-splitting algorithm. The latter two solutions are calculated using the deterministic forward Euler scheme introduced in Section 5.6. The deterministic solver is more efficient in this case because we desire low-noise results for the thermal conductivity (always a challenge with an MC method) while coarse discretizations of reciprocal space are acceptable for showing the convergence of the error introduced by the splitting scheme as long as all runs use the same discretization. All simulations were run with $N_{\mathrm{side}} = 11$ up to a simulation time of 20 ns, which should effectively eliminate transient behavior. As expected, the symmetrized version converges more rapidly than the unsymmetrized algorithm.

One drawback associated with use of the propagator for time stepping is that the propagator, $P_{ij}$, does not preserve the sparsity of the transition matrix, $B_{ij}$. The loss of sparsity may become computationally limiting for finer discretizations particularly in terms of memory requirements. As an alternative, the first order approximation for the propagator,

$$P_{ij}(\Delta t) \approx 1 + B_{ij}\Delta t, \tag{6.38}$$

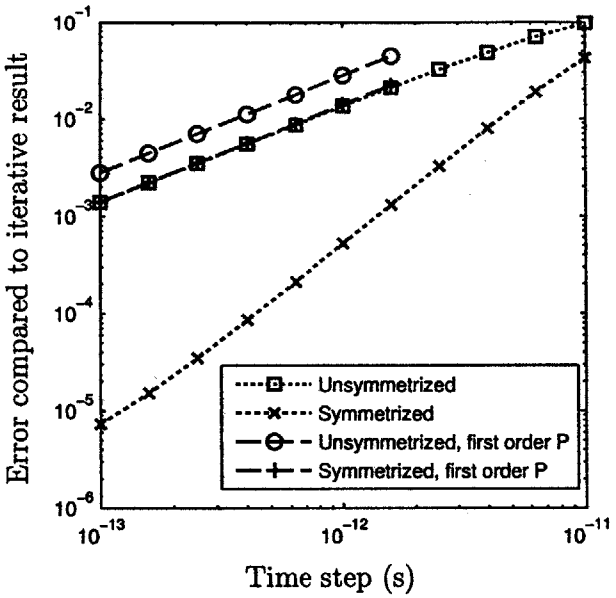


Figure 6-6: The symmetrized time splitting algorithm improves the convergence rate of time step error due to the splitting scheme. Using a sparsity preserving approximation for the propagator is shown to undo this increased convergence rate.

(which preserves the sparsity) can be used. The error associated with this first order approximation for $P_{ij}$ (also shown in Figure 6-6 as evaluated with the Euler deterministic scheme) is higher than that introduced by the time splitting and, as expected, is first order convergent even when symmetrized. Furthermore, for timesteps of length $\Delta t = 3$ps and larger, the first order approximation causes the simulation to become unstable. This is one drawback of using a deterministic scheme, that may not be an issue for a stochastic particle method. Due to the shorter timesteps that would be required to achieve a desired level of accuracy, the first order approximation for $P_{ij}$ is only recommended when memory requirements become limiting.

For the homogeneous problem above, only the source term needed to be split to symmetrize the algorithm—there was no need to advect particles and the cancellation routine introduced no error. For spatially dependent problems, the free flight of the particles and the particle cancellation routine must also be symmetrized.

### 6.8.2 Cancellation routine error

In DSMC, which provided the rule of thumb estimates for controlling discretization error (See Section 6.8), scattering is modeled by selecting pairs of particles within a spatial cell and processing a collision between them. Clearly particles separated by a finite distance cannot interact, leading to spatial error. Furthermore, under-sampling of the distribution function with a finite number of particles can lead to biases in the scattering, which introduces error based on the number of particles per cell. In our LAIP-LVDSMC method, scattering is treated exactly using the propagator matrix and is expected to introduce no discretization error. Nevertheless, our scattering routine generates additional particles which may need to be controlled using the cancellation routine of Section 6.5. It appears that dependence upon number of particles and spatial discretization enters LAIP-LVDSMC only through the cancellation routine.

As an example of the error that particle cancellation may introduce, consider particles generated at a prescribed temperature boundary which, after one timestep advect only a short distance into the simulation domain. If the spatial cell is large compared to the mean free path of the particle, then cancellation may occur between a particle near the boundary and one further away from it which significantly speeds the advection of energy from a wall into the domain.

In practice, we have not observed a discretization error in LAIP-LVDSMC based on the number of particles per cell. This may be due to the fact that this simulation is adaptive in the following sense: when the number of particles per spatial cell is small, cancellation will occur less frequently. This means that in practice the number of particles in a cell will grow (due to the scattering step generation) until the number of particles is sufficient for cancellation to occur. Thus, the number of particles in the simulation will automatically become approximately proportional to the number spatial cells times the number of reciprocal space states. A more rigorous analysis of this relationship should be performed in the future.

Here we also note that a small number of particles (i.e. less than 10) drawn in

a timestep for the advection source terms—particularly if not using the antithetic variates approach described in Section 6.3.3—may lead to random walks in property estimators. Above the threshold of 10 particles per timestep, the only discretization error observed in this work dependent on the number of particles is related to the cancellation routine as described above.

## 6.9 Reciprocal space discretization and time scaling

The convergence of thermal conductivity versus the reciprocal space discretization has already been investigated in this work; it was concluded that the thermal conductivity tends to converge to within a few percent for discretizations $N_{\text{side}} = 81$ in the absence of boundary scattering. While finer discretizations would be desirable, the discretization of reciprocal space must be considered in light of the computational requirements.

The simplest iterative and deterministic solutions require $\mathcal{O}(N_{\text{states}}) = \mathcal{O}(N_{\text{side}}^2)$ operations to compute per time step for a single state (e.g. the summation on the RHS of Equation (5.40)). The overall scaling of these algorithms is therefore $\mathcal{O}(N_{\text{states}}^2) = \mathcal{O}(N_{\text{side}}^4)$ per timestep per spatial cell. Without reformulating the solution, the sparseness of the transition matrix can be exploited to reduce the scaling to $\sim \mathcal{O}(N_{\text{states}}^{3/2}) = \mathcal{O}(N_{\text{side}}^3)$, because the energy conservation delta function transforms the state of allowable scattering transitions from a 2D to a 1D space.

The Monte Carlo algorithm proposed in this thesis utilizes a binary search algorithm to identify the post scattering state of a particle, which requires $\mathcal{O}(\log(N_{\text{states}})) = \mathcal{O}(\log(N_{\text{side}}))$ operations per timestep per particle. The overall algorithm therefore requires $\mathcal{O}(N_{\text{parts}} \log(N_{\text{states}}))$ operations per timestep to process all the particles in a spatial cell. Assuming (see Section 6.5) that the number of particles will be proportional to the number of reciprocal space states, the scaling of the number of operations required to evaluate the scattering operator per timestep per physical space cell is

$\mathcal{O}(N_{\text{states}} \log(N_{\text{states}})) = \mathcal{O}(N_{\text{side}}^2 \log(N_{\text{side}}))$, which represents an improvement over the scaling of the iterative and deterministic approaches.

Here we note that the Monte Carlo solutions are associated with statistical uncertainty which, although strictly not an error (bias), it can require significant computational effort to reduce. Due to the slow convergence of Monte Carlo methods (proportional to $1/\sqrt{M}$), where $M$ is the number of independent samples (proportional to the $N_{\text{parts}}$), this can be considered as a disadvantage compared to deterministic simulation methods suffering only from traditional discretization errors, namely timestep, physical space discretization, and reciprocal space discretization (which are also present in the Monte Carlo method presented here). However, our results indicate that, perhaps due to the use of the deviational formulation, for reciprocal space discretizations deemed sufficiently accurate for representing the material model ($N_{\text{side}} \gtrsim 31$), the number of particles per cell is sufficiently large to make statistical noise only a minor and typically negligible consideration. On the other hand, the simplicity of the Monte Carlo method as well as its ability to extend to spatially dependent problems via a robust and efficient algorithm (particularly the advection part of the splitting algorithm—see Section 6.3) is a major advantage compared to deterministic solution methods which require complex numerical constructs (e.g. flux limiters [8]) to deal with the advection operator of the Boltzmann equation.

## 6.10 Conclusion

In this chapter we presented LAIP-LVDSMC, a Monte Carlo algorithm for integrating the phonon Boltzmann equation with the linearized ab initio three phonon scattering operator. Scattering is efficiently and exactly treated using the propagator of Section 5.5. The scaling of this approach with respect to the reciprocal space discretization may give the particle method the advantage over direct evaluation of the matrix vector product in the limit of fine discretizations and it introduces no timestep error in the collision sub step although it does generate additional particles. A time dependent homogenous problem and a spatially dependent SMRT problem are used to validate

the scattering and advection routines, respectively. We also provide a brief discussion of the sources of discretization error particularly noting the discretization error due to the timestep and the error introduced by the cancellation routine.

# Chapter 7

# Kinetic effects in graphene ribbons

A numerical method capable of correctly modeling thermal transport in infinitely large graphene sheets, namely the iterative method described in Chapter 4 and Refs. [87, 109, 113, 112, 71, 77], has only recently been developed. This method is limited to the homogeneous case, formally corresponding to a Knudsen number of $Kn = 0$. To some extent, finite-size effects ($Kn > 0$) have been treated approximately within the homogeneous iterative method. Specifically, as introduced in Section 4.8, the scattering rate may be modified to represent the effect of the boundaries. While including the effect of boundaries without increasing the dimensionality of the problem is an efficient numerical strategy, it must be expected to incur some error. Furthermore, close to a boundary, even as $Kn \to 0$, kinetic (non-Fourier) effects are always important (for example, phonons that have just collided with the boundary travel ballistically for a distance $\Lambda$, on average). A homogeneous simulation is not capable of resolving the spatial dependence of these kinetic effects.

One of the main objectives of this chapter is to use our linearized ab initio phonon low variance deviational simulation Monte Carlo method (LAIP-LVDSMC) to study kinetic effects in graphene and characterize the error associated with approximate approaches. We will focus on graphene ribbons of finite (compared to the mean free path) width or length and along which a temperature gradient causes heat to flow. In both geometries, a reduction in effective thermal conductivity is expected, since, in the first, edge-roughness scattering tends to reduce the heat flux in the direction

parallel to those boundaries (see Section 7.2); while, in the second, traditional finite-size effects (diffusive vs ballistic transport) become important (see Section 7.3). Some aspects of these effects are discussed in Ref. [27] in the context of three-dimensional thin films.

## 7.1 Problem formulation

We consider ribbons of the geometry shown in Figure 7-1. The length of the ribbon in the direction of the imposed gradient is denoted $L$ with $\eta$ being the non-dimensional (normalized by $L$) coordinate such that $0 \leq \eta \leq 1$. The ribbon ends at $\eta = 0$ and $\eta = 1$ are modeled as prescribed temperature boundaries at temperatures $T_\mathrm{h}$ at $\eta = 0$ and $T_\mathrm{c}$ at $\eta = 1$. The width of the ribbon (perpendicular to the temperature gradient) is denoted $W$ with $\xi$ denoting the normalized transverse coordinate such that $0 \leq \xi \leq 1$. The ribbon boundaries (normal to the $\xi$-direction) are assumed to be adiabatic and diffuse.

For finite Knudsen numbers (e.g. $Kn > 0$), the thermal conductivity is no longer described by Equation (3.25) and the heat flux is not necessarily proportional to the temperature gradient. However, we may still define an effective thermal conductivity $\kappa_\mathrm{eff} = -(J_{\eta,E}L)/(T_\mathrm{h} - T_\mathrm{c})$, which is dependent upon the boundary conditions and hence is *not* a material property. In this work, we only consider small temperature differences, where the effective thermal conductivity can be treated as a function of the length and/or width and the average temperature of the material. We will further restrict our study to room temperature (300 K).

## 7.2 Kinetic effects in long graphene ribbons

In this section, as in Section 6.7.2, we consider only the effect of finite width (i.e. edge roughness scattering) by studying infinitely long ribbons under the action of a temperature gradient. Under the infinite length assumption, the governing equation accepts solutions of the form $f_i = f^\mathrm{eq}(\omega_i; T(\eta)) + f_i^\mathrm{d}(\xi)$, which implies that the devi-

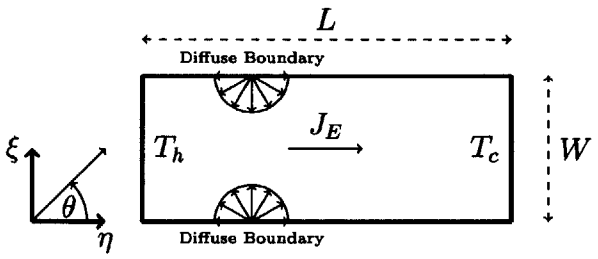


Figure 7-1: Schematic of a graphene ribbon with diffuse boundaries

ation from the local equilibrium is constant along the temperature gradient [124, 49] and that the temperature is a function of $\eta$ but not $\xi$. In other words, we can solve the governing equation for $f_i^{\mathrm{d}}(\xi)$ without reference to the $\eta$ direction—reducing the problem to a single spatial dimension.

### 7.2.1 LAIP-LVDSMC simulations

The LAIP-LVDSMC method is an efficient numerical technique for simulating the spatial variation of phonon transport in finite width ribbons including the effects of normal, umklapp and boundary scattering. As described above the deviation from local equilibrium is independent of the $\eta$ direction. Therefore, using the temperature gradient source term (see Section 6.3.3), an infinitely long ribbon will be simulated by solving only in the $\xi$ spatial dimension.

Figure 7-2 shows the heat flux profile across the width of the ribbon for various $Kn_W$, where $Kn_W = \frac{\Lambda}{W}$ is the Knudsen number and $\Lambda$ is the mean free path (see Equation (3.33)). Similar to the SMRT approximate profiles shown in Figure 6-5, there is a region of reduced heat flux near the boundaries, but with the ab initio three phonon scattering operator, this boundary layer is shown to extend relatively further into the domain for the same Knudsen number as compared to the SMRT results. For both the SMRT and the ab initio results, the average heat flux decreases with increasing Knudsen number, but in the case of the ab initio results, the reduction of the average heat flux with $Kn$ is significantly faster.

Figure 7-3 shows the reduction of the effective thermal conductivity of a finite

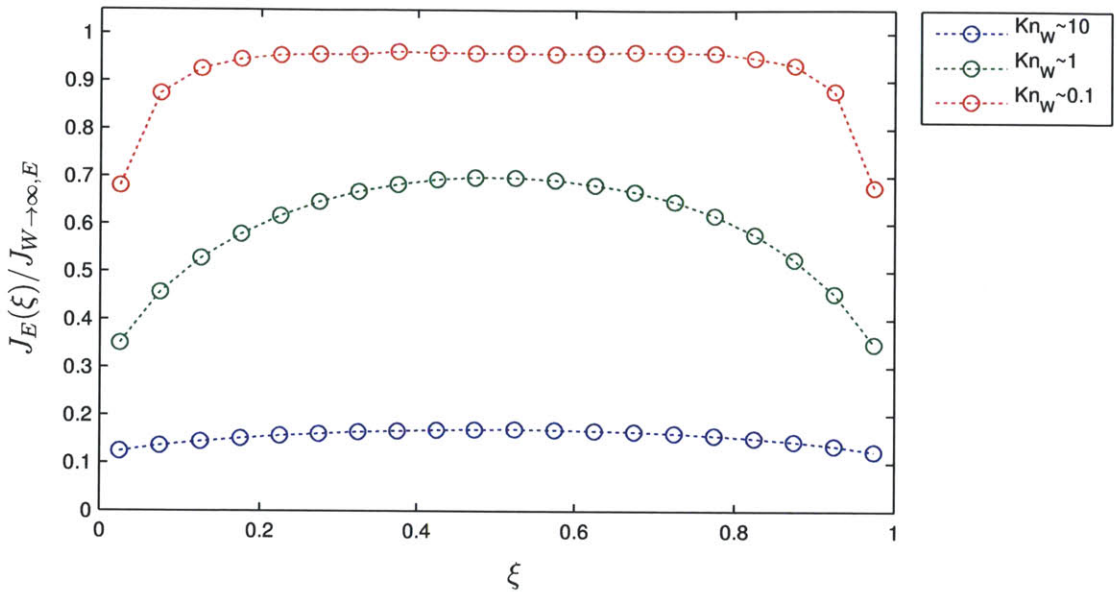


Figure 7-2: Heat flux profile across graphene ribbons of various widths calculated using LAIP-LVDSMC simulations.

width ribbon as a function of the Knudsen number $Kn_W$. The reduction is shown to occur predominately in the traditional transition regime $0.1 \lesssim Kn \lesssim 10$. Given the mean free path of 600nm, this model predicts significant kinetic effects for graphene ribbons with widths less than 6 $\mu$m. Also shown in Figure 7-3 is the prediction of the homogenous approximation of the boundary scattering that is employed in the iterative solution method. It will be discussed in the following section.

### 7.2.2 "Homogeneous" scattering rate approximation

Boundary scattering can be approximated in a "homogeneous" manner introducing an additional scattering rate representative of the boundaries [22]. The scattering rate for a rectangular ribbon is [76]

$$\frac{2v_i|\sin(\theta_i)|}{W} \tag{7.1}$$

where $v_i = ||\boldsymbol{v}_i||$, and $\theta_i$ is the angle between the wavevector (from $i = (\boldsymbol{q}_i s_i)$) and the positive $\xi$ direction measured as shown in Figure 7-1. Assuming that this scattering

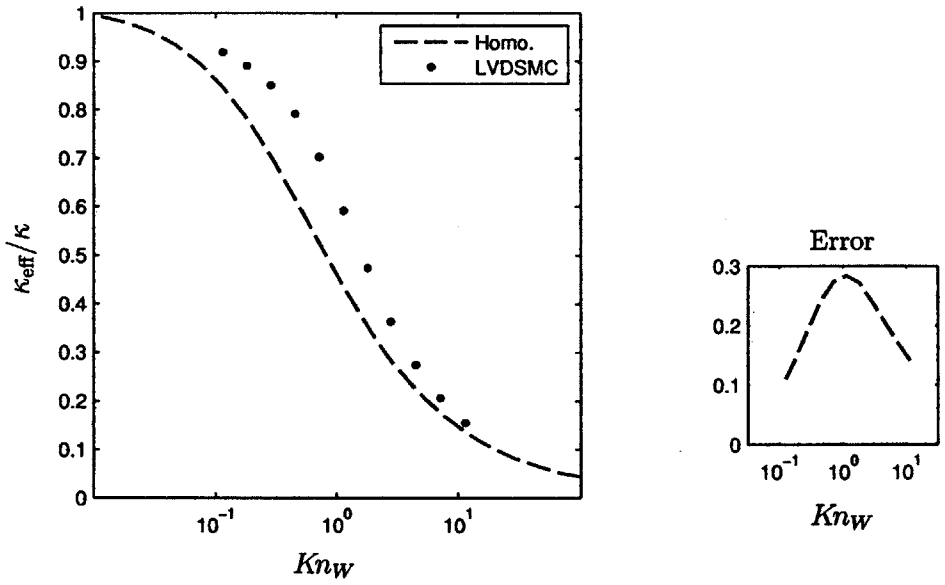


Figure 7-3: Comparison of effective thermal conductivity for an infinitely long ribbon with the ab initio phonon scattering operator calculated by LVDSMC and using the homogeneous scattering rate approximation.

occurs homogeneously, its rate can be summed with the phonon-phonon scattering rates ($\Gamma_i$ or $B_{ii}$) using Matthiessen's rule. This yields an approximate phonon lifetime

$$\tau_i^{\text{approx}} = \tau_i \left(1 + 2Kn_{i,W}|\sin(\theta_i)|\right)^{-1} \tag{7.2}$$

where $Kn_{i,W} = \frac{\tau_i v_i}{W}$ is a Knudsen number based on the state dependent free path.

The homogeneous scattering rate results are also shown in 7-3. This approximation is shown to introduce an error that reaches nearly 30 % near $Kn_W = 1$. The homogenous approximation also predicts more significant kinetic effects at lower Knudsen numbers than the ab initio results—specifically for length scales on the order of $1\mu$m, the homogenous approximation predicts reduction of thermal conductivity between 10 and 30%, whereas the ab initio results predict reductions between 7 and 15%. Based on the fidelity of the model, we expect the latter to be more accurate.

### Deduction from the SMRT model

The error resulting from using a homogeneous scattering term to approximate the presence of transverse boundaries can be better understood by comparing expression (7.2) with the effective relaxation time

$$\tau_i^{\text{exact,SMRT}} = \tau_i \left[1 - |\sin(\theta_i)| Kn_{i,W} \left(1 - \exp\left(-\frac{1}{Kn_{i,W}|\sin(\theta_i)|}\right)\right)\right]. \tag{7.3}$$

obtained from the analytical solution of the space-dependent Boltzmann equation, *albeit in the SMRT approximation*, in Section 6.7.2. This effective relaxation time is obtained by comparing equations (6.30) and (6.24) and clearly shows how boundaries (rather than a homogeneous scattering term) determine the effective relaxation time according to the Boltzmann equation (in the relaxation time approximation). By comparing the two expressions one can see that one of the limitations of the homogeneous approach is the neglect of the spatial variation of non-equilibrium (and thus relaxation) in the domain.

To make the comparison more quantitative, we define $R_i = \tau_i^{\text{exact,SMRT}}/\tau_i^{\text{approx}}$. It can be verified that in the ballistic and the diffusive limits the two lifetimes are the same, namely,

$$\lim_{Kn_{i,W}\to 0} R_i = \lim_{Kn_{i,W}\to\infty} R_i = 1. \tag{7.4}$$

This is an expected result because in both of these limits one of the two scattering mechanisms that are summed by Matthiessen's rule (boundary or intrinsic) is negligible, so the homogeneous approximation becomes exact. Between the two limits, the ratio of the two modified relaxation times varies by as much as 14% (see Figure 7-4). This result is independent of the relaxation times, but does rely on the SMRT approximation.

When the thermal conductivity is integrated over all modes, the resulting maximum error (assuming the analytical SMRT solution to be exact) is reduced to about 8% (see Figure 7-5). This is in contrast to the ab initio simulations where the difference between the homogenous approximation and the LAIP-LVDSMC results was

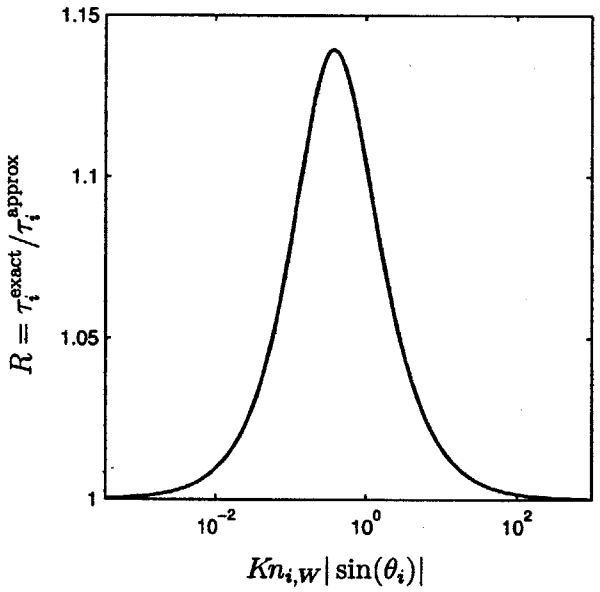


Figure 7-4: The ratio of the modified relaxation times for the approximate and exact solutions. The approximate "homogeneous" solution carries an error as large as 14% for modes with $Kn_{i,W}|\sin(\theta_i)| \sim 0.37$.

as large as 30%. This suggests that coupling between out-of-equilibrium modes further complicates the interaction between intrinsic and boundary scattering making Matthiessen's rule less reliable.

### 7.2.3 Landauer-like approximation

In order to predict average behavior without the computational burden of ab initio simulations, we note that the transition regime behavior of finite width ribbons can be reasonably well approximated much more simply. The reduction in effective thermal conductivity (as a function of the Knudsen number) can be approximately captured using the Landauer-like approach (see Equation (4.33) and Refs. [66, 98, 100, 55])

$$\frac{\kappa_{\text{eff}}}{\kappa} = \frac{1}{1 + \beta_W Kn_W} \tag{7.5}$$

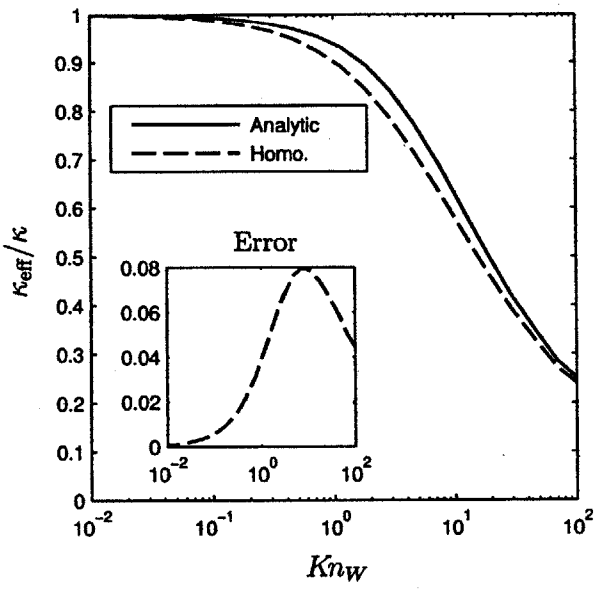


Figure 7-5: Comparison of effective thermal conductivity of an infinitely long ribbon over a range of Knudsen numbers $Kn_W = \Lambda/W$–calculated using a homogeneous SMRT solution (labeled "Homo."), and the analytical SMRT solution (labeled "Analytic").

where the coefficient $\beta_W$ will, in general, depend on the material and the type of boundary conditions it is subject to. Here, $\beta_W \approx .53$ seems to describe the data well (see Figure 7-6)—within 10% error for the transition regime, $0.1 \lesssim Kn \lesssim, 10$, which is better than the homogeneous scattering rate approach. Both the model and the parameter value are entirely phenomenological in this case, but may be useful to provide simple estimates for simulation and experiment design.

## 7.3 Finite-length ribbons

Unlike the infinitely long ribbons of the previous section, in all practical applications, graphene ribbons have finite length and may terminate in graphitic heat sinks [41, 10], or contacts which can be approximated as prescribed-temperature boundary conditions. Phonons emitted from such a boundary may have a substantially different distribution than those arriving at the boundary. This non-equilibrium distribution

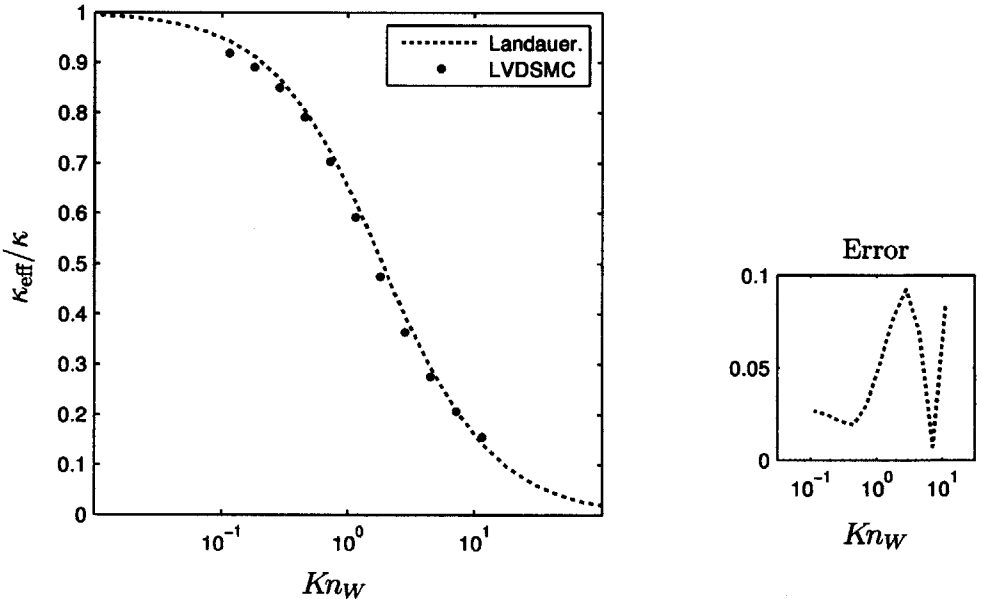


Figure 7-6: Comparison of effective thermal conductivity for an infinitely long ribbon with the ab initio phonon scattering operator calculated by LAIP-LVDSMC and using a fitted Landauer-like approximation.

will persist until the entering phonons have had a chance to thermalize with the local phonon population (e.g. a few mean free paths).

Figure 7-7 shows the temperature profiles calculated from LAIP-LVDSMC for various Knudsen numbers. These calculations were performed using the prescribed temperature boundary conditions described in Section 6.3.1 in the axial ($\eta$) direction ($T^* = 1, -1$ at $\eta = 1, 0$ respectively) , while in the transverse direction the simulation was taken to be periodic. The prescribed temperature boundary condition is shown to introduce a region of non-linear temperature gradient (implying Fourier's law does not hold) as well as to decrease the temperature gradient in the "bulk" away from the boundary—a linear segment of the temperature gradient is present only in the $Kn_L = 0.1$ case.

In the Boltzmann equation literature, the linear (bulk) profile is extrapolated to the wall to provide the boundary condition that needs to be supplied to Fourier's law so that the latter can reproduce the correct behavior *away from the boundary.*

In Figure 7-7 for $Kn = 0.1$, the linearly extrapolated temperature at the boundary is $\approx 0.8$, which is different from the imposed boundary temperature ($T^* = \pm 1$); in other words, a temperature jump exists. For the $Kn = 1$ and $Kn = 10$ profiles, kinetic effects are expected to span the entire domain and Fourier's law cannot be applied [93].

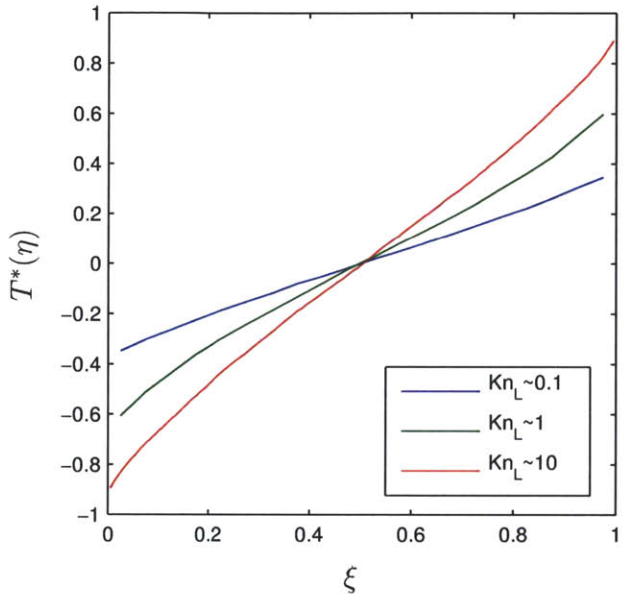


Figure 7-7: Temperature profile along a finite length ribbon for various $Kn = \Lambda/L$ calculated using ab initio LVDSMC simulations. These profiles exhibit a clear temperature jump with respect to the applied temperature of $\pm 1$. The dimensionless temperature is $T^*(\eta) = 2\frac{T(\eta)-T_0}{T_h-T_c}$.

In terms of heat flux, the net effect of the finite length of the ribbon is to diminish transport, which has been termed "ballistic resistance" [98, 55, 100, 79, 25, 61, 111]. Figure 7-8 shows the reduction in heat flux due to finite length as calculated by LAIP-LVDSMC for a range of $Kn_L$. At $Kn_L \approx 0.1$ the thermal conductivity has already been reduced from the bulk value by 15%. In contrast, the finite width reduction at $Kn_W = 0.1$ was approximately half that amount. In other words, the effective thermal conductivity is more sensitive to reductions in length than to reductions in width. This is of course dependent upon our representation of the interface as atomically sharp one. The physical fidelity of this approximation must still be investigated.

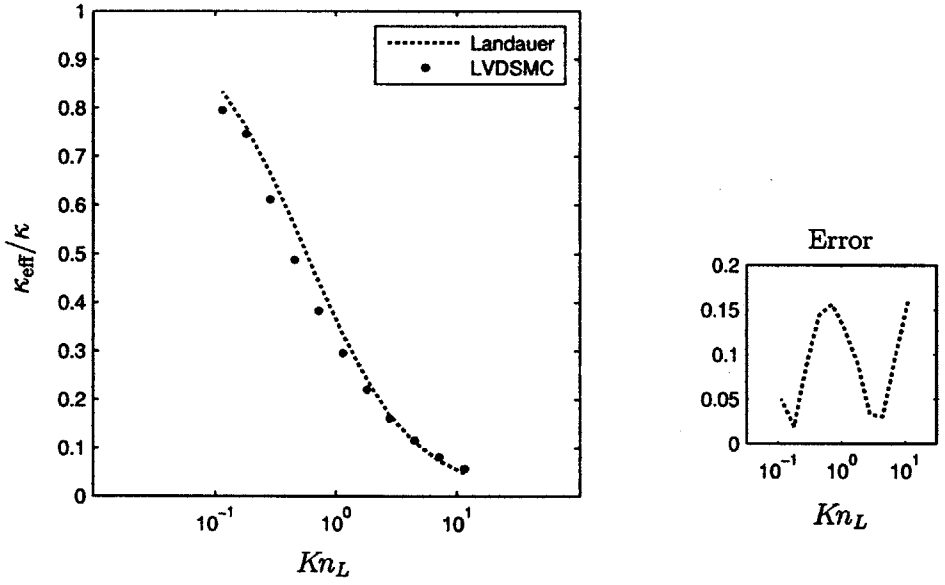


Figure 7-8: Comparison of effective thermal conductivity for an infinitely wide, finite length ribbon over a range of Knudsen numbers $Kn_L = \Lambda/L$.

### 7.3.1 Approximate treatment of ballistic resistance

There exist two main *approximate* approaches for including the ballistic resistance in Boltzmann equation simulations: 1) exclusion of all modes with mean free path greater than the device length [58, 79] or 2) introduction of an additional resistance implemented using a Landauer-like expression [83, 100, 98]. The first of these approximations has its roots more strongly in convenience rather than physical realities. It dates back at least to 2001 when Klemens proposed a frequency cutoff to remove the divergent thermal conductivity predicted by his model that did not correctly consider momentum and energy conservation requirements nor branch selection rules. Klemens' approach qualitatively leads to the correct behavior for the effective thermal conductivity [83, 67] (i.e. decreasing effective conductivity with length), but clearly will predict zero transport for a purely ballistic problem. Furthermore, this approximation relies on decoupling of ballistic and diffusive modes [79]. Due to the importance of mode coupling in graphene as evidenced by the difference between the SMRT thermal conductivity and the ab initio calculations [71, 112] the validity of

decoupling the ballistic and diffusive modes in the context of graphene is questionable.

The second approximate approach, the Landauer-like approach, can be justified by noting that, especially in the (approximate) one-dimensional form simulated here, this problem is classical Fourier conduction problem, which is well described by the Landauer form

$$\frac{\kappa_{eff}}{\kappa} = \frac{1}{1 + \beta_L Kn_L} \tag{7.6}$$

where Ref [98] gives $\beta_L = \frac{\pi}{2}$, but we found $\beta_L = 1.75$ to better describe our data. This approximation should at least be correct in the two limits (i.e. $Kn \to 0$ and $Kn \to \infty$) [99], and it has been shown to agree with experiments for other systems [100]. As shown in Figure 7-3, this approximation is within 15% of the LAIP-LVDSMC solution for $0.1 \lesssim Kn \lesssim 10$, making it a valuable simple model.

## 7.4 Two dimensional simulations of finite length, finite width ribbons

In this section we use two-dimensional LAIP-LVDSMC simulation to show the combined effects of both finite width and finite length ribbons in a full two-dimensional problem. An approximation for this multi dimensional behavior is provided by summing the finite width and finite length Landauer-like scattering rates (essentially assuming that they act as resistances in parallel)

$$\frac{\kappa_{eff}}{\kappa} = \frac{1}{1 + \beta_L Kn_L + \beta_W Kn_W}. \tag{7.7}$$

While parameters $\beta_L$ and $\beta_W$ could be adjusted to improve agreement with the data, we chose to use the parameters optimized for the one dimensional problems: $\beta_W = 0.53$ and $\beta_L = 1.75$. The error of the approximation is generally comparable to the sum of the two individual components, so it appears that our superposition of the finite width and finite length problems introduces little or no additional error into our approximate model. Nevertheless, we reiterate that this approximate model is

incapable of providing the spatial variation of the temperature and heat flux profiles. This spatial variation can be even more important when considering more complicated geometries (e.g. a circular heated region in a rectangular geometry).

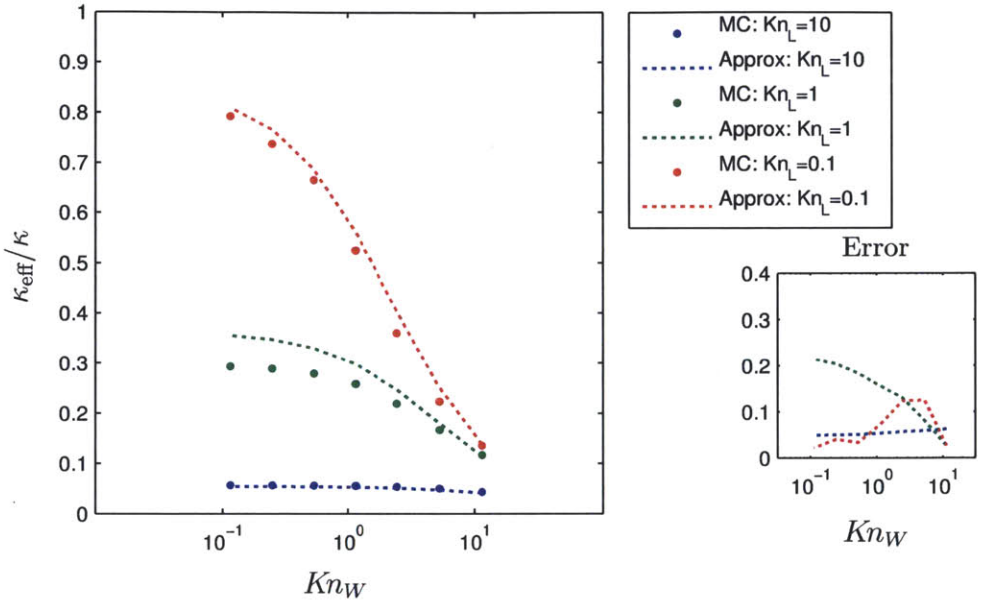


Figure 7-9: The combined effects of finite width and finite length as described by the Knudsen numbers $Kn_L$ and $Kn_W$ are shown for the graphene ribbon geometry.

## 7.5 Conclusions

The LAIP-LVDSMC simulation is used to characterize the heat flux profile in finite width graphene ribbons and the temperature profile in finite length graphene ribbons. Both the finite width and the finite length are shown to reduce the effective thermal conductivity although the mechanisms associated with this reduction are distinct. Finally, the combined finite width and finite length problem is solved using two-dimensional simulations. A simple Landauer-like model captures the transition from diffusive to ballistic transport reasonably well (with 10% error for the finite width problem, within 15% error for the finite length problem, and within 25% error for the finite width and finite length problem). This compares very favorably with the

maximum of 30% error observed when using an additional homogeneous scattering rate to model the effects of transverse boundaries in homogeneous calculations.

The standard kinetic theory prediction of transition between $0.1 \lesssim Kn \lesssim 10$ agrees reasonably well with the data, suggesting that the definition for the mean free path developed and proposed in Section 3.5.1 is reasonable and effective. We note that the effective thermal conductivity in the finite length tends to be more sensitive to reductions in length than the finite width problem and transition begins at a relatively smaller Knudsen number. In the two-dimensional problem, we show that both the Knudsen number in terms of width and length must be small in order to eliminate kinetic effects from a simulation. These results and the simple Landauer-like models should provide useful guidelines for future simulation and experimental efforts.

# Chapter 8

# Final remarks

In this thesis we describe a deviational Monte Carlo method for solving the Boltzmann equation for phonon transport subject to the linearized ab-initio three-phonon scattering operator. We use the method to study heat transport in graphene ribbons, a geometry used to experimentally measure the thermal conductivity of graphene. Our results show that in addition to the insight obtained from spatially and temporally resolved transport fields, this method is useful for validating and characterizing the error associated with simple models. Of particular interest is the finding that the treatment of boundaries using a homogeneous scattering term leads up to 30% error in the effective thermal conductivity. Our hope is that the proposed method will be used by the scientific community in the future to study a variety of materials and processes of practical and scientific interest.

In this context, we note that the method for treating the ab-initio collision operator developed here is general and does not rely on assumptions about the material dimensionality. Similarly, the particle formulation for integrating the advection part of the Boltzmann equation readily extends to three-dimensional simulations. In fact, the simplicity with which arbitrary three dimensional geometries can be treated is one of the big advantages of this approach compared to mesh-based approaches. In other words, we expect that the complete method for simulating phonon transport using the ab-initio collision operator should directly extend to 3D materials, making ab-initio simulations of all materials of interest possible, provided suitable material

information is available (i.e. second and third order force constants). The cost of the method will clearly be larger in three dimensions. The largest computational cost increase is expected to be due to the increase of states in the reciprocal space discretization, but we note that these calculations are already being performed in three dimensions for spatially homogeneous problems [88, 77].

One of the major ingredients of the method developed in this thesis is the energy-conserving, stochastic particle method for simulating the action of the linearized ab-initio scattering operator during the homogeneous relaxation step of the splitting algorithm described in Chapter 6. Although this algorithm is very efficient—it requires roughly $\mathcal{O}(N_{\text{states}} \log(N_{\text{states}}))$ operations per timestep—and exhibits no timestep error, it generates additional particles, which need to be dealt with within the computational formulation. The present work achieves stability using a simple cancellation approach: particles of opposite sign but of the same discrete wave vector and within the same computational cell in physical space are cancelled. This approach introduces some numerical error which may be reduced by developing less crude approaches such as the one outlined in [93] under the section labelled "Termination of particle trajectories" and shown to be second order accurate in the cell size. Although the latter technique is developed in the context of a timestep-free, kinetic-type algorithm and is limited to steady problems, it may be possible to adapt it to the present method.

Alternatively, timestep-free formulations of the present algorithm should also be pursued, since they could be beneficial not just in the context of particle cancellation, but as a general acceleration strategy. As explained in [93], such methods reduce the computational cost because they reduce memory and processing requirements (particles are treated independently), but also because they automatically adapt the timestep to the characteristic timescale of each particle (mode). The latter will in general lead to (significantly) larger timesteps compared to timestep-based algorithms which, strictly speaking, need to use a timestep that is smaller than the smallest relaxation time.

While the computational framework presented in this thesis provides exciting op-

portunities to study kinetic effects in previously inaccessible systems, the quality of the results will of course depend upon the fidelity of the material model—namely the second and third order force constants. We have shown in this work that numerical errors in calculating the third order force constants can lead to significant uncertainties in the calculation of transport properties (estimated to be as large as 25% in the present work). For this reason, we have limited ourselves to moderately fine discretizations of reciprocal space ($N_{\text{side}} = 81$) when calculating thermal conductivity and $N_{\text{side}} = 31$ when calculating relative transport properties (e.g. $\kappa_{\text{eff}}(Kn_W)/\kappa$). We also note that convergence with respect to reciprocal space discretization is improved by the presence of boundary scattering. We expect that the above discretizations should provide results well within the uncertainty of 25% inherent in the material model, but these matters should be investigated further as uncertainties in the material model are improved. We expect that the investigation of energy and momentum conservation in this work will provide direction for efforts towards improving numerical calculations of force constants.

The reciprocal space discretization of the material model is currently the most resource intensive part of the computation. When finer reciprocal space discretizations are desired, the computational cost of calculating the matrix exponential, which scales as $\mathcal{O}(N_{\text{states}}^4)$, may become limiting. Some of the computational cost may be alleviated by using the first order approximation for calculating the propagator (Equation (5.44)). This approach also has the potential to preserve sparsity of the propagator matrix, provided a suitable energy conserving scheme is developed (see the last paragraph of Section 5.4). For discretizations on the order of $N_{\text{side}} \sim 100$, memory requirements were on the order of tens of gigabytes even when using the first-order, sparse matrix formulation. Further efficiency improvements and/or supercomputing resources will be required to obtain simulations at finer discretizations.

In the above context, we note that one advantage of Monte Carlo methods, as opposed to deterministic approaches, is that there is no underlying need for discretizing the reciprocal space. In this work, reciprocal space discretization was forced upon us because no acceptable continuous description of the scattering operator in reciprocal

space was available. If such a representation is developed either for the linearized operator used in this work or its non-linear counterpart (Equation (3.7)), it could lead to more efficient Monte Carlo algorithms. We expect future work will focus on scattering models (linearized and non-linear) and particle method implementations that will allow for stable (in terms of number of particles) simulations without discretizing reciprocal space, which should prove an enormous benefit in terms of convergence and computational resource requirements.

# Appendix A

# Equilibrium related coefficients

The scattering operator (3.7) evaluated at equilibrium is zero. Given three states $i$, $j$, and $k$ whose frequencies satisfy $\omega_i + \omega_j - \omega_k = 0$, this leads to the condition

$$(n_i^0 + 1)(n_j^0 + 1)n_k^0 = n_i^0 n_j^0 (n_k^0 + 1) \quad \text{for} \quad (\omega_i + \omega_j - \omega_k = 0). \tag{A.1}$$

This expression can be expanded to

$$n_j^0 n_k^0 + n_i^0 n_k^0 + n_k^0 = n_i^0 n_j^0 \quad \text{for} \quad (\omega_i + \omega_j - \omega_k = 0). \tag{A.2}$$

where the $n_i^0 n_j^0 n_k^0$ terms cancel. Equation (A.2) leads to the following useful relation by grouping of terms:

$$n_i^0 + n_j^0 + 1 = \frac{n_i^0 n_j^0}{n_k^0} \tag{A.3}$$

$$n_i^0 - n_k^0 = \frac{n_k^0 (n_i^0 + 1)}{n_j^0} \tag{A.4}$$

$$n_i^0 - n_k^0 = \frac{n_k^0 (n_j^0 + 1)}{n_i^0} \tag{A.5}$$

which are again only valid for states that satisfy $\omega_i + \omega_j - \omega_k = 0$.

These relations can be used to transform Equation (4.24) into Equation (4.27) as well as various other forms that appear in the literature. For a finite grid, the energy conservation is not exactly satisfied by the states in the discretization, so we expect

that different forms will result in "slightly" different transport properties for finite discretizations, but should converge to the same result as the grid is refined.

# Appendix B

# Simulation parameters

In order to facilitate the correct usage of the LAIP-LVDSMC simulation method presented herein, this appendix documents the parameters used to generate the results reported where those parameters are not clear from the text. Table 6.1 describes the two letter abbreviations used in this appendix for the input parameters, and Table 6.2 describes the two letter abbreviations used for derived simulation parameters.

Table B.1: Input and derived parameters for Figure 6-2 and for the steady state value also reported.

| Run # | T0 | TG | LS | NS | DT | PT | NC | CF | TS | SS | NE |
|---|---|---|---|---|---|---|---|---|---|---|---|
| 1 | 300.0 | 1e-05 | 0.6 | 11 | 1 | 200 | 1 | 1 | 2000 | 2000 | 100 |
| 2 | 300.0 | 1e-05 | $\infty$ | 11 | 1 | 720 | 1 | 1 | 20000 | 20000 | 1 |

| Run # | PC | LC | TM | TC | KN | TT | TB | CM |
|---|---|---|---|---|---|---|---|---|
| 1 | 125 | 1.55 | 0.066 | 0.0019 | 0.645 | 132 | 3.8 | 0.0171 |
| 2 | 449 | 1.55 | – | 0.0019 | 0 | 1.32e+03 | – | 0.123 |

Table B.2: Input and derived parameters for Figures 6-4 and 6-5

| Run # | T0 | TG | LS | NS | DT | PT | NC | CF | TS | SS | NE |
|---|---|---|---|---|---|---|---|---|---|---|---|
| 1 | 300.0 | 0 | 0.06 | 31 | 0.5 | 1000 | 20 | 1 | 4000 | 4000 | 1 |
| 2 | 300.0 | 0 | 0.0951 | 31 | 0.5 | 1000 | 20 | 1 | 4000 | 4000 | 1 |
| 3 | 300.0 | 0 | 0.151 | 31 | 0.5 | 1000 | 20 | 1 | 4000 | 4000 | 1 |
| 4 | 300.0 | 0 | 0.239 | 31 | 0.5 | 1000 | 20 | 1 | 4000 | 4000 | 1 |
| 5 | 300.0 | 0 | 0.379 | 31 | 1 | 2000 | 20 | 1 | 2000 | 2000 | 1 |
| 6 | 300.0 | 0 | 0.6 | 31 | 1 | 2000 | 20 | 1 | 2000 | 2000 | 1 |
| 7 | 300.0 | 0 | 0.951 | 31 | 1 | 2000 | 20 | 1 | 2000 | 2000 | 1 |
| 8 | 300.0 | 0 | 1.51 | 31 | 1 | 2000 | 20 | 1 | 2000 | 2000 | 1 |
| 9 | 300.0 | 0 | 2.39 | 31 | 1 | 2000 | 20 | 1 | 2000 | 2000 | 1 |
| 10 | 300.0 | 0 | 3.79 | 31 | 1 | 2000 | 20 | 1 | 2000 | 2000 | 1 |
| 11 | 300.0 | 0 | 6 | 31 | 1 | 4000 | 40 | 1 | 2000 | 2000 | 1 |

| Run # | PC | LC | TM | TC | KN | TT | TB | CM |
|---|---|---|---|---|---|---|---|---|
| 1 | 1.79 | 0.00439 | 0.0241 | 3.55 | 11.4 | 96.6 | 709 | 0.0827 |
| 2 | 2.08 | 0.00695 | 0.0241 | 2.24 | 7.19 | 96.6 | 448 | 0.0899 |
| 3 | 2.37 | 0.011 | 0.0241 | 1.41 | 4.53 | 96.6 | 282 | 0.102 |
| 4 | 2.63 | 0.0175 | 0.0241 | 0.891 | 2.86 | 96.6 | 178 | 0.106 |
| 5 | 2.84 | 0.0277 | 0.0483 | 1.12 | 1.8 | 96.6 | 112 | 0.179 |
| 6 | 3.01 | 0.0439 | 0.0483 | 0.709 | 1.14 | 96.6 | 70.9 | 0.184 |
| 7 | 3.13 | 0.0695 | 0.0483 | 0.448 | 0.719 | 96.6 | 44.8 | 0.202 |
| 8 | 3.22 | 0.11 | 0.0483 | 0.282 | 0.453 | 96.6 | 28.2 | 0.17 |
| 9 | 3.29 | 0.175 | 0.0483 | 0.178 | 0.286 | 96.6 | 17.8 | 0.259 |
| 10 | 3.34 | 0.277 | 0.0483 | 0.112 | 0.18 | 96.6 | 11.2 | 0.258 |
| 11 | 3.38 | 0.219 | 0.0483 | 0.142 | 0.114 | 96.6 | 7.09 | 0.552 |

Table B.3: Input and derived parameters for Figures 7-2 and 7-3.

| Run # | T0 | TG | LS | NS | DT | PT | NC | CF | TS | SS | NE |
|---|---|---|---|---|---|---|---|---|---|---|---|
| 1 | 300.0 | 0 | 0.06 | 31 | 0.5 | 1000 | 20 | 1 | 4000 | 4000 | 1 |
| 2 | 300.0 | 0 | 0.0951 | 31 | 0.5 | 1000 | 20 | 1 | 4000 | 4000 | 1 |
| 3 | 300.0 | 0 | 0.151 | 31 | 0.5 | 1000 | 20 | 1 | 4000 | 4000 | 1 |
| 4 | 300.0 | 0 | 0.239 | 31 | 0.5 | 1000 | 20 | 1 | 4000 | 4000 | 1 |
| 5 | 300.0 | 0 | 0.379 | 31 | 1 | 2000 | 20 | 1 | 2000 | 2000 | 1 |
| 6 | 300.0 | 0 | 0.6 | 31 | 1 | 2000 | 20 | 1 | 2000 | 2000 | 1 |
| 7 | 300.0 | 0 | 0.951 | 31 | 1 | 2000 | 20 | 1 | 2000 | 2000 | 1 |
| 8 | 300.0 | 0 | 1.51 | 31 | 1 | 2000 | 20 | 1 | 2000 | 2000 | 1 |
| 9 | 300.0 | 0 | 2.39 | 31 | 1 | 2000 | 20 | 1 | 2000 | 2000 | 1 |
| 10 | 300.0 | 0 | 3.79 | 31 | 1 | 2000 | 20 | 1 | 2000 | 2000 | 1 |
| 11 | 300.0 | 0 | 6 | 31 | 1 | 2000 | 20 | 1 | 2000 | 2000 | 1 |

| Run # | PC | LC | TM | TC | KN | TT | TB | CM |
|---|---|---|---|---|---|---|---|---|
| 1 | 3.14 | 0.00439 | 0.0241 | 3.55 | 11.4 | 96.6 | 709 | 0.225 |
| 2 | 4.25 | 0.00695 | 0.0241 | 2.24 | 7.19 | 96.6 | 448 | 0.374 |
| 3 | 5.82 | 0.011 | 0.0241 | 1.41 | 4.53 | 96.6 | 282 | 0.346 |
| 4 | 8 | 0.0175 | 0.0241 | 0.891 | 2.86 | 96.6 | 178 | 0.844 |
| 5 | 11 | 0.0277 | 0.0483 | 1.12 | 1.8 | 96.6 | 112 | 1.23 |
| 6 | 14.3 | 0.0439 | 0.0483 | 0.709 | 1.14 | 96.6 | 70.9 | 1.69 |
| 7 | 17.7 | 0.0695 | 0.0483 | 0.448 | 0.719 | 96.6 | 44.8 | 1.61 |
| 8 | 20.6 | 0.11 | 0.0483 | 0.282 | 0.453 | 96.6 | 28.2 | 2.13 |
| 9 | 2.83 | 0.175 | 0.0483 | 0.178 | 0.286 | 96.6 | 17.8 | 1.39 |
| 10 | 24.2 | 0.277 | 0.0483 | 0.112 | 0.18 | 96.6 | 11.2 | 2.43 |
| 11 | 25.1 | 0.439 | 0.0483 | 0.0709 | 0.114 | 96.6 | 7.09 | 2.6 |

Table B.4: Input and derived parameters for Figures 7-7 and 7-8.

| Run # | T0 | TG | LS | NS | DT | PT | NC | CF | TS | SS | NE |
|---|---|---|---|---|---|---|---|---|---|---|---|
| 1 | 300.0 | 0.0001 | 0.06 | 31 | 0.1 | 1000 | 20 | 1 | 20000 | 20000 | 1 |
| 2 | 300.0 | 6.3091e-05 | 0.0951 | 31 | 0.1 | 1000 | 20 | 1 | 20000 | 20000 | 1 |
| 3 | 300.0 | 3.9735e-05 | 0.151 | 31 | 0.1 | 1000 | 20 | 1 | 20000 | 20000 | 1 |
| 4 | 300.0 | 2.5105e-05 | 0.239 | 31 | 0.1 | 1000 | 20 | 1 | 20000 | 20000 | 1 |
| 5 | 300.0 | 1.5831e-05 | 0.379 | 31 | 0.1 | 2000 | 20 | 1 | 20000 | 20000 | 1 |
| 6 | 300.0 | 1e-05 | 0.6 | 31 | 0.5 | 200 | 20 | 1 | 4000 | 4000 | 1 |
| 7 | 300.0 | 6.3091e-06 | 0.951 | 31 | 0.5 | 2000 | 20 | 1 | 4000 | 4000 | 1 |
| 8 | 300.0 | 3.9735e-06 | 1.51 | 31 | 0.5 | 2000 | 20 | 1 | 4000 | 4000 | 1 |
| 9 | 300.0 | 2.5105e-06 | 2.39 | 31 | 0.5 | 2000 | 20 | 1 | 4000 | 4000 | 1 |
| 10 | 300.0 | 1.5831e-06 | 3.79 | 31 | 1 | 2000 | 20 | 1 | 4000 | 4000 | 1 |
| 11 | 300.0 | 1e-06 | 6 | 31 | 6 | 200 | 100 | 1 | 80000 | 80000 | 1 |

| Run # | PC | LC | TM | TC | KN | TT | TB | CM |
|---|---|---|---|---|---|---|---|---|
| 1 | 0.791 | 0.00439 | 0.00483 | 0.284 | 11.4 | 96.6 | 284 | 0.0415 |
| 2 | 1.13 | 0.00695 | 0.00483 | 0.18 | 7.19 | 96.6 | 180 | 0.0557 |
| 3 | 1.64 | 0.011 | 0.00483 | 0.113 | 4.53 | 96.6 | 113 | 0.0741 |
| 4 | 2.4 | 0.0175 | 0.00483 | 0.0715 | 2.86 | 96.6 | 71.5 | 0.112 |
| 5 | 6.94 | 0.0277 | 0.00483 | 0.0451 | 1.8 | 96.6 | 45.1 | 0.275 |
| 6 | 0.386 | 0.0439 | 0.0241 | 0.142 | 1.14 | 96.6 | 28.4 | 0.0279 |
| 7 | 3.27 | 0.0695 | 0.0241 | 0.0897 | 0.719 | 96.6 | 17.9 | 0.199 |
| 8 | 5.18 | 0.11 | 0.0241 | 0.0566 | 0.453 | 96.6 | 11.3 | 0.352 |
| 9 | 8.95 | 0.175 | 0.0241 | 0.0357 | 0.286 | 96.6 | 7.15 | 0.568 |
| 10 | 7.9 | 0.277 | 0.0483 | 0.0451 | 0.18 | 193 | 9.02 | 0.569 |
| 11 | 0.311 | 0.0877 | 0.29 | 0.853 | 0.114 | 2.32e+04 | 683 | 0.392 |

Table B.5: Input parameters for Figure 7-9.

| Run # | T0 | TG | LS(x,y) | NS | DT | PT | NC(x,y) | CF | TS | SS | NE |
|---|---|---|---|---|---|---|---|---|---|---|---|
| 1 | 300.0 | 0.0016667 | 0.06,0.06 | 31 | 0.1 | 10000 | 20,20 | 1 | 20000 | 20000 | 1 |
| 2 | 300.0 | 0.0016667 | 0.06,0.129 | 31 | 0.1 | 10000 | 20,20 | 1 | 20000 | 20000 | 1 |
| 3 | 300.0 | 0.0016667 | 0.06,0.279 | 31 | 0.1 | 10000 | 20,20 | 1 | 20000 | 20000 | 1 |
| 4 | 300.0 | 0.0016667 | 0.06,0.6 | 31 | 0.1 | 10000 | 20,20 | 1 | 20000 | 20000 | 1 |
| 5 | 300.0 | 0.0016667 | 0.06,1.29 | 31 | 0.1 | 10000 | 20,20 | 1 | 20000 | 20000 | 1 |
| 6 | 300.0 | 0.0016667 | 0.06,2.79 | 31 | 0.1 | 10000 | 20,20 | 1 | 20000 | 20000 | 1 |
| 7 | 300.0 | 0.0016667 | 0.06,6 | 31 | 0.1 | 10000 | 20,20 | 1 | 20000 | 20000 | 1 |
| 8 | 300.0 | 0.00016667 | 0.6,0.06 | 31 | 0.1 | 2000 | 20,20 | 1 | 20000 | 20000 | 1 |
| 9 | 300.0 | 0.00016667 | 0.6,0.129 | 31 | 0.1 | 2000 | 20,20 | 1 | 20000 | 20000 | 1 |
| 10 | 300.0 | 0.00016667 | 0.6,0.279 | 31 | 0.1 | 2000 | 20,20 | 1 | 20000 | 20000 | 1 |
| 11 | 300.0 | 0.00016667 | 0.6,0.6 | 31 | 0.1 | 2000 | 20,20 | 1 | 20000 | 20000 | 1 |
| 12 | 300.0 | 0.00016667 | 0.6,1.29 | 31 | 0.1 | 2000 | 20,20 | 1 | 20000 | 20000 | 1 |
| 13 | 300.0 | 0.00016667 | 0.6,2.79 | 31 | 0.1 | 2000 | 20,20 | 1 | 20000 | 20000 | 1 |
| 14 | 300.0 | 0.00016667 | 0.6,6 | 31 | 0.1 | 2000 | 20,20 | 1 | 20000 | 20000 | 1 |
| 15 | 300.0 | 1.6667e-05 | 6,0.06 | 31 | 3 | 200 | 20,20 | 1 | 160000 | 160000 | 1 |
| 16 | 300.0 | 1.6667e-05 | 6,0.129 | 31 | 3 | 200 | 20,20 | 1 | 160000 | 160000 | 1 |
| 17 | 300.0 | 1.6667e-05 | 6,0.279 | 31 | 3 | 200 | 20,20 | 1 | 160000 | 160000 | 1 |
| 18 | 300.0 | 1.6667e-05 | 6,0.6 | 31 | 3 | 200 | 20,20 | 1 | 160000 | 160000 | 1 |
| 19 | 300.0 | 1.6667e-05 | 6,1.29 | 31 | 3 | 200 | 20,20 | 1 | 160000 | 160000 | 1 |
| 20 | 300.0 | 1.6667e-05 | 6,2.79 | 31 | 3 | 200 | 20,20 | 1 | 160000 | 160000 | 1 |
| 21 | 300.0 | 1.6667e-05 | 6,6 | 31 | 3 | 200 | 20,20 | 1 | 160000 | 160000 | 1 |

Table B.6: Derived parameters for Figure 7-9.

| Run # | PC | LC (x,y) | TM | TC (x,y) | KN (L,W) | TT | TB (x,y) | CM |
|---|---|---|---|---|---|---|---|---|
| 1 | 0.319 | 0.00439, 0.00439 | 0.00483 | 0.284, 0.284 | 11.4, 11.4 | 96.6 | 284, 284 | 0.761 |
| 2 | 0.362 | 0.00439, 0.00945 | 0.00483 | 0.284, 0.132 | 11.4, 5.3 | 96.6 | 284, 132 | 0.811 |
| 3 | 0.394 | 0.00439, 0.0204 | 0.00483 | 0.284, 0.0613 | 11.4, 2.45 | 96.6 | 284, 61.3 | 0.866 |
| 4 | 0.414 | 0.00439, 0.0439 | 0.00483 | 0.284, 0.0284 | 11.4, 1.14 | 96.6 | 284, 28.4 | 0.888 |
| 5 | 0.428 | 0.00439, 0.0945 | 0.00483 | 0.284, 0.0132 | 11.4, 0.53 | 96.6 | 284, 13.2 | 0.675 |
| 6 | 0.437 | 0.00439, 0.204 | 0.00483 | 0.284, 0.00613 | 11.4, 0.245 | 96.6 | 284, 6.13 | 0.92 |
| 7 | 0.443 | 0.00439, 0.439 | 0.00483 | 0.284, 0.00284 | 11.4, 0.114 | 96.6 | 284, 2.84 | 0.89 |
| 8 | 0.498 | 0.0439, 0.00439 | 0.00483 | 0.0284, 0.284 | 1.14, 11.4 | 96.6 | 28.4, 284 | 1.18 |
| 9 | 0.512 | 0.0439, 0.00945 | 0.00483 | 0.0284, 0.132 | 1.14, 5.3 | 96.6 | 28.4, 132 | 1 |
| 10 | 0.544 | 0.0439, 0.0204 | 0.00483 | 0.0284, 0.0613 | 1.14, 2.45 | 96.6 | 28.4, 61.3 | 1.26 |
| 11 | 0.586 | 0.0439, 0.0439 | 0.00483 | 0.0284, 0.0284 | 1.14, 1.14 | 96.6 | 28.4, 28.4 | 1.26 |
| 12 | 0.622 | 0.0439, 0.0945 | 0.00483 | 0.0284, 0.0132 | 1.14, 0.53 | 96.6 | 28.4, 13.2 | 1.2 |
| 13 | 0.644 | 0.0439, 0.204 | 0.00483 | 0.0284, 0.00613 | 1.14, 0.245 | 96.6 | 28.4, 6.13 | 1.36 |
| 14 | 0.657 | 0.0439, 0.439 | 0.00483 | 0.0284, 0.00284 | 1.14, 0.114 | 96.6 | 28.4, 2.84 | 1.31 |
| 15 | 0.04 | 0.439, 0.00439 | 0.145 | 0.0853, 8.53 | 0.114, 11.4 | 2.32e+04 | 683, 6.83e+04 | 0.101 |
| 16 | 0.105 | 0.439, 0.00945 | 0.145 | 0.0853, 3.96 | 0.114, 5.3 | 2.32e+04 | 683, 3.17e+04 | 0.21 |
| 17 | 0.197 | 0.439, 0.0204 | 0.145 | 0.0853, 1.84 | 0.114, 2.45 | 2.32e+04 | 683, 1.47e+04 | 0.376 |
| 18 | 0.245 | 0.439, 0.0439 | 0.145 | 0.0853, 0.853 | 0.114, 1.14 | 2.32e+04 | 683, 6.83e+03 | 0.454 |
| 19 | 0.272 | 0.439, 0.0945 | 0.145 | 0.0853, 0.396 | 0.114, 0.53 | 2.32e+04 | 683, 3.17e+03 | 0.557 |
| 20 | 0.298 | 0.439, 0.204 | 0.145 | 0.0853, 0.184 | 0.114, 0.245 | 2.32e+04 | 683, 1.47e+03 | 0.605 |
| 21 | 0.318 | 0.439, 0.439 | 0.145 | 0.0853, 0.0853 | 0.114, 0.114 | 2.32e+04 | 683, 683 | 0.627 |

# Bibliography


[1] Z. Aksamija and I. Knezevic. Lattice thermal conductivity of graphene nanoribbons: Anisotropy and edge roughness scattering. *Appl. Phys. Lett.*, 98:141919, 2011.

[2] A. Akturk and N. Goldsman. Electron transport and full-band electron-phonon interactions in graphene. *J. Appl. Phys.*, 103:053702, 2008.

[3] F. J. Alexander, A. L. Garcia, and B. J. Alder. Cell size dependence of transport coefficients in stochastic particle algorithms. *Physics of Fluids*, 10:1540–1542, 1998.

[4] F. J. Alexander, A. L. Garcia, and B. J. Alder. Erratum: Cell size dependence of transport coefficients in stochastic particle algorithms [Phys. Fluids 10, 1540 (1998)]. *Physics of Fluids*, 12:731, 2000.

[5] K. Aoki, S. Takata, and F. Golse. A rarefied gas flow caused by a discontinuous wall temperature. *Physics of Fluids*, 13:2645–2661, 2001.

[6] M. Asen-Palmer, K. Bartkowski, E. Gmelin, and M. Cardona. Thermal conductivity of germanium crystal with different isotopic compositions. *Phys. Rev. B*, 56(15):9431–9447, 1997.

[7] L. L. Baker and N. G. Hadjiconstantinou. Variance reduction for Monte Carlo solutions of the Boltzmann equation. *Phys. Fluids*, 17:051703, 2005.

[8] L. L. Baker and N. G. Hadjiconstantinou. Variance-reduced Monte Carlo solutions of the Boltzmann equation for low-speed gas flows: A discontinuous Galerkin formulation. *Int. J. Numer. Meth. Fluids*, 58:381–402, 2008.

[9] A. A. Balandin. Thermal properties of graphene and nanostructured carbon materials. *Nat. Mater.*, 10:569–581, 2011.

[10] A. A. Balandin, S. Ghosh, W. Bao, I. Calizo, D. Teweldebrhan, F. Miao, and C. N. Lau. Superior thermal conductivity of single-layer graphene. *Nano Lett.*, 8(3):902–907, 2008.

[11] G. A. Bird. Approach to translational equilibrium in a rigid sphere gas. *Physics of Fluids*, 6:1518–1520, 1963.

[12] G. A. Bird. *Molecular Gas Dynamics and the Direct Simulation of Gas Flows.* Clarendon Press, 1994.

[13] N. Bonini, J. Garg, and N. Marzari. Acoustic phonon lifetimes and thermal transport in free-standing and strained graphene. *Nano Lett.*, 12:2673–2678, 2012.

[14] N. Bonini, M. Lazzeri, N. Marzari, and F. Mauri. Phonon anharmonicities in graphite and graphene. *Phys. Rev. Lett.*, 99:176802, 2007.

[15] D. A. Broido, A. Ward, and N. Mingo. Lattice thermal conductivity of silicon from empirical interatomic potentials. *Phys. Rev. B*, 72:014308, 2005.

[16] T. W. Brown and E. Hensel. Statistical phonon transport model for multiscale simulation of thermal transport in silicon: Part i – presentation of the model. *Int. J. Heat and Mass Transfer*, 55(25–26):7444 – 7452, 2012.

[17] T. W. Brown and E. Hensel. Statistical phonon transport model for multiscale simulation of thermal transport in silicon: Part {II} – model verification and validation. *Int. J. Heat and Mass Transfer*, 55(25–26):7453 – 7459, 2012.

[18] D. G. Cahill. Analysis of heat flow in layered structures for time-domain thermoreflectance. *Rev. Sci. Instrum.*, 75:5119, 2004.

[19] D. G. Cahill, W. K. Ford, K. E. Goodson, G. D. Mahan, A. Majumdar, H. J. Maris, R. Merlin, and S. R. Phillpot. Nanoscale thermal transport. *J. Applied Physics*, 93:793–818, 2003.

[20] D. G. Cahill, K. E. Goodson, and A. Majumdar. Thermometry and thermal transport in micro/nanoscale solid-state devices and structures. *J. Heat Transfer*, 124:223–240, 2002.

[21] W. Cai, A. L. Moore, Y. Zhu, X. Li, S. Chen, L. Shi, and R. S. Ruoff. Thermal transport in suspended and supported monolayer graphene grown by chemical vapor deposition. *Nano Lett.*, 10:1645–1651, 2010.

[22] J. Callaway. Model for lattice thermal conductivity at low temperatures. *Phys. Rev.*, 113(4):1046–1051, 1959.

[23] H. B. G. Casimir. Note on the conduction of heat in crystals. *Physica*, 5(6):495 – 500, 1938.

[24] C. Cercignani. *The Boltzmann Equation and its Applications.* Springer-Verlag, New York, NY, 1988.

[25] G. Chen. Nonlocal and nonequilibrium heat conduction in the vicinity of nanoparticles. *Journal of Heat Transfer*, 118(3):539–545, 1996.

[26] G. Chen. Size and interface effects on thermal conductivity of superlattices and periodic thin-film structures. *J. Heat Transfer*, 119:220–229, 1997.

[27] G. Chen. *Nanoscale Energy Transport and Conversion.* Oxford University Press, 2005.

[28] S. Chen, Q. Li, Y. Qu, H. Ji, R. S. Ruoff, and W. Cai. Thermal conductivity measurements of suspended graphene with and without wrinkles by micro-raman mapping. *Nanotech.*, 23:365701, 2012.

[29] S. Chen, A. L. Moore, W. Cai, J. W. Suk, J. An, C. Mishra, C. Amos, C. W. Magnuson, J. Kang, L. Shi, and R. S. Ruoff. Raman measurements of thermal transport in suspended monolayer graphene of variable sizes in vacuum and gaseous environments. *ACS Nano*, 5(1):321–328, 2011.

[30] Y. Chen, D. Li, J. R. Lukes, and Z. Ni. Monte Carlo simulation of silicon nanowire thermal conductivity. *J. Heat Transfer*, 127:1129–1137, 2005.

[31] R A Cowley. Anharmonic crystals. *Reports on Progress in Physics*, 31(1):123, 1968.

[32] R. B. Dingle. The electrical conductivity of thin wires. *Proceedings of the Royal Society of London. Series A. Mathematical and Physical Sciences*, 201(1067):545–560, 1950.

[33] K. Esfarjani, G. Chen, and H. T. Stokes. Heat transport in silicon from first-principles calculations. *Phys. Rev. B*, 84:085204, 2011.

[34] C. Faugeras, B. Faugeras, M. Orlita, M. Potemski, R. R. Nair, and A. K. Geim. Thermal conductivity of graphene in Corbino membrane geometry. *ACS Nano*, 4(4):1889–1892, 2010.

[35] R. P. Feynman. *Statistical Mechanics: A Set of Lectures.* Westview Press, 2nd edition, 1998.

[36] K. Fuchs. The conductivity of thin metallic films according to the electron theory of metals. *Mathematical Proceedings of the Cambridge Philosophical Society*, 34:100–108, 1938.

[37] Santhosh G. and Deepak Kumar. Anomalous transport and phonon renormalization in a chain with transverse and longitudinal vibrations. *Phys. Rev. E*, 82:011130, 2010.

[38] A. L. Garcia and W. Wagner. Timestep truncation error in direct simulation Monte Carlo. *Physics of Fluids*, 12:2621–2633, 2000.

[39] A. L. Garcia and W. Wagner. Direct simulation Monte Carlo method for the Uehling-Uhlenbeck-Boltzmann equation. *Physical Review E*, 68:056703, 2003.

[40] J. Garg. *Thermal Conductivity from First-Principles in Bulk, Disordered, and Nanostructured Materials.* PhD thesis, Massachusetts Institute of Technology, Cambridge, MA, 2011.

[41] S. Ghosh, I. Calizo, D. Teweldebrhan, E. P. Pokatilov, D. L. Nika, A. A. Balandin, W. Bao, F. Miao, and C. N. Lau. Extremely high thermal conductivity of graphene: Prospects for thermal management applications in nanoelectronic circuits. *Appl. Phys. Lett.*, 92(15):151911, 2008.

[42] G. Gilat and L. J. Raubenheimer. Accurate numerical method for calculating frequency-distribution functions in solids. *Phys. Rev.*, 144:390–395, 1966.

[43] N. G. Hadjiconstantinou. Analysis of discretization in the Direct Simulation Monte Carlo. *Phys. Fluids*, 12:2634–2638, 2000.

[44] N. G. Hadjiconstantinou. The limits of Navier-Stokes theory and kinetic extensions for describing small scale gaseous hydrodynamics. *Phys. Fluids*, 18:111301, 2006.

[45] N. G. Hadjiconstantinou, A. Garcia, M. Bazant, and G. He. Statistical error in particle simulations of hydrodynamic phenomena. *J. Comput. Phys.*, 187:274–297, 2003.

[46] N. G. Hadjiconstantinou, G. A. Radtke, and L. L. Baker. On variance-reduced simulations of the Boltzmann transport equation for small-scale heat transfer applications. *J. Heat Transfer*, 132:112401, 2010.

[47] J. M. Hammersley and D. C. Handscomb. *Monte Carlo Methods.* Wiley, New York, NY, 1964.

[48] H. Hamzeh and F. Aniel. Monte Carlo study of phonon dynamics in III-V compounds. *J. Appl. Phys.*, 109:063511, 2011.

[49] Q. Hao, G. Chen, and M. S. Jeng. Frequency-dependent Monte Carlo simulation of phonon transport in two-dimensional porous silicon with aligned pores. *J. Appl. Phys.*, 106:114321, 2009.

[50] M. G. Holland. Analysis of lattice thermal conductivity. *Physical Review*, 95(4), 1963.

[51] T. Homolle. Efficient particle methods for solving the Boltzmann equation. Master's thesis, Massachusetts Institute of Technology, 2007.

[52] T. M. M. Homolle and N. G. Hadjiconstantinou. A low-variance deviational simulation Monte Carlo for the Boltzmann equation. *J. Comput. Phys.*, 226(2341-2358), 2007.

[53] J. Hu, X. Ruan, and Y. P. Chen. Thermal conductivity and thermal rectification in graphene nanoribbons: A molecular dynamics study. *Nano Lett.*, 9(7):2730–2735, 2009.

[54] L. A. Jauregui, Y. Yue, A. N. Sidorov, J. Hu, Q. Yu, G. Lopez, R. Jalilian, D. K. Benjamin, D. A. Delk, W. Wu, Z. Liu, X. Wang, Z. Jiang, X. Ruan, J. Bao, S. Pei, and Y. P. Chen. Thermal transport in graphene nanostructures: Experiments and simulations. In *ECS Transactions*, volume 28, page 73, 2010.

[55] C. Jeong, S. Datta, and M. Lundstrom. Full dispersion versus Debye model evaluation of lattice thermal conductivity with a Landauer approach. *Journal of Applied Physics*, 109(7):073718, 2011.

[56] P. G. Klemens. Thermal conductivity and lattice vibrational modes. In *Solid State Physics*, volume 7. Academic, 1958.

[57] P. G. Klemens. Theory of the thermal conductivity of solids. In R. P. Tye, editor, *Thermal Conductivity*, volume 1. Academic, 1969.

[58] P. G. Klemens. Theory of thermal conduction in thin ceramic films. *Int. J. Thermophys.*, 22(1):265–275, 2001.

[59] P. G. Klemens and D. F. Pedraza. Thermal conductivity of graphite in the basal plane. *Carbon*, 22(4):735–741, 1994.

[60] T. Klitsner, J. E. VanCleve, H. E. Fisher, and R. O. Pohl. Phonon radiative heat transfer and surface scattering. *Physical Review B*, 38:7576–7594, 1988.

[61] Y. K. Koh and D. G. Cahill. Frequency dependence of the thermal conductivity of semiconductor alloys. *Phys. Rev. B*, 76:075207, 2007.

[62] O. V. Kovalev. *Representations of the Crystallographic Space Groups: Irreducible Representations, Induced Representations and Corepresentations.* Gordon and Breach, 1993.

[63] S. I. Kurganskii, O. I. Dubrovskii, and E. P. Domashevskaya. Integration over the two-dimensional Brillouin zone. *Phys. Stat. Sol. B*, 129:293–299, 1985.

[64] A. Rubio L. Wirtz. The phonon dispersion of graphite revisited. *Solid State Commun.*, 131:141–152, 2004.

[65] D. Lacroix, K. Joulain, and D. Lemonnier. Monte Carlo transient phonons transport in silicon and germanium at nanoscales. *Phys. Rev. B*, 72:064305, 2005.

[66] R. Landauer. Electrical transport in open and closed systems. *Zeitschrift für Physik B Condensed Matter*, 68:217–228, 1987.

[67] C. D. Landon and N. G. Hadjiconstantinou. Low-variance Monte Carlo simulation of thermal transport in graphene. *The International Mechanical Engineering Congress and Exposition*, paper number IMECE2012-87957, 2012.

[68] G. F. Lawler. *Introduction to Stochastic Processes.* Chapman & Hall, 1995.

[69] J.-U. Lee, D. Yoon, H. Kim, S. W. Lee, and H. Cheong. Thermal conductivity of suspended pristine graphene measured by Raman spectroscopy. *Phys. Rev. B*, 83:081419, 2011.

[70] L. Lindsay and D. A. Broido. Optimized Tersoff and Brenner empirical potential parameters for lattice dynamics and phonon thermal transport in carbon nanotubes and graphene. *Phys. Rev. B*, 81:205441, 2010.

[71] L. Lindsay, D. A. Broido, and N. Mingo. Flexural phonons and thermal transport in graphene. *Phys. Rev. B*, 82:115427, 2010.

[72] A. A. Maradudin and A. E. Fein. Scattering of neutrons by an anharmonic crystal. *Phys. Rev.*, 128:2589–2608, 1962.

[73] Y. Masao, M. Okano, and M. Matsumoto. DSMC scheme to study phonon dynamics. *J. Mechanical Science and Technology*, 25:21–26, 2011.

[74] M. Matsumoto, M. Okano, and Y. Masao. DSMC scheme for phonon transport in solid thin films. *J. Heat Transfer*, 134:051009, 2012.

[75] S. Mazumder and A. Majumdar. Monte Carlo study of phonon transport in solid thin films including dispersion and polarization. *J. Heat Transfer*, 123:749–759, 2001.

[76] A. J. H. McGaughey, E. S. Landry, D. P. Sellan, and C. H. Amon. Size dependent model for thin film and nanowire thermal conductivity. *Appl. Phys. Lett.*, 99:131904, 2011.

[77] N. Mingo, D.A. Stewart, D.A. Broido, L. Lindsay, and W. Li. Ab initio thermal transport. In Subhash L. Shindé and Gyaneshwar P. Srivastava, editors, *Length-Scale Dependent Phonon Interactions*, volume 128 of *Topics in Applied Physics*, pages 137–173. Springer New York, 2014.

[78] A. J. Minnich. Determining phonon mean free paths from observation of quasiballistic thermal transport. *Physical Review Letters*, 109:205901, 2012.

[79] A. J. Minnich, J. A. Johnson, A. J. Schmidt, K. Esfarjani, M. S. Dresselhaus, K. A. Nelson, and G. Chen. Thermal conductivity spectroscopy technique to measure phonon mean free paths. *Phys. Rev. Lett.*, 107:095901, 2011.

[80] C. Moler and C. Van Loan. Nineteen dubious ways to compute the exponential of a matrix, twenty-five years later. *SIAM Review*, 45(1):3–46, 2003.

[81] N. Mounet and N. Marzari. First-principles determination of the structural, vibrational and thermodynamic properties of diamond, graphite, and derivatives. *Phys. Rev. B*, 71(20):205214, 2005.

[82] S. V. J. Narumanchi, J. Y. Murthy, and C. H. Amon. Submicron heat transport model in silicon accounting for phonon dispersion and polarization. *J. Heat Transfer*, 126:946–955, 2004.

[83] D. L. Nika, S. Ghosh, E. P. Pokatilov, and A. A. Balandin. Lattice thermal conductivity of graphene flakes: Comparison with bulk graphite. *Appl. Phys. Lett.*, 94:203103, 2009.

[84] D. L. Nika, E. P. Pokatilov, A. S. Askerov, and A. A. Balandin. Phonon thermal conduction in graphene: Role of umklapp and edge roughness scattering. *Phys. Rev. B*, 79:155413, 2009.

[85] D. L. Nika, E. P. Pokatilov, and A. A. Balandin. Theoretical description of thermal transport in graphene: The issues of phonon cut-off frequencies and polarization branches. *Phys. Stat. Sol. B*, 248(11):2609–2614, 2011.

[86] K. S. Novoselov, A. K. Geim, S. V. Morozov, D. Jiang, Y. Zhang, S. V. Dubonos, I. V. Grigorieva, and A. A. Firsov. Electric field effect in atomically thin carbon films. *Science*, 306(5696):666–669, 2004.

[87] M. Omini and A. Sparavigna. An iterative approach to the phonon Boltzmann equation in the theory of thermal conductivity. *Phyisca B*, 212:101–112, 1995.

[88] J. A. Pascual-Gutiérrez, J. Y. Murthy, and R. Viskanta. Thermal conductivity and phonon transport properties of silicon using perturbation theory and the environment-dependent interatomic potential. *J. Appl. Phys.*, 106(6):063532, 2009.

[89] R. Peierls. On the kinetic theory of thermal conduction in crystals. *Ann. Phys.*, 3:1055–1101, 1929.

[90] J-P. M. Péraud. Low variance methods for Monte Carlo simulation of phonon transport. Master's thesis, Massachusetts Institute of Technology, Cambridge, MA, 2011.

[91] J-P. M. Péraud and N. G. Hadjiconstantinou. Efficient simulation of multidimensional phonon transport using energy-based variance-reduced Monte Carlo formulations. *Phys. Rev. B*, 84:205331, 2011.

[92] J-P. M. Péraud and N. G. Hadjiconstantinou. An alternative approach to efficient simulation of micro/nanoscale phonon transport. *Appl. Phys. Lett.*, 101:153114, 2012.

[93] J-P. M. Péraud, C. D. Landon, and N. G. Hadjiconstantinou. Monte Carlo methods for solving the Boltzmann transport equation. *Annu. Rev. Heat Trans.*, 17, 2014.

[94] J. P. Perdew and A. Zunger. Self-interaction correction to density-functional approximations for many-electron systems. *Phys. Rev. B*, 23:5048–5079, 1981.

[95] John P. Perdew, Kieron Burke, and Matthias Ernzerhof. Generalized gradient approximation made simple. *Phys. Rev. Lett.*, 77:3865–3868, 1996.

[96] R. B. Peterson. Direct simulation of phonon-mediated heat transfer in a Debye crystal. *J. Heat Transfer*, 116:816–822, 1994.

[97] E. S. Piekos, S. Graham, and C. C. Wong. Multiscale thermal transport. Technical Report SAND2004-0531, Sandia National Laboratories, 2004.

[98] E. Pop, V. Varshney, and A. K. Roy. Thermal properties of graphene: Fundamentals and applications. *MRS Bulletin*, 37:1273–1281, 2012.

[99] R. Prasher. Transverse thermal conductivity of porous materials made from aligned nano- and microcylindrical pores. *J. Appl. Phys.*, 100(6):064302, 2006.

[100] R. Prasher. Thermal boundary resistance and thermal conductivity of multiwalled carbon nanotubes. *Phys. Rev. B*, 77:075424, 2008.

[101] D. J. Rader, M. A. Gallis, J. R. Torczynski, and W. Wagner. Direct simulation Monte Carlo convergence behavior of the hard-sphere gas thermal conductivity for Fourier heat flow. *Phys. Fluids*, 18:077102, 2006.

[102] G. A. Radtke. *Efficient Simulation of Molecular Gas Transport for Micro- and Nanoscale Applications.* PhD thesis, Massachusetts Institute of Technology, Cambridge, MA, 2011.

[103] G. A. Radtke, N. G. Hadjiconstantinou, and W. Wagner. Low-noise Monte Carlo simulation of the variable hard-sphere gas. *Phys. Fluids*, 23:030606, 2011.

[104] S. Rjasanow and W. Wagner. *Stochastic Numerics for the Boltzmann Equation.* Springer-Verlag, Berlin, 2005.

[105] N. A. Roberts and D. G. Walker. Computational study of thermal rectification from nanostructured interfaces. *J. Heat Transfer*, 133:092401, 2011.

[106] P. K. Schelling and S. R. Phillpot. Multiscale simulation of phonon transport in superlattices. *J. Applied Physics*, 93(9):5377–5387, 2003.

[107] A. Schmidt. Pump probe thermoreflectance. In *Annual Review of Heat Transfer*, volume 16. Begell House, in press.

[108] A. J. Schmidt, X. Chen, and G. Chen. Pulse accumulation, radial heat conduction, and anisotropic thermal conductivity in pump-probe transient thermoreflectance. *Rev. Sci. Instrum.*, 79:114902, 2008.

[109] J. H. Seol, I. Jo, A. L. Moore, L. Lindsay, Z. H. Aitken, M. T. Pettes, X. Li, Z. Yao, R. Huang, D. Broido, N. Mingo, R. S. Ruoff, and L. Shi. Two-dimensional phonon transport in supported graphene. *Science*, 328:213–216, 2010.

[110] H. Sevinçli and G. Cuniberti. Enhanced thermoelectric figure of merit in edge-disordered zigzag graphene nanoribbons. *Phys. Rev. B*, 81:113401, 2010.

[111] M. E. Siemens, Q. Li, R. Yang, K. A. Nelson, Erik H. Anderson, M. M. Murnane, and H. C. Kapteyn. Quasi-ballistic thermal transport from nanoscale interfaces observed using ultrafast coherent soft x-ray beams. *Nat Mater*, 9(1):26–30, 2010.

[112] D. Singh, J. Y. Murthy, and T. S. Fisher. On the accuracy of classical and long wavelength approximation for phonon transport in graphene. *J. Appl. Phys.*, 110:113510, 2011.

[113] D. Singh, J. Y. Murthy, and T. S. Fisher. Spectral phonon conduction and dominant scattering pathways in graphene. *J. Appl. Phys.*, 110:094312, 2011.

[114] Y. Sone. *Kinetic Theory and Fluid Dynamics.* Birkhäuser Boston, 2002.

[115] G. P. Srivastava. *The Physics of Phonons.* CRC Press, 1990.

[116] G. Strang. On the construction and comparison of difference schemes. *SIAM J. Numerical Analysis*, 5(3):506–517, 1968.

[117] A. K. Vallabhaneni, J. Hu, Y. P. Chen, and X. Ruan. Thermal rectification in graphene and carbon nanotube systems using molecular dynamics simulations. In *Proceedings of the ASME/JSME 2011 8th Thermal Engineering Joint Conference*, 2011.

[118] R. S. Varga. *Matrix Iterative Analysis.* Springer Series in Computational Mathematics. Prentice Hall, Inc, 2nd edition, 1962.

[119] W. G. Vincenti and C. H. Kruger. *Introduction to Physical Gas Dynamics.* Wiley, New York, 1965.

[120] W. Wagner. Deviational particle Monte Carlo for the Boltzmann equation. *Monte Carlo Methods Appl.*, 14:191–268, 2008.

[121] Z. Wang, J. E. Alaniz, W. Jang, J. E. Garay, and C. Dames. Thermal conductivity of nanocrystalline silicon: Importance of grain size and frequency-dependent mean free paths. *Nano Letters*, 11(6):2206–2213, 2011.

[122] X. Wen. High order numerical methods to three dimensional Delta function integrals in level set methods. *SIAM J. Sci. Comput.*, 32(3):1288–1309, 2010.

[123] Fan Yang and Chris Dames. Mean free path spectra as a tool to understand thermal conductivity in bulk and nanostructures. *Phys. Rev. B*, 87:035437, 2013.

[124] J. M. Ziman. *Electrons and Phonons.* Oxford Clarendon Press, 1960.